In response to the 2016 ESA's call for M5 Mission Proposals

European SpaceCraft for the study of Atmospheric Particle Escape (ESCAPE)

Iannis Dandouras (Lead), Masatoshi Yamauchi, and the ESCAPE proposal team

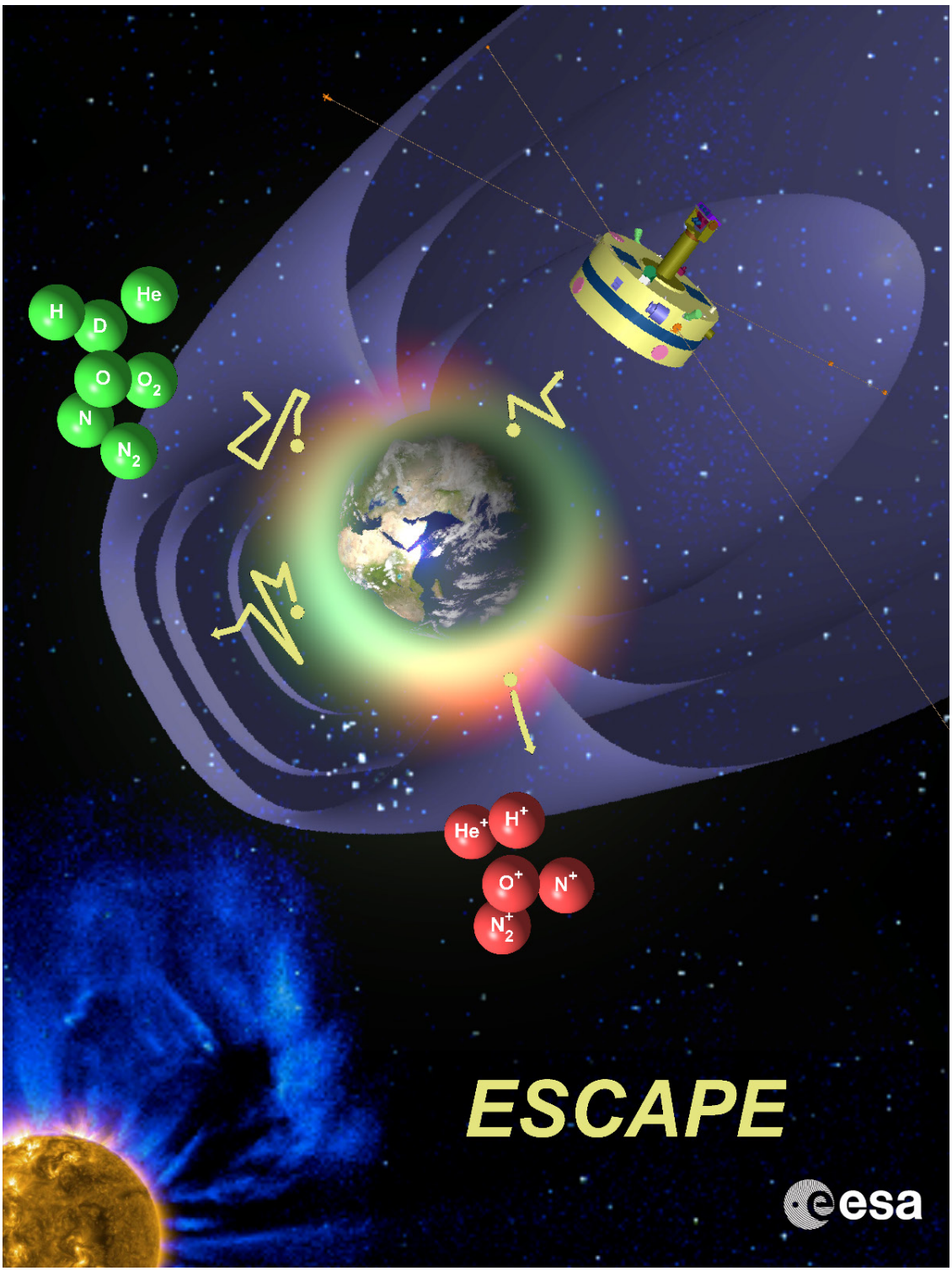

Proposing Team of the ESCAPE Mission

Lead Proposer (single-point contact):

I. Dandouras <Iannis.Dandouras@irap.omp.eu>
CNRS and Paul Sabatier Toulouse University, Institut de Recherche en Astrophysique et Planétologie (IRAP), 9 avenue du Colonel Roche, BP 44346, F-31028 Toulouse, Cedex 4, France
Phone: +33-561558320 / *fax:* +33-561556701

The Lead Proposer can and will support the study activities at the level of at least 20% of his time throughout the study period.

Core team members:

M. Yamauchi <M.Yamauchi@irf.se>
Swedish Institute of Space Physics (IRF), Box 812, S-98128 Kiruna, Sweden

H. Rème <Henri.Reme@irap.omp.eu> (IRAP)

O. Marghitu <marghitu@gpsm.spacescience.ro>
Institute for Space Sciences (ISS), 409 Atomistilor Street, RO-77125, Bucharest-Magurele, Romania

J. De Keyser <johandk@aeronomie.be >
Royal Belgian Institute for Space Aeronomy (BIRA-IASB), Ringlaan 3, B-1180 Brussels, Belgium

PI, PI institute, & main national funding agency for scientific payload (blue=ESA states)

Instument	PI/co-PI	PI institute	Funding
INMS	P. Wurz	University of Bern, Physikalisches Institut, Bern, Switzerland (*U.Bern*)	**SSO**
WCIMS	N. Paschalidis	NASA Goddard Space Flight Center, Greenbelt, USA (*GSFC*)	**NASA**
MIMS	I. Dandouras	*IRAP* (see above)	**CNES**
NOIA	M. Wieser	*IRF* (see above)	**SNSB**
EMS	L. Kistler	University of New Hampshire, Durham, USA (*UNH*)	**NASA**
ESMIE	A. Fazakerley	Mullard Space Science Laboratory, UCL, Holmbury St. Mary, Surrey, UK (*MSSL*)	**UKSA**
SLP	J. De Keyser	*BIRA-IASB* (see above)	**BELSPO**
MAG	R. Nakamura	Institut für Weltraumforschung, Graz, Austria (*IWF*)	**ALR/FFG**
WAVES	B. Grison	Institute of Atmospheric Physics, Academy of Sciences, Prague, Czech Republic (*ASCR/IAP*)	**PRODEX**
Search Coil	J.-L. Pincon (co-PI)	Laboratoire de Physique et Chimie de l'Environnement et de l'Espace, Orléans, France (*LPC2E*)	**CNES**
UVIS	I. Yoshikawa	University of Tokyo, Kashiwa, Japan (*U.Tokyo*)	**JAXA**
ENAI	A. Milillo	INAF/Istituto di Astrofisica e Planetologia Spaziali, Rome, Italy (*IAPS*)	**ASI**
AMC	T. Sakanoi	Tohoku University, Sendai, Japan *(TohokuU)*	**JAXA**
DPU	A. Paschalis I. Daglis (co-PI)	National and Kapodistrian University of Athens, Greece (*NKUA*)	**GSRT**
EISCAT_3D	I. Häggström	EISCAT Headquarters, Kiruna, Sweden	**EISCAT**
Model and inter-disciplinary analyses	F. Tian (*Tsinghua U., Beijing*), M. Liemohn and R. Ilie (*U. Michigan*), O. Marghitu (*ISS, Bucharest*), J.-Y. Chaufray (*LATMOS, Paris*), J. Saur (*U. Köln*), J. Zönnchen (*U. Bonn*), H. Lammer (*IWF*), Y. Ebihara (*Kyoto U.*), A. Beth (*Imperial College, London*), J. Machol (*NOAA, Boulder*), L. Waldrop (*U. Illinois*), E. Mierkiewicz (*Embry-Riddle Aero. U.*), V. Airapetian (*NASA/GSFC*)		

Acknowledgments

The ESCAPE team acknowledges the support from CNES PASO, in the preparation of the proposal.

Executive Summary

ESCAPE Summary Table	
Element	**Explanation**
Question	**How and at what rate is Earth slowly losing its atmosphere to space?**
Specific Goal #1	**Build a quantitative and comprehensive picture for 500-2000 km altitudes** - Determine exospheric altitude density profiles and temperature profile as a function of different drivers such as solar EUV, solar wind and geomagnetic conditions. - Establish isotope ratios for both neutrals and ions and compare them with those found at the Earth's surface and in other solar system objects. - Determine exospheric altitude profiles of ion/neutral ratios and estimate ionisation/neutralisation efficiencies. - Measure temporal and spatial variations of the density of major exospheric species. - Correlate such variability with upper atmosphere parameters, and with different incident energies when particle precipitation is present.
Specific Goal #2	**Determine the dominant escape mechanisms, and their dependence on the drivers** - Estimate thermal escape flux for neutral and ion species for different conditions. - Estimate the prevailing escape mechanisms and the relative importance of thermal or non-thermal escape for different driver conditions. - Estimate the response of the ionisation/neutralisation efficiencies, isotope fractionation and the N/O ratio to different drivers. - Estimate the degree of recirculation of plasma after it has left the ionosphere.
Spacecraft	- Single slowly spinning spacecraft (~3 rpm) with a despun platform. - Chemical cleanliness, including cold gas (Kr or Xe) propulsion for attitude control. - Moderate (Cluster level) magnetic cleanliness and EMC requirements
Payload	**Payload for in-situ measurements** - INMS: Cold ion and neutral mass spectrometer ($M/\Delta M$ ~1100, 10^{-3}–10^{3}/cc per 5 sec) - WCIMS: High time resolution cold ion analyser ($M/\Delta M > 50$, per 5 sec) - MIMS: Light hot ions ($M < 20$, N/O separation, 5 eV/q – 40 keV/q) - NOIA: Heavy hot ions ($M > 10$, N_2/O separation, 10 eV/q – 30 keV/q) - EMS: Energetic ions (H^+, He^+, O^{++}, N^+, O^+, N_2^+, 20–200 keV) - ESMIE: Ionospheric photoelectrons & magnetospheric electrons (5 eV – 20 keV) - SLP: Plasma density, E-field, spacecraft potential (Langmuir probe) - MAG: Magnetic field (5nT accuracy) - WAVES: Electromagnetic waves (5 Hz – 20 kHz) **Payload for remote measurements and for line-of-sight information** - UVIS: UV imaging spectrometer (85–140 nm, optional: O^+ 83 nm, He 58 nm, He^+ 30 nm) - ENAI: Energetic neutral atoms imager (2 – 200 keV) - AMC: Aurora monitoring and airglow camera (O: 630 nm, N_2: 670nm) **Mandatory subsystems (by ESA)** - Two DPUs (hardware), two 5 m rigid booms for MAG and search coil, 15-20 m wire booms for SLP, Active spacecraft potential control (ASPOC)
Orbit	- elliptic Earth orbit (~500 km x 33000 km altitude with ~10 hr orbital period) - high-inclination (~90°) to cover polar cap and EISCAT_3D observation area - no need of orbit manoeuvres to change apogee
Resolution	* temporal < 1 minute & vertical < 150 km at 500–2000 km altitude
Duration	* 3 year nominal mission with instruments designed to operate for 5 years
Radiation	* Shielding of ~5 mm aluminium equivalent will keep dose < 50 krad for 3 years
Downlink	- 19 Gbit/day with 30 W RF transmitter to ESA stations; >10 GByte onboard memory
Science Operations	- ESA (ESOC/ESAC) is responsible for operation, data collection/archiving/distribution. - Real-time detection of the radiation belts to change to a reduced operational mode.
Data policy	- Level 2 (calibrated) data delivery within 6 months. - Key parameters or equivalent data (open access) within 12 months.
Collaboration	* USA (NASA) and Japan (JAXA): instrument provision (EMS, WCIMS, UVIS, AMC) * EISCAT: conjugate ground-based 3-D observations (ions and electrons at > 500 km)
Cost	338 M€ (SC: 125 M€; ESA payload elements :15 M€; SC chemical cleanliness pro.: 10 M€; Operations: 50 M€; A62 Launch: 73 M€; ESA internal cost: 30 M€, contingency: 35 M€)

Scientific goal:

The purpose of the ESCAPE mission is to **obtain the composition and flux of the atmospheric escape from the Earth and understand its effect on the evolution of atmosphere** (Cosmic Vision Theme 1). Although this subject, including escape from planetary atmospheres, has been studied for many years, the existing data are incomplete for estimating even the basic values of the escape rate for different driver conditions. To answer these questions, the ESCAPE mission will measure both neutrals and superthermal ions of major atmospheric species H, He, O, N, O_2, N_2, NO, and CO_2 in the exosphere/ upper ionosphere in the altitude range 500–2000 km, as well as major hot ions (H^+, He^+, O^+, N^+, N_2^+) in upper ionosphere, plasmasphere, polar cap, and inner magnetosphere. As a unique measurement, the variability of the isotope ratio in both space and time will be examined for the first time in the geospace environment.

These measurements will lead to **(1) the first quantitative and comprehensive observations of the entire exosphere** and upper ionosphere (500-2000 km altitude) that will allow quantitative modelling of the thermal escape, and **(2)** determination of the dominant non-thermal escape mechanisms that will allow evaluation of **relative importance of thermal and non-thermal escape**, both critical in modelling the composition of the atmospheric escape under different internal and external drivers (solar UV, solar wind, magnetospheric and ionospheric conditions).

The proposed measurements will also **(a)** contribute to fundamental physics and chemistry questions on **how the isotopes fractionate** and **what the operating ionisation/neutralising efficiencies are in the space environment** (Cosmic Vision Theme 3), and **(b)** serve as an important reference for **understanding the evolution of the atmospheres** of other planets (comparative planetology) because the majority of the basic escape mechanisms working on planets or on the past Earth are expected to be currently operating at the Earth.

ESCAPE's measurements will have implications for other science fields including: **(c)** estimating the history of the N/O ratio of the Earth that influences biological activity (astrobiology), **(d)** dynamic modelling of the exosphere for a better understanding of exospheric light contaminations pertinent to astrophysical spectroscopy observations, **(e)** dynamics at the topside ionosphere, **(f)** exospheric effects on the ionosphere-plasmasphere coupling through chemistry, transport, and electric field, and **(g)** magnetospheric-ionosphere coupling with the orbit covering various routes of ion transport between the two regions.

Measurements required to achieve the science goals:

All measurements will be made with flight-proven or equivalent instruments on board a single slowly spinning (3 rpm) spacecraft equipped with a despun platform for the remote sensing optical measurements. To maximise the utility of the despun platform the spin axis will point to the Sun with a pointing accuracy of < 1°. The orbit has high-inclination (> 80°) with perigee and apogee at ~500 km x 33000 km altitudes (~10 hr orbital period) to cover the polar cap, inner magnetosphere, exosphere, and topside ionosphere at all local times. Latitudinal drift of the apogee allows coverage of all altitudes in the polar cap. A high-inclination orbit will optimise geomagnetic conjugate observations with the EISCAT_3D ground-based radar facility, which will yield for the first-time continuous 3D volume measurement of the ionosphere over 10°–20° latitudinal range in the northern Europe.

The spacecraft includes a full suite of particle instruments: hot and energetic ion instruments with N/O separation capability, cold ion and neutral instruments with isotope separation capability ($M/\Delta M \approx 1100$) down to as low as 10^{-4} cm^{-3} for ions and $>10^{-1}$ cm^{-3} for neutrals, and a hot electron instrument with capability of identifying photoelectron peaks. The spacecraft potential is controlled to < +5 eV level to allow the measurements of cold ions and photoelectrons. The spacecraft potential will be monitored with a Langmuir probe on two 15-20 m wire booms, and pitch-angles of ions and electrons will be measured using a magnetometer on a 5 m rigid boom. Two spacecraft DPUs are used for handling the data, one on the spinning platform and the other on the despun platform.

The spacecraft includes an imaging UV spectrometer on the despun platform to obtain line-of-sight integrated images of various emission lines, including the nitrogen ions and neutrals (*85–140 nm* for H, N, O; and at *83 nm* for O^+, *58 nm* for He, and *30 nm* for He^+). The altitude resolution will be < 100 km for a 500–3000 km altitude range.

The remaining instruments will monitor the background conditions: aurora monitor to determine the energy injection to the ionosphere on a global scale, simple wave measurements with a search coil magnetometer on a separate 5 m rigid boom, and an energetic neutral atom (ENA) imager for monitoring the geomagnetic storm/substorm activity.

The total mass and power of the scientific payload, including shielding, is less than 150 kg and 150 W. The total mission budget including 3 year operations is about 330–340 M€ for ESA.

1. Scientific Objectives (Key Science)

1.1. Background: Why do we study the atmospheric escape from the Earth?

Understanding the evolution of the planetary atmospheres, particularly of the composition of Earth's atmosphere, is a major challenge in both geoscience and planetary science. Why are the atmospheres and surface compositions of the Earth so different compared to Mars and Venus, although the initial composition of these "brother" planets 4.5 billion years ago is believed to have been similar to each other, as indicated, e.g., by the $^{15}N/^{14}N$ ratio (Füri and Marty, 2015)? Why and how much is the Earth special in terms of habitability? How much has the atmospheric evolution of the Earth been influenced by the planetary magnetic field and the biologic/subsurface activities? How was the atmospheric evolution in the ancient time right after life emerged? These fundamental questions are largely not well understood.

Studying the atmospheric evolution of the Earth is particularly important compared to the similar studies of the other planets. First, it is directly related to the past and future of the habitable environment of the Earth. Second, we can obtain the best knowledge among measurable planets thanks to many other measurements at and from the ground. Nevertheless, our knowledge on the atmospheric evolution of the Earth is still patchy and very limited for any quantitative modelling of the past conditions.

Evolution of a habitable atmosphere

The Earth is a unique habitable body with actual life, and that is strongly related to its atmosphere. The present atmospheric composition is quite different from that of the other planets after 4.5 billion years of evolution, and quite different from the ancient Earth billions of years ago (e.g., compared to the time when life emerged or even right after the photosynthesis started). The present atmospheric composition may even be significantly different from the atmosphere when historical distinctions of life occurred. The unique evolution of the atmosphere allowed life to emerge and survive in the ancient Earth and to evolve to the present time.

Constructing reliable models of the ancient atmosphere and its evolution is one of the key issues in studies of the origin and evolution of life on the Earth. Past efforts have focused on modelling an initial neutral atmosphere from planetary formation models (e.g., Owen, 1998; Kasting and Brown, 1998; Abe et al., 2000; Commeyras et al., 2006; Hashimoto et al., 2007). However, the initial atmosphere was not as stable as it is now, and could have quickly evolved even after the major outgassing and bombardment period was over because of enhanced escape to space (due to high solar UV flux) and migration to the subsurface (Kasting and Brown, 1998; Kasting and Catling, 2003; Lammer et al., 2003, 2008; Hashimoto et al., 2007, Airapetian et al. 2014, 2016; Johnson and Goldblatt, 2015). The atmospheric conditions at the time when life emerged were already quite different from what the solar system formation models can predict. Fortunately, the evolution part (escape and migration) of the atmosphere can be modelled using the present-day observations because many of the processes are still occurring.

During the subsequent evolution of life, the atmospheric composition (and the water solutions affected by the atmosphere) must have played an important role (Sagan and Chyba, 1997; Freda and McDonald, 1988; Gunn and Keller 1990; Shaviv, 2003; Lammer et al., 2009). Unlike the non-organic planetary surfaces of Mars and Venus, the biologic activity on the Earth's surface is very sensitive to the atmospheric composition. Only a few percent change in the atmospheric O_2/N_2 ratio or in the water pH, or a few degrees change in the atmospheric/water temperature may significantly affect the biochemical reactions and hence metabolism and photosynthesis (e.g., Loesche, 1969; Hill, 1976; Servaites, 1977; Ku et al., 1977; Harrison, 2010). A few percent-level change of the atmospheric N/O ratio corresponds to about a 10% change in the nitrogen inventory in the biosphere. As described below, such a change is realistic on the geological time scale.

Escape to space

There are five main channels that determine the evolution of the atmosphere: **(a)** net escape to space after removing the return flow, **(b)** net influx from space (e.g., meteors), **(c)** biospheric reactions (e.g., O_2 after photosynthesis), **(d)** sub-surface sink through ocean bottom, and **(e)** emission from sub-surface through both non-organic (e.g., volcanic) and organic activities (bacterial denitrification) (Berner, 1999; Canfield, 2005; Bababash et al., 2007; Johnson and Goldblatt, 2015). Among those, (d) and (e) are related to the inventory in the Earth's interior.

The inventory of the major elements in the atmosphere, i.e., N, O, H, and C, is larger in the Earth's interior. Even for nitrogen, of which the atmosphere comprises more than 80% of the inventory of the entire biosphere (atmosphere, ocean, and soil), 3-10 times more is stored in the solid part of the Earth (Johnson and Goldblatt, 2015). This means that already a 1-3% change in the nitrogen

inventory of the Earth's interior can substantially affect the atmospheric N/O ratio.

However, the actual contribution of the Earth's interior to the evolution of the atmosphere is not necessarily significant except for ancient times, because it mainly contributes to recycling of elements rather than causing net changes through (e). On the other hand, the escape to space causes net changes, and therefore, its relative importance, compared to the sub-surface migration, increases with the planetary age. The question is: how much? If the average nitrogen loss rate reaches $10^{27}s^{-1}$, 2×10^{43} atoms (that comprise 10% of the atmospheric 4-5×10^{18} kg nitrogen) will be lost in 600 million years ($=2\times10^{16}$ sec).

Such an escape rate to space is not unrealistic for the ancient Earth, according to the result from the Sun-in-Time project (Ribas et al., 2005; Wood et al., 2005), in which G-type stars at different stages are compared in order to model the past Sun. The comparison suggests that the past Sun emitted much higher EUV radiation (EUV is defined as 10-120 nm range that activates photochemistry including generation of N_2^+, $N^+$and O^+), and had a faster rotation (driving more active solar dynamo, which resulted in more active sunspot and a stronger interplanetary magnetic field) and a faster solar wind (Ayres, 1997; Wood, 2006; Kulikov et al., 2006; Airapetian and Usmanov, 2016). In fact, the combination of the high geomagnetic activity during major storms and the high solar EUV flux has been used as proxy of normal (or solar minimum) conditions during the ancient time, billion of years ago (Krauss et al., 2012; Airapetian et al., 2014).

Under high solar and geomagnetic activity conditions that can be presumably used as a proxy of the ancient normal conditions, the instantaneous non-thermal ion escape rate from the geomagnetically open part of the polar cap observed by the Cluster hot plasma instrument (> 30 eV threshold) increased by two orders of magnitude as shown in **Fig. 1.1**, reaching to $10^{27}s^{-1}$ instantaneous value from nominal values of about $10^{25}s^{-1}$ (Moore et al., 1999; Peterson et al., 2008; Nilsson, 2011, Slapak et al, 2012, 2015). In addition, limited observations from Akebono (cold ions <50 eV) and AMPTE (energetic ions > 30 keV) satellites in the magnetosphere showed an increase of the N/O ratio by at least one order of magnitude to reach a 1:1 ratio during high geomagnetic activity conditions (Hamilton et al., 1988; Yau and Whalen, 1992; Yau et al., 1993). Therefore, nitrogen escape to space during the ancient time could have substantially affected the atmospheric N/O ratio on the time scale of life evolution.

Thus, understanding the escape is important independently of the sub-surface route, although a complete modelling of the atmospheric evolution (particularly for O and H) requires knowledge of the space route as well as the sub-surface route. Furthermore, the method to tackle the sub-surface route is completely different from that of the space route.

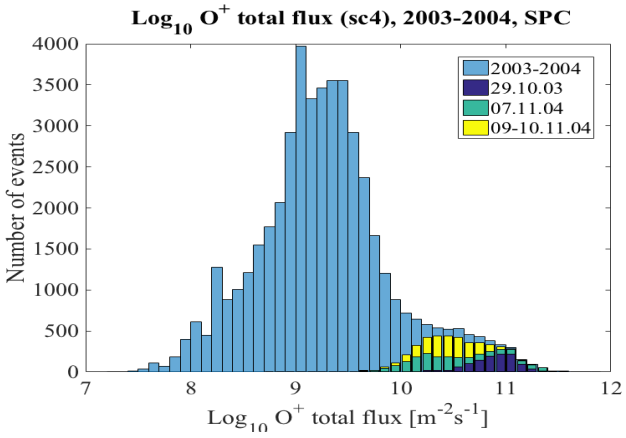

Fig. 1.1: Distribution of local spin-averaged flux values of heavy ions (CNO group) at Cluster location. It reaches 3×10^{17} $km^{-2}s^{-1}$ ($\sim10^{25}$ $R_E^{-2}s^{-1}$) at around 6-8 R_E, With a 6 R_E radius of enlarged open area at Cluster altitude, this gives instantaneous heavy ion escape rate up to $\sim10^{27}$ s^{-1} during big events.

Among the sources (from subsurface and space) and losses (to subsurface and space), **this mission addresses the question of atmosphere escape to space: how and at what rate is the Earth losing the atmosphere,** particularly the major species H, He, O, N, O_2, N_2, NO, and CO_2, as both neutrals and ions.

Reference for the other planets

Without a biologic route or an ocean route to migrate the atmospheric elements (the ocean route enhances sub-surface circulation), roles of the atmospheric escape to the evolution of their atmospheres is relatively important for Mars and Venus compared to the Earth. Fortunately, the majority of mechanisms related to the space route are common between the Earth and the other planets, and therefore, knowledge from the Earth is useful. **Table 1.1** summarises the major escape mechanisms to space known to date, and the third column shows the regions (black) and planets (blue) where the listed mechanism mainly operates (Lundin et al.; 1990, 2004, 2013, Lundin and Barabash, 2004), Brace and Kliore 1991; Luhmann and Bauer, 1992; Luhmann et al., 1992; Jakosky et al., 1994; Lammer et al., 2003, 2008, 2013; Brecht and Ledvina, 2006; Kulikov et al., 2006; Chaufray et al., 2007; Schaufelberger et al., 2012 for unmagnetised planets, and Sagan and Mullen, 1972; Walker, 1977; Kasting and Brown,

1998; Moore et al.,, 1999; Sibeck et al., 1999; Brandt et al., 1999; Kasting and Catling, 2003; Fujimoto et al.,, 2006; Kulikov et al., 2007; Darrouzet et al., 2009; Nilsson, 2011; and Fok et al., 2014) for magnetised planets). Except for (d), all mechanisms are operating at present on Earth, while (d) can be estimated if (a) and (b) are well understood because they all require good knowledge on the exosphere (details are discussed later). Understanding the atmospheric evolution of the present Earth is, therefore, inevitable to understand the evolution of other atmospheres like Earth-like planets or the ancient Earth.

Advantage of observing the Earth

Among all planets, the Earth is by far the easiest target to obtain the escaping fluxes for each mechanism listed in **Table 1.1**, because of extra resources (payload mass and power of the spacecraft), extra facilities (e.g., ground-based facilities), past knowledge (e.g., surface interaction), and long database (solar wind and magnetospheric conditions). Among those, the existence of ground-based facilities is a strong advantage. For example, Cluster and Themis benefitted from the synergy of ground observations (e.g., Aikio et al., 2004; Mende et al., 2009). The latest relevant ESA mission is

Table 1.1. Major escape mechanisms into space of planetary atmospheres heavy elements, and mass filtering effect of each in terms of energy (velocity). cf. §1.4 and 1.5.

Type of the mechanism	**Description of the mechanism**	**reference altitude** *1 **planets**	**mass-filter** *2
(a) Jeans escape (neutrals)	Thermal tail exceeds the escape velocity.	exobase Mars>Earth≥Venus*3	exp() *4
(b) Photochemical heating (mainly neutrals)	Release of energy in the excited state, e.g., through recombination, gives escape velocity to the atom.	exosphere Mars>Venus~Earth	$m^{-0.5}$
(c) Hydrodynamic blow off (neutrals & ions)	Massive escape when thermal energy exceeds escape energy, and these escaping light molecules collide with heavier molecules.	upper thermosphere ancient (all planets)	$m^{-0.5}$ to m^{0}
(d) Ion pickup (newly ionised neutrals)	Ions that are newly exposed to solar wind start moving according to the electromagnetic force of the solar wind.	outer exosphere Mars, Venus	m^{0}
(e) Local electric & electromagnetic energisation (ions)	Field-aligned potential acceleration (DC field) and wave-particle interactions (AC field).	magnetosphere Earth>Mars>Venus	?
(f) Small-scale momentum transfer (neutrals & ions)	The energetic particles (both neutrals and ions, both from the Sun and the magnetosphere) spatter or interact with the atmosphere or plasma	above exobase Mars, Venus>Earth	m^{0}
(g) Large-scale momentum transfer (ions)	The solar wind dynamic pressure and electro-magnetic forces push the planetary plasma anti-sunward (e.g., instability, reconnection, and unknown cold outflow from Titan).	magnetospheric boundary Earth>Mars~Venus	m^{0}
(h) Magnetopause shadowing (ions)	The inner magnetospheric ion drift overshoots the magnetospheric boundary: (ring current and plasmasphere).	ring current or plasmasphere Earth	m^{0} *5
(i) Internal pluming process (neutrals & ions)	Detachment of bulk plasma or neutrals by internal process (volcanic eruption, ionospheric blob, plasmaspheric wind and plume)	exobase up to plasmasphere all planets	m^{0}
(j) Charge-exchanged neutral atoms	Ions with escape velocity are charge exchanging with cold neutrals and are no longer trapped by the magnetic field.	mirror altitude above exobase all planets	m^{0}

*1: for the source population just before the energisation (cf. §1.4).
*2: mass-dependency of the gained velocity by the energisation mechanisms (cf. §1.4 and §1.5).
*3: the exobase is cold due to CO_2 cooling (e.g., Gordiets and Kulikov, 1985). Small amount of light species at the exobase also makes the current escape rate from Venus small.
*4: ~exp(-k·m/T) where k is a constant determined by gravitational potential (Brinkman, 1970).
*5: when the finite gyroradius effect compared to the planetary size is ignored.

Swarm, for which the data assimilation with ground-based observations is essential.

The capability of ground-based facilities has considerably improved during the past two decades. Particularly, EISCAT_3D (http://www.eiscat3d.se), a new incoherent scatter radar system currently being designed to replace the single-point tristatic line observations of the current EISCAT mainland systems, will be a powerful tool, because it will continuously monitor a 3-D volume from 100 km to > 500 km altitude with a > 300 km diameter over northern Scandinavia (**Fig. 1.2**) where non-thermal escape is very active. The satellite footpoints will traverse a measurement volume (instead of passing at some distance from the radar line of sight in current systems). EISCAT_3D will measure scalar parameters including temperature anisotropy and estimate ion velocity vectors, with a basic resolution of 10 km (comparable to 1.5 sec resolution by the spacecraft) and can go down to 100 m resolution (comparable to 15 ms resolution by the spacecraft). EISCAT_3D is a European-lead international project, and is planed to start operation 2023 (cf. Annex-D).

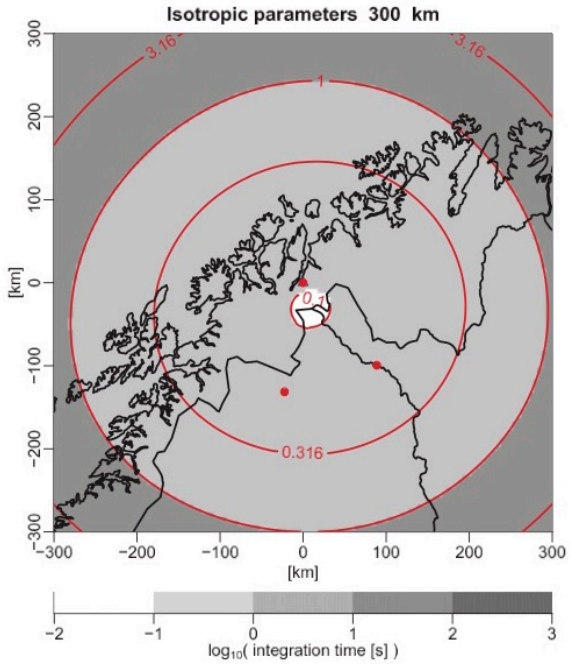

Fig. 1.2: Covering area of EISCAT_3D stage-1, which is planned to start operation in 2023 from three sites in Norway, Sweden, and Finland. A second stage with additional ground sites is planned to expand the coverage area. The shading represents the integration time to obtain scalar parameters (electron density, ion temperature and ion-electron temperature ratio) at 300 km altitude. Good quality data (integration less than 1 sec) is expected within a region of about 500 km diameter at this altitude (diameter >300 km at 500 km altitude).

The historical comparison is another advantage of the Earth. The rich database of the Earth's environment and of the Sun/solar wind monitor allows us to extrapolate new measurements to the past, with a good assessment of the likely external (Sun and solar wind) and internal (geomagnetic and ionospheric) conditions. The database includes even historical events that were derived from ^{14}C and ^{10}Be in trees and ice cores, such as the large solar proton event in AD 775 (Schrijver et al., 2012; Usoskin et al., 2013), for historical scaling.

1.2. Different types of escape and key regions

The various escape mechanisms summarised in **Table 1.1** are classified into two types: those mainly working on the neutrals and those specific to ions. The energisation mechanisms are quite different for neutrals and for ions: the former are mainly related to chemical reactions and collisions, whereas the latter are mainly related to the electric field including "resistivity" in plasma physics terminology (this is not caused by particle-to-particle interaction but by localised electromagnetic field that regulate individual particle motion). Conventionally, we call the former (chemical + neutral-neutral collisions) type "**thermal escape**" (hydrodynamic escape is categorised here) and the latter type "**non-thermal escape**" (charge exchange is categorised here). The neutrals are mainly lost by the thermal escape, while ions are mainly lost by non-thermal escape. With this categorisation, **understanding the relative importance between the thermal and non-thermal escape mechanisms under different driver conditions** is the most important target in the escape study.

Key regions for thermal and non-thermal escapes

The main driver for the thermal (neutral) escape is the solar EUV (10-120 nm) flux because it causes photochemical reactions (this includes subsequent chemical reactions) that convert irradiation energy to kinetic energies of particles in the upper atmosphere. **Table 1.2** shows major reactions that give N and O kinetic energy (there are hundreds more reactions (e.g., Rees, 1989; Tian et al., 2008), although the actual degree of photochemical heating has not been confirmed from observations even for these major ones. When the density is not very low, this energy is converted to a high temperature through collisions, and this collisional high-temperature region is called the **thermosphere** (> 80 km altitude for the Earth's case).

At some altitude where the atmosphere becomes thin enough, the energetic neutrals produced by the photochemical reactions may follow ballistic motion without collisions. This region is called the

exosphere, and the boundary between the thermosphere (collisional regime) and the exosphere (collision-free regime) is called the **exobase**. The neutrals with escape energy above the exobase, as listed in **Table 1.3**, will finally escape without any other help. From **Tables 1.2** and **1.3**, the photochemical heating is expected to be very effective for N and O escape from Mars but not from the Earth or Venus. However, the study of thermal escape largely depends on finding out the exobase conditions (density, gravity=altitude, and temperature), which may depend on the species, as well as the photochemical or other chemical activities in the exosphere.

In the thermosphere, the photochemical reactions also ionise neutrals to form the **ionosphere**, where the electromagnetic energy coming from space (ultimately from the solar wind) can be absorbed due to high electric conductivity (high electron density). Therefore, the lower part of the ionosphere is normally co-located with the thermosphere. The electromagnetic energy absorbed by the plasma will energise individual ions, part of which will escape by non-thermal mechanisms. The non-thermal energy conversion takes place where sufficient plasma exists, e.g., in the **plasmasphere**, and **magnetosphere**. The plasmasphere is a part of the magnetosphere, but unlike the magnetosphere, it is dominated by cold ions and can be considered to be the expanded ionosphere along the geomagnetic field. The plasmasphere does not exist around non-magnetised planets, like Mars or Venus.

Need for simultaneous studies of thermal and non-thermal escape

The difference in the atmospheres of the Earth, Venus, Mars, has been traditionally (during 1970's) explained by the difference in the Jeans escape, rather than considering the unique evolution of the Earth's atmosphere. However, these explanations are not quantitatively sufficient to explain the water loss from both Venus and Mars compared to the Earth as mentioned in §1.4. Furthermore, knowledge on the exosphere that is the basis for modelling of the thermal escape (and photochemical mechanisms) is very poor as described in §1.3.

In 1989, the Soviet Phobos-2 spacecraft found massive non-thermal ion escape from Mars (Lundin et al., 2000; 2013; Ramstad et al., 2013). This opened up the possibility that non-thermal escape could play a significant role in the loss of water from non-magnetized planets, triggering many relevant studies on the evolution of the planetary atmospheres. Those include dedicated Mars/Venus missions (such as Russian (failed) Mars-96, Japanese (failed) Nozomi, ESA's Mars Express, Venus Express and US MAVEN), analyses of non-dedicated satellite data (such as Akebono, Polar, and Cluster for Earth, and Cassini for Titan and Enceladus), as well as models. The observations have shown that non-thermal (ion) escape of heavy ions is indeed important at all planets, but the study is incomplete particularly for the Earth because no past mission is optimised for comprehensive understanding of the escape from the Earth (cf. §1.5).

To obtain the entire quantitative picture of the atmospheric escape, we need a coordinated investigation of both thermal and no-thermal escapes. While the majority of ion escape can be directly measured with modern reliable plasma instruments with mass separation ability of N and O, the energy distributions of the low-energy neutral atoms/ molecules around the escape energy is difficult to measure, because neutrals must be first ionised inside the instrument in order to determine their energies by electric or magnetic methods. At present, all energy spectrometers for neutrals at < 100 eV are too heavy or have a too low sensitivity for space missions, and it is not realistic to directly measure the escaping neutrals.

Fortunately, the thermal escape can be modelled from the altitude profile of the temperature and densities of major species in the exosphere and near the exobase, by assuming the velocity distribution of the superthermal part (Brinkman, 1970). We take this alternative method. Here, we note that the exospheric temperature, which should be theoretically constant due to the collision-free definition, might not be constant due to temporal variations and local heating (cf. §1.3).

In summary, a comprehensive observation should include:

* Cold ion and neutrals measurements in the ionosphere, exosphere, and near the exobase.
* Plasma measurements in the magnetosphere, ionosphere and plasmasphere.

Table 1.2: Major heating for N and O.

before		after	extra energy
O_2^+ + e-	→	2O	1–7 eV
N_2^+ + e-	→	2N	3–6 eV
N + O_2	→	NO + O	2–4 eV

cf. Tian et al., 2008 for complete list.

Table 1.3: escape velocity (km/s) and energy (eV).

height	500 km				2000 km			
	km/s	O	N	D,H_2	km/s	O	N	D,H_2
Earth	**10.8**	**9.7**	**8.5**	**1.2**	**9.8**	**8.0**	**7.0**	**1.0**
Venus	9.9	8.2	7.2	1.0	8.9	6.7	5.8	0.8
Mar	4.7	1.8	1.6	0.23	4.0	1.3	1.1	0.16

Importance of the variability

Considering the long time "evolution" of the atmosphere, we need to be able to estimate the amount of escape under driver conditions that are similar to those in the distant past, for both (non-thermal) ions and (thermal) neutrals. This requires observational knowledge of the variability as well as the average values. The past observations indicate that the non-thermal ion escape varies by more than 3 orders of magnitudes within a few days as shown (cf. **Fig. 1.1**, Cully et al., 2003; Peterson et al., 2008). Even the loss through the ion-pickup, which is strongly related to exospheric density, changed by more than one order of magnitude within a day (Yamauchi et al., 2015). The historical records of the Earth show that already a 1000 year scale is long enough to experience more variability in the drivers condition than that during the space age by two orders of magnitude, such as the proton event in AD 775. This proton event was two orders of magnitude stronger than the largest proton events observed during the last several decades (Schrijver et al., 2012; Usoskin et al., 2013). These facts stress that the Jeans escape and photochemical escape, which have been assumed to be relatively constant, have strong variations in both space and time.

Therefore, our target includes also the following information:

(a) average amount of escaping flux for each species for different escape (energisation) mechanisms,

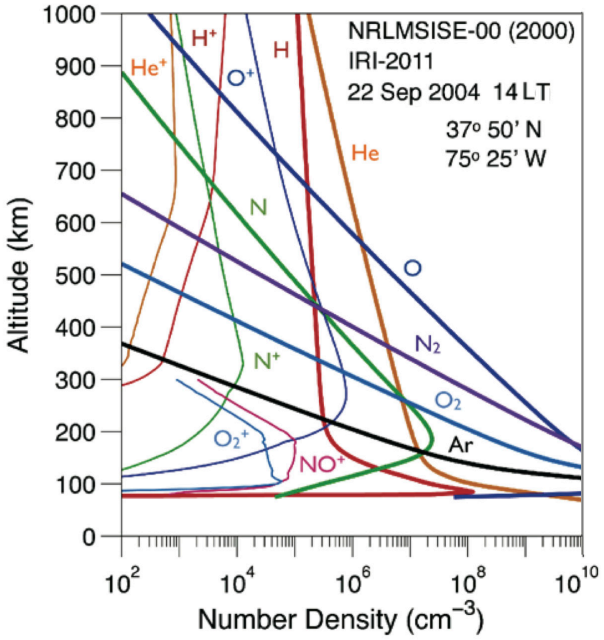

Fig. 1.3: Example altitude profile by the International MSIS model (Johnson, 1969; Pfaff, 2012). The smoothness of the profile (nearly exponential above 200 km for neutrals) comes from lack of observations.

(b) their variability including the range and time scales during different external (solar, solar wind and magnetospheric) and internal (ionospheric, thermospheric, and exospheric) conditions, and

(c) role of big solar events, e.g., whether small numbers of big events account more than the long time duration of normal events.

For the thermal escape, we plan to examine the spatial distribution and temporal variability of both the background neutral/ion conditions of the exosphere and upper ionosphere including the isotope ratio. For the non-thermal escape, we must know the ion flux resulting from the various escape mechanisms in the magnetosphere. The knowledge to be obtained by ESCAPE will help to assess the large-scale and long-term changes, including the time scale of planetary evolution.

1.3. Present knowledge of the exosphere is not sufficient

As mentioned before, knowing both the average conditions of the exosphere and exobase (including its altitude) and their variability (in both space and time) are essential in modelling the thermal escape including photochemical processes that contribute such exospheric conditions. The observational knowledge of the exosphere at different solar and geomagnetic conditions is also important for estimating the ion population that seeds the non-thermal escape through the ionisation of exospheric neutrals. The required knowledge includes the altitude profiles of the temperature and densities of all major species, as well as the ionisation and neutralisation efficiencies. The latter is also needed because the actual ionisation and neutralisation efficiencies in the exosphere are most likely different from the values used in the present models of the exosphere.

Lessons from the thermospheric studies

According to recent studies of the thermosphere by GUVI limb observations (at 120-180 nm range) from NASA's TIMED mission, which is designed for 110-310 km altitude range (Meier et al., 2015), the current empirical models of the exosphere and upper thermosphere such as the MSIS model (e.g., **Fig. 1.3**) are quite outdated and not suitable for any solid application such as modelling of the thermal escape. The TIMED/ GUVI result is even different from the estimate by ground-based observations of airglow (Bishop et al., 2004).

The GUVI data show large variability of neutral temperature and O, N_2, and O_2 densities, responding to both the solar EUV and the magnetospheric activity. These observations are significantly different from the predictions of the MSIS empirical

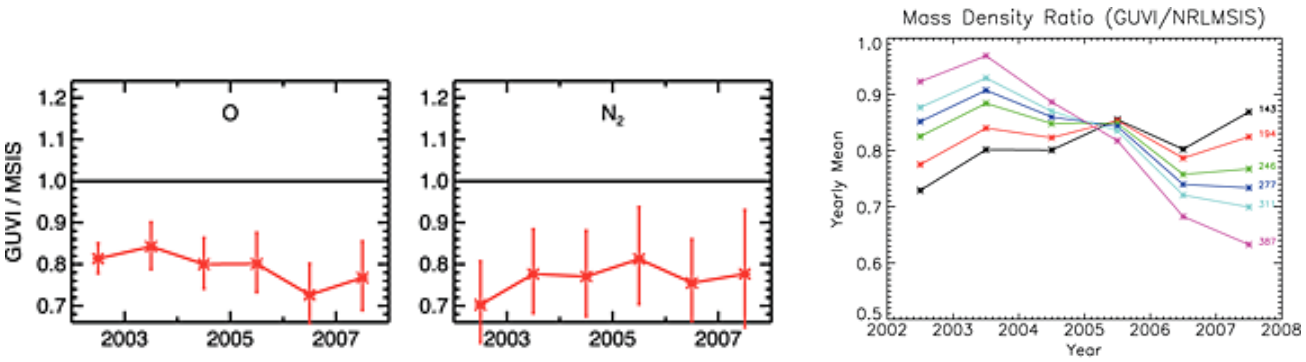

Fig. 1.4: Left: Ratio of GUVI observation to the NRLMSIS empirical model at 194 km altitude for geomagnetically quiet condition. Right: Mass density ratio (observation/model) at different altitudes from 143 km to 387 km (Meier et al., 2015).

model (Picone et al., 2002) or other models (e.g., Gordiets et al., 1982, Tian et al., 2008). Even the baseline densities of the most abundant species (O and N_2) are 20-30% lower in the observation than the empirical model, while the temperature is in principle estimated from the density gradient (scale height). The discrepancy changes from year to year as shown in **Fig. 1.4** (Meier et al., 2015).

The GUVI data also show strong structuring of density and particularly temperature within 5° in latitude during geomagnetic storms, while the model predicts essentially constant density (less than factor of 2 change). During these geomagnetic storm periods, the temperature nearly doubled and the N_2 density changed by one order of magnitude increase in within 10 days, presumably because of particle injections from the magnetosphere.

Table 1.4: Relevant recent missions (mostly active > 2000) at Earth's exosphere and mass separation.

Mission	UV instrument	Particle instrument
IMAGE	Lyman-alpha	ENA
TWINS	Lyman-alpha	ENA
GOES	Lyman-alpha	hot ions
TIMED*1	multi-wavelength	
Hisaki*2	multi-wavelength	
Polar		hot ions
Cluster		hot ions
Akebono		cold ions with N/O separation, hot ions
e-POP *3		cold ions with N/O separation

*1: The mission is targeted to the thermosphere and density (emission) threshold is set high for exosphere
*2: Detected as contamination from exosphere in the observations of the planetary atmosphere
*3: Science module on CASIOPPE satellite, 330 km x 1400 km orbit.

Lessons from the available exospheric H data

Unfortunately, no systematic observations of the exosphere have been performed for the major species (O, N_2, O_2, N) in the past. **Table 1.4** summarises the recent Earth missions with the capability of observing exospheric neutral density. The table also includes satellite missions that had ion instruments suitable for detecting non-thermal ion escape. Before the missions listed here, DE-1 (launched 1981was is the only spacecraft that had Lyman-alpha measurements and plasma measurements.

So far, no mission in the exosphere made in-situ neutral measurements with good mass-separation, except those in 1970's with an upper altitude limit of 800 km by OGO-5 (Bertaux and Blamont, 1970; Vidal-Madjar, 1978) and the series of Atmosphere Explorers at < 400 km altitude. Otherwise, the exospheric density has only been derived from UV data (e.g., Østgaard et al., 2003), while missions with UV spectroscopy (other than Lyman-alpha) were not designed for exospheric observations, and we can only use the Lyman-alpha channel for hydrogen emission from the available UV data in the exosphere at > 500 km. Consequently, the data are patchy and insufficient for modern modelling even at < 800 km altitude.

The available UV observations of exospheric H (sometimes called the H corona) show that the exosphere is not as simple as predictions by any models and has large variability in both space and time, as actually expected from the thermospheric studies. The H distribution derived from the line-of-sight stereo observations by the two TWINS spacecraft (**Fig. 1.5**) shows that both the average density and the localised structure of the neutral H changed significantly within two years, i.e., the altitude of the same density changed by more than 1 R_E (Zoennchen et al., 2013, 2015). The variation of the altitude profile indicates a large change in the escape velocity according to **Table 1.3**. The day-night asymmetry is also larger than the expected

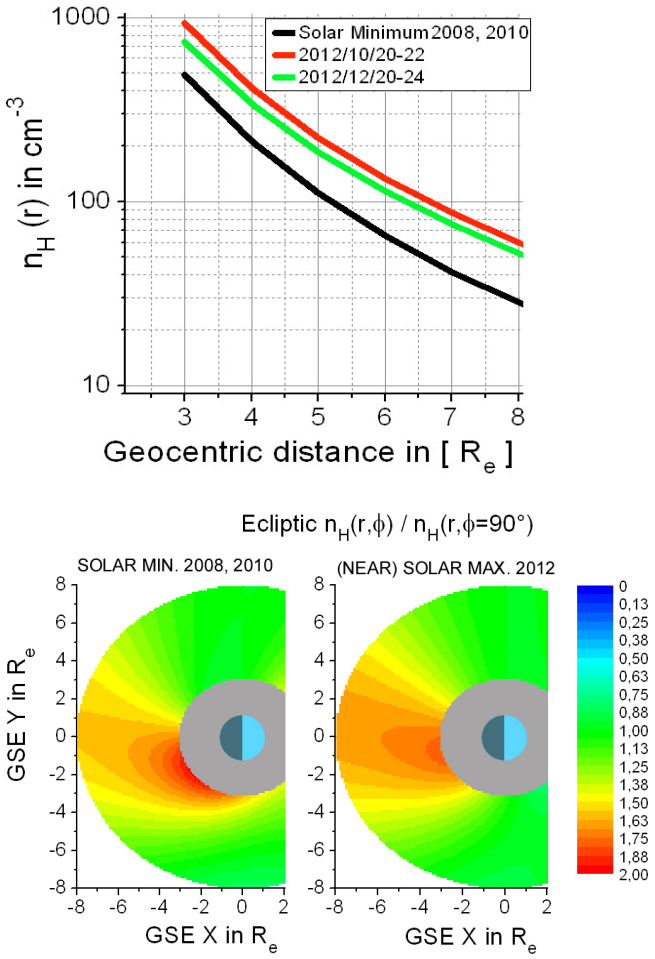

Fig. 1.5: Exospheric hydrogen density that is model-fitted from Lyman-alpha line-of-sight stereo observations by the two TWINS spacecraft (Zoennchen et al., 2015). The smoothness of the profile comes from the model fitting, and therefore only the relative difference between different solar cycle phases and different local times are reliable. Top: Average density profile over geocentric distance. Bottom: Relative density compared to the dusk value for each geocentric distance.

asymmetry even after taking into consideration of the solar radiation pressure (Beth et al., 2016).

More recently, the solar cycle variation of the dayside H density distribution was derived from TIMED/GUVI (Lyman-alpha) limb observations from about 200 km to about 2 R_E (Qin and Waldrop, 2016). The exosphere is found to be very extended and the derived scale heights for H are much larger than conventionally expected. The result suggests that fundamental efficiencies such as the collisional thermalisation and/or non-thermal energisation (e.g., charge exchange) might have to be revised. Furthermore, the solar cycle dependence of the density scale height is opposite to that predicted by semi-empirical models such as MSIS. The actual H escape flux might significantly exceed thermal Jeans escape from the current model of the thermosphere (Qin and Waldrop, 2016), and the high velocity tail of the kinetic distribution function may have different profiles from what is traditionally assumed (Brinkmann, 1970; Tinsley et al., 1986; Tian et al., 2005, 2006).

The variability of the exosphere is also observed at Mars by Hubble Space Telescope (HST) and Mars Express UV data (exospheric temperature), ion data (density of newly ionised exospheric H outside the bow shock), and magnetic field data (ion cyclotron waves that are excited by these newly formed ions) (Bertaux et al., 2006; Bertucci et al., 2013; Chaffin et al., 2014; Clarke et al., 2014; Bhattacharyya et al. 2015; Yamauchi et al., 2015).

Due to the slightly elliptic orbit of Mars around the Sun, radiation flux increases by 40% from aphelion to perihelion. However, the observed seasonal (aphelion-perihelion) variations of the Lyman-alpha brightness of the exospheric origin is larger than the expected variations. According to the Mars Express ion data, the density variation of the newly ionised exospheric hydrogen changed by one order of magnitude between aphelion and perihelion, and this variation is more evident than the solar cycle variations, as shown in **Fig. 1.6**. Furthermore, the ion density occasionally changed by more than a factor of 3 (nearly 10) within a half day (Yamauchi et al., 2015). These observations indicate that the exospheric density is not solely determined by the solar EUV, and there might be additional controlling factors. Coupling with the lower part of the atmosphere is one obvious candidate.

In summary, recent patchy observations of the exosphere show that the observed H distribution is quite different from the semi-empirical exospheric models (e.g., those using hydrostatic and constant distribution), with larger variability in both space and time than any model could predict, and that there is other factor than EUV that controls the exospheric condition. These discrepancies affect the modelling of thermal escape.

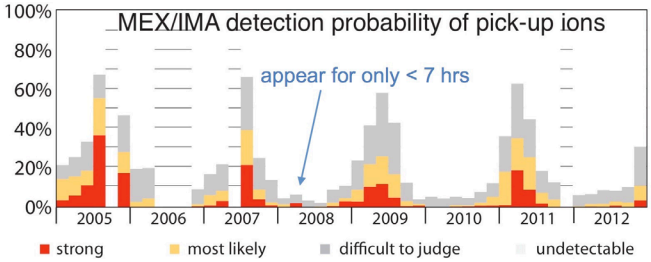

Fig. 1.6: Probability of observing newly ionised exospheric hydrogen as measured by Mars Express IMA instrument. Different categories indicate an intensity difference of more than a factor of 3. The peak that repeats every two years corresponds to Martian perihelion (Yamauchi et al., 2015).

How can we improve our observational knowledge?

For better estimate of thermal escape, a systematic investigation of the exosphere is needed for species other than H (many Lyman-alpha study exist), particularly for the most abundant components O and N_2 (cf. **Fig. 1.4**). Accordingly, current standard model of the exosphere such as NRLMSIS must be significantly revised. New models must also take into account the dynamic and non-uniform nature of the exosphere. We note that the variability can be different for different species (H, O, N_2). One should also measure both ions and neutrals to understand the actual production of ions and their recombination, i.e., net ionisation rate.

There are two major methods to measure density. One is EUV-UV spectroscopy (like TIMED GUVI for UV range and Hisaki satellite for EUV range) to obtain line-of-sight integrated values. However, this method provides only the column density but not the local density, and smears away fluctuations along the line-of-sight. The other method is in-situ measurements by neutral and cold ion instruments. The best option is to combine both methods. If the line-of-sight direction of a spacecraft traversal includes its trajectory and if the temporal variation is not significant during that traversal (approximately < 5 hours between the remote and in-situ observation, cf. §4.1), the spatial and temporal structures can be separated along the traversal. In addition, these two methods can provide cross-calibrated values.

1.4. Lack of fundamental physics/chemistry knowledge on atmospheric escape

In the relationship between the exospheric conditions and atmospheric escape, two fundamental processes must be taken into account. One is the ionisation/neutralisation processes (neutralisation includes both recombination and charge-exchange). The balance between the ionisation and neutralisation efficiencies determines the actual ionisation rate. The other is the isotope fractionation processes (mass-filtering processes) that determine the isotope ratios of the escaping species (cf. **Table 1.1**).

Ionisation-neutralisation efficiencies in space: need for simultaneous observation of cold ions

The model-observation discrepancy mentioned in the previous section may also affect the modelling of the non-thermal escape rate by influencing the ion production rate in the exosphere, because the produced ions at the altitude of the exosphere are affected more by the electromagnetic field rather than collisions or gravitational force, and can easily contribute to the non-thermal escape. The ionisation and neutralisation are also important in the photochemical (recombination) energisation because the ions are expected to have an initial energy of about 1 eV before the reaction and the escape energy at the exosphere altitude is lower than that of the thermosphere (cf. **Table 1.3**).

The problem is that the net ionisation rate, as the result of ionisation and neutralisation, is most likely different between the exospheric environment and the laboratory. The thermospheric study, as mentioned in the previous section, indicates that the ionisation and neutralisation efficiencies at thermosphere/exosphere environment are different from those in laboratory experiments or quantum chemistry calculations. The "non-ionised" hydrogen distribution in the nightside exosphere in **Fig. 1.5**, which is generally explained by the quick photo-ionisation of hydrogen in the morning and slow recombination of co-rotating protons in the darkness, also raises the same suggestion that the difference between the solar minimum and maximum may not be explained only by the solar UV flux.

One possible causes of this discrepancy in the ionisation/neutralisation efficiencies is the existence of many different plasma population in space, because precipitating ions/electrons are considered to influence the thermospheric temperature, as mentioned §1.3 (Meier et al., 2015). Another possible cause is the various types of electromagnetic waves that together control the dynamics of low energy ions in different manner from laboratory (Alfvén and Fälthammar, 1963; André and Yau, 1977), and may influence both the recombination rate and the charge-exchange rate of low-energy ions. The resultant coherent ion motion (e.g., plasma wave and convection) may also affect the dynamics of neutrals through weak but non-zero collisions (Allen et al, 2000). These possibilities have never been examined by measurements in space.

The model-observation discrepancy in the exospheric density and temperature indicates that our theoretical understanding of the ionisation rate is not sufficient to use as the basis for the atmospheric escape modelling. Therefore, the net ionisation rate must be observationally obtained. Thanks to technology developments, densities of cold ions and cold neutrals can now be measured with light-weight space instruments. By measuring the ion density and neutral density simultaneously at the lower exosphere/upper ionosphere (> 500 km for ESCAPE), we can obtain basic information on the ion-neutral interaction (ionisation, neutralisation, and/or charge-exchange in the exospheric environment for different driver conditions).

Isotope ratios as indicators of past escape

The isotope ratios of planetary and solar materials have been used in estimating the formation of the

solar system bodies. Although the isotope ratio of the solar system bodies are subject to secular changes, the combination of isotope ratios of different elements made it possible to classify the solar system into three groups in terms of fractionation of the isotope ratios (e.g., Füri and Marty, 2015). Since the initial composition is considered similar between the Earth, Venus, and Mars, the present isotope ratio of these planets must reflect the fractionation process during planetary evolution over 4.5 billion years. There are three major processes that might change the isotope ratio of a planet: exposure to the solar wind (which corresponds to proto-solar nebula's values), bombardment, and atmospheric escape. For the escape process, the degree of the isotope fractionation depends on the size (gravity) of the planet (Jakosky et al., 1994; Robert et al., 2000; Robert, 2006; Chassefiere and Leblanc 2004; Fedorova et al., 2008; Marty et al., 2011), if we ignore the biological fractionation mechanism that works only at the Earth (e.g., Guy et al., 199; Luz e al., 1999).

The escape energy of atoms/molecules from a planet/satellite is proportional to the planetary mass and the gravitational potential (inversely proportional to the distance from the planetary centre), as shown in **Table 1.3**. This makes it easier for light isotopes to escape than heavier isotopes ("gravity-filtering"), and the heavy/light isotope ratio of the remaining atmosphere increases in time no matter what is the escape mechanism. This is how the isotope ratio has been used as a qualitative measure of the total atmospheric loss as compared to the original inventory.

For example, the $^{15}N/^{14}N$ ratio of the Martian atmosphere is higher than that of the Earth or Venus (cf. **Fig. 1.7**), or even that of the Mars-origin meteorite (by a factor of about 1.6). This difference is interpreted as a consequence of more nitrogen escape at Mars than at Earth or Venus due to more efficient photochemical and hydrodynamic escapes of nitrogen under lower gravity of Mars (cf. **Figs. 1.2** and **1.3**; Lammer et al., 2008; Chassefiere and Leblanc, 2004). The extremely high D/H ratio of the Venus atmosphere, by a factor of about 240 compared to the Earth (e.g., Fedorova et al., 2008), and the relatively high D/H ratio in the Martian atmosphere compared to those of the Earth or Titan (cf. **Fig. 1.7**) have been attributed to a huge loss of hydrogen during the long duration of expanded hot exosphere (Kulikov et al., 2007; Airapetian and Usmanov 2016).

However, this argument is only qualitative, and we cannot quantitatively model the amount of isotope fractionation by atmospheric escape, or quantitatively compare between different planets, because the degree of isotope fractionation is different for different escape mechanisms. In the above argument, the present Venus D/H ratio predicts only a < 10 m depth of an ocean on the ancient Venus (as the total loss of the water), if the gravity-filter of thermal escape is assumed and if photo-dissociation processes did not fractionate D and H significantly (Bertaux et al., 2007; Fedorova et al., 2008). The total loss of only < 10 m depth water is one to three orders of magnitude less than the ocean depth on the Earth.

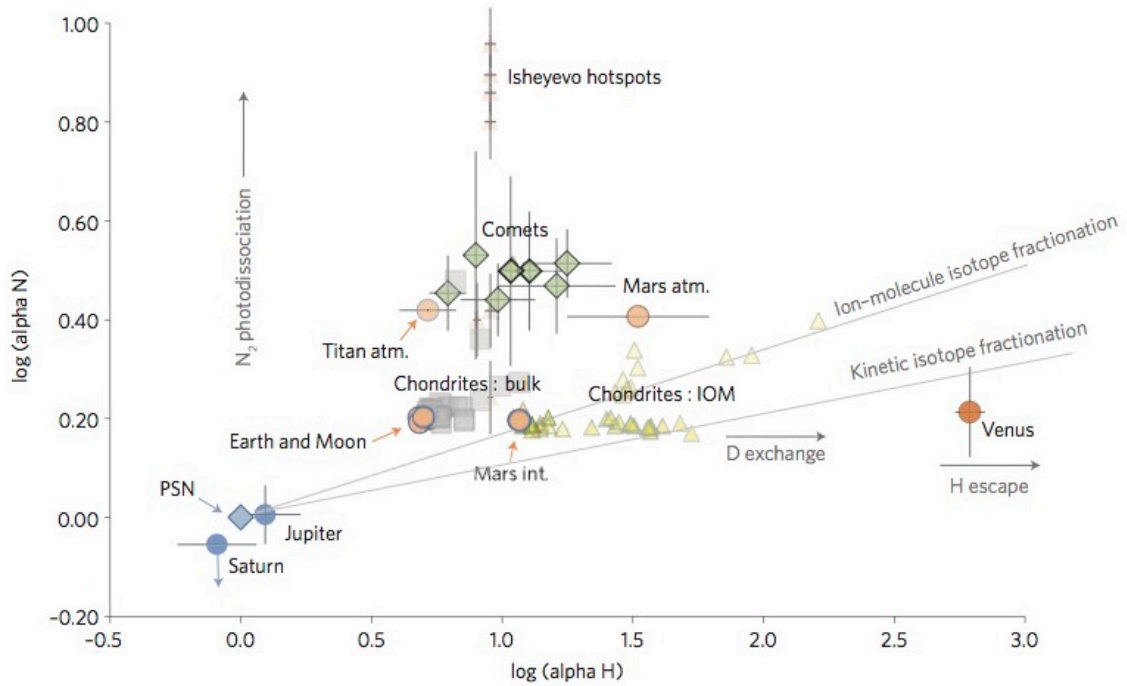

Fig. 1.7: Planets classified by isotope ratios (Füri and Marty, 2015). Alpha H and alpha N are defined as the D/H and $^{15}N/^{14}N$ ratios normalised to the protosolar nebula values (2×10^{-5} for D/H and 2.3×10^{-3} for $^{15}N/^{14}N$ (Robert et al., 2000; Marty et al., 2011). Lines indicate theoretical fractionation during planetary formation.

If a non-thermal escape mechanism with a much smaller isotope fractionation effect contributed more than the thermal escape, the extremely high D/H ratio of the current Venus would mean more total loss than estimated, resulting in more water loss than the estimation assuming the thermal escape only. This argument also applies to Mars, where the current estimate of thermal escape (from the D/H ratio) means extremely small total water loss.

Similarly, the high $^{15}N/^{14}N$ ratio of the Martian atmosphere mentioned above does not necessarily preclude contributions from escape mechanisms other than the photochemical escape, such as non-thermal escape and hydrodynamic escape (cf. **Table 1.1**) during the past 4.5 billion years. Hydrodynamic escape, which is originally triggered by photochemical heating (Kasting and Pollack, 1983; Tucker and Johnson, 2009), can either select a specific mass or might drag an entire group of similar mass atoms through collisions, and might have worked for heavy species at the Earth.

Thus, just a rough estimate of the past hydrogen losses from Mars and from Venus requires the evaluation of the degrees of mass-filtering for major escape mechanisms. The Earth's case is even more complicated because the flux of the non-thermal escape is found to be larger than those of Mars or Venus (Nilsson et al., 2010, 2012; Nordström et al., 2013; Slapak et al. 2013, 2015). This is because the acceptance area of the solar wind energy to the thermosphere/ionosphere significantly increased by the geomagnetic field.

Isotope fractionation during the escape processes

So far, we have very poor knowledge of the degree of the isotope fractionation effects for all escape mechanisms, including the thermal escape. The difficulty partly comes from the fact that the gravity-filter of the mass is just one of the fractionation processes that operate during the escape. The actual fractionation is determined by a combination of three factors: **(a)** the difference in the supply rate of atoms from molecules, **(b)** the difference in the reference altitude at which each escape process start operating, and **(c)** the mass-dependency of the effectiveness of each mechanism.

For (a), the supply rate is mainly determined by the effectiveness of photo-dissociation and isotope exchange (e.g., associated with water), but modelling the supply rate is still far from accurate even though the photo-dissociation and isotope exchange rate are known relatively well (e.g., Rees, 1989; Robert, 2006; Tian et al., 2008). For (c), a rough estimate is possible as listed in the 4th column of **Table 1.1**, but some mechanisms (like wave-particle interaction) are extremely difficult to model without observation-based statistics (e.g., by measuring the energy and flux of N^+ and O^+ for strong mass-filter cases, and He^+ and O^+ for weak mass-filter cases). On the other hand, the reference altitude is very difficult to evaluate (3rd column of **Table 1.1** shows rather broad altitude ranges). Here is a simple estimate showing how the reference altitude is important.

In the hydrostatic assumption (pressure gradient is balanced by gravity), the pressure scale height h is inversely proportional to the mass of atoms/molecules (for pressure H, D, ^{16}O and ^{18}O, $h_H = 2*h_D = 16*h_{16} = 18*h_{18}$), and $h_H \sim 300$ km for the Earth's atmosphere (this is slightly larger in the exosphere due to higher temperature). If an atmospheric layer of thickness h_H is hydrostatic, the pressure of D, ^{16}O, and ^{18}O decrease by e^{-2}, e^{-16} y e^{-18}, respectively, and hence the pressure ratio P_D/P_H decreases by e^{-1} and P_{18}/P_{16} by e^{-2}. A vertical thickness of 300 km is much thicker than the stratosphere, but is no longer thick in the exosphere. Here, the temperature ratio between different species does not normally change very much with altitude, and hence the pressure ratios normally have the same altitude profiles as the density ratios.

If the exosphere and thermosphere are stratified mainly by gravy, we expect a large difference in the isotope ratio between the upper layer (e.g., 2000 km) and near the surface. In such a case, the altitude of the starting location of the escape determines the majority of the isotope fractionation rather than the mechanism itself. The situation could have been more extreme during ancient times, when the ionosphere and the thermosphere expanded under much higher solar EUV flux than in the present time by one order of magnitude (Wood, 2006; Yamauchi and Wahlund, 2007; Airapetian and Usmanov, 2016).

Expected variability in the isotope ratio

On the other hand, it is questionable how much the hydrostatic assumption is applicable. The thickness of the hydrostatic layer at high altitude can be non-uniform and variable, e.g., by the convection. It is quite possible that the exosphere has large-scale convection with some variability. The observation by TWINS and TIMED indeed indicate that exosphere and thermosphere are non-uniform and changing (Zoennchen et al., 2011; 2013, 2015; Meier et al., 2015). Accordingly, we expect isotope fractionation to be variable in both space and time. In fact, MAVEN recently detected a dynamic change in the D/H ratio, as shown in **Fig. 1.8** (Clark et al., 2016), and so we may no longer assume that the isotope ratio is constant in the Earth's exosphere. Thus, the isotope measurements will provide information on the dynamics below the observation altitude.

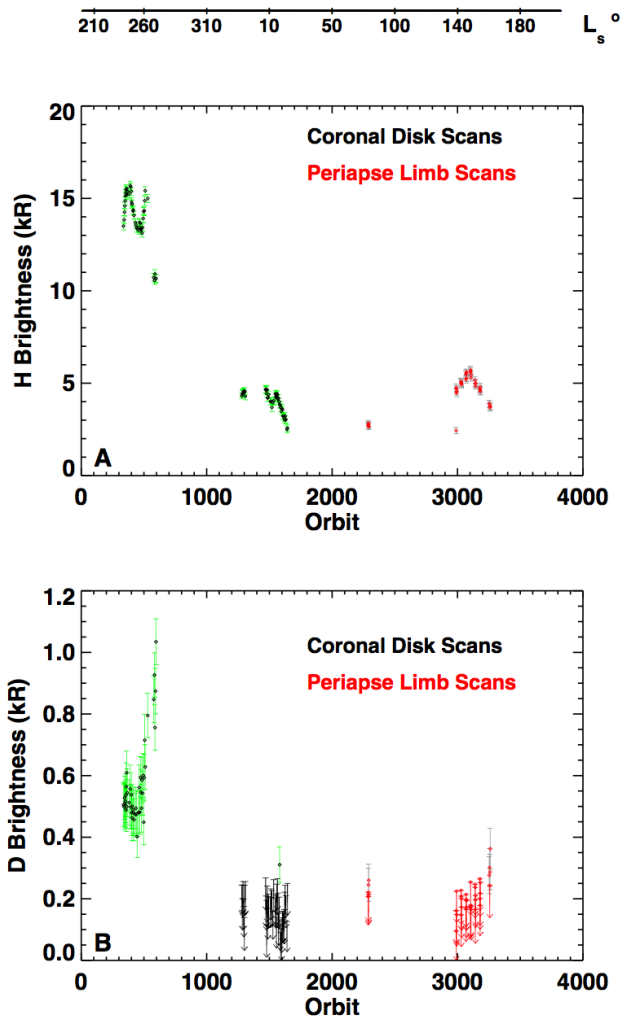

Fig. 1.8: MAVEN observation of H and D in the Martian exosphere. The variations of H and D are different, indicating changes in the D/H ratio in time (Courtesy by John Clark; Clark et al., 2016, submitted to JGR).

Since the ions and neutrals obey different dynamics (electromagnetic field for ions and collisions and gravity for neutrals), the effective thickness of the hydrostatic layer should be different between ions and neutrals. Therefore, we expect the same isotope ratio between ions and neutrals only if the cold ions are formed locally. If ions are filled from much lower altitude, the isotope ratio will be different between the cold ions and neutrals, and in that case, the isotope fractionation for the non-thermal escape becomes relatively small.

Need for isotope ratio measurements

The isotope ratio is thus a fundamental parameter to understand the past and present atmospheric processes including escape. Just knowing the difference in the isotope ratios between near the surface and near the exobase helps in estimating the isotope ratio of the escaping atoms, ions, and molecules. Such direct observations are needed to correctly model and understand the origin of the isotope ratios and to estimate the past history of other planets and moons.

So far, no past mission measured the isotope ratio in a systematic manner. Even the altitude dependence of the isotope ratio of the neutral atmosphere or ionosphere has never been measured. This is in contrast to the other solar system bodies: the space instrumentation is already available and has actually flown to other environments (e.g., ROSETTA and MAVEN). To fill this gap, ESCAPE will include light-weight high $M/\Delta M$ instruments to perform the first systematic isotope measurements in the geospace environment.

1.5. Need for simultaneous observation of the non-thermal escape with N/O separation

In order to understand the atmospheric escape and evolution of atmospheric composition, a good estimate of both the thermal and non-thermal escape is mandatory. In particular, the thermal/non-thermal escape ratio under different driver conditions is important from a biology viewpoint because this ratio actually fractionates the atmosphere and potentially influence the composition such as the pH and N/O ratio, as described in §1.1. The best strategy is to measure the non-thermal escape simultaneously with the exospheric observations to compare them under the same driver conditions.

Furthermore, although there are many observations, no past mission was optimised for coordinated observations of ion escape. As the result, our knowledge of the non-thermal escape from the Earth is still patchy. For example, measurements at higher altitudes provided larger escape values (Peterson et al., 2006, 2008; Slapak et al., 2013): nearly 10^{24} ions/s were measured at < 10000 km altitude (FAST, Akebono, Polar) but over 10^{25} ions/s were measured at > 6 R_E. (Cluster, Polar). This is probably because of the limited energy ranges of the instruments: Measuring cold (< 5 eV) ions and

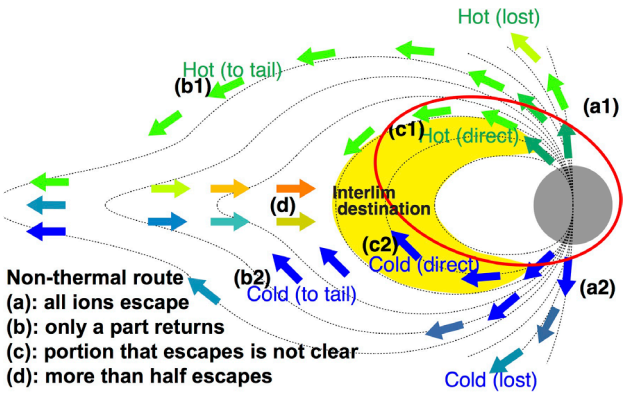

Fig. 1.9: Major routes for escaping ions. The red ellipse indicates the proposed orbit of ESCAPE.

measuring hot ions require different techniques, with independent instrumentation, but most past missions had only one of those (cf. **Table 1.4**). Only DE-1 (launch 1981) and Akebono (launch 1989) had the capability for both, but they used old technology not optimised for escape studies.

Major destinations of outflowing cold and hot ions from the ionosphere

To have a good observation of ion escape, including the estimation of what fraction of outflowing ions from the ionosphere actually escape, the spacecraft must cover a wide range of altitudes and latitudes, because the fate of the outflowing ions is quite complicated for the Earth compared to Mars or Venus. **Fig. 1.9** shows major routes of heavy ions once they have left the ionosphere.

(a) Ions outflowing through the cusp and the dayside part of the polar cap enter the magnetosheath (either directly or through the plasma mantle) to completely escape (Nilsson et al., 2013; Slapak et al. 2013). This works for both cold and hot ions. The instantaneous escape value reaching 10^{27} ions/s (cf. **Fig. 1.1**) refers to this part only.

(b) Ions (both hot and cold) flowing in the lobe region reach the magnetotail plasma sheet, where a part of them returns to the Earth ((d) in the figure) while a majority flows tailward, either steadily or as a plasmoid (e.g., Hones, 1974). With much smaller area of orbital coverage and lower energy coverage than tailward flowing heavy ions, Seki et al (2001) reported a decrease of the tailward flux of heavy ions with distance, and interpreted this decrease as return to the Earth, but no direct observations to date have reported the hypothesised high flux of the Earthward flowing ions. Instead, recent Cluster's direct measurements of returning heavy ions show that the returning amount is much smaller than the outflowing amount (Nilsson et al., 2016).

(c) Some ions directly enter the inner magnetosphere. Most of them are cold, with some warm (< 1 keV) ions mixed. In a limited local time and latitude range in the inner magnetosphere, a region of dense cold ions, the plasmasphere, exists, and the majority of these cold ions are filled from ionosphere (Lemaire and Gringauz, 1998). If these ions stay inside the magnetosphere, it obeys the ExB drift (Liemohn et al., 2004), but it is not clear what fraction of these returning ions escapes.

(d) The returning part from the magnetotail has a broad energy range from less than 50 eV to more than 100 keV depending on their initial location (local time), their energies, and the cross-tail electric field (e.g., Kronberg et al., 2014). Some are energised adiabatically or non-adiabatically (e.g., by shocks) to form the main part of the ring current (Ejiri, 1978; Ebihara and Ejiri, 2000; Yamauchi et al., 2009a; Luo et al., 2014), while some are transported simply as a fluid, such as the busty bulk flows (Angelopoulos et al., 1994; Cao et al., 2013) to form stripes of hot ions around 1 keV in the inner magnetosphere (Yamauchi et al., 2013). Both types have finite values of the magnetic moment that keep these ions bouncing inside the geomagnetic bottle unless the pitch-angle changes.

Need for simultaneous observation of the exosphere

To estimate the non-thermal escape, we need to evaluate the final percentage of escape for routes (c) and (d). This requires adequate information on the exosphere, because a substantial portion of these ions in the inner magnetosphere will charge-exchange with the exospheric neutrals. This must be compared with the other destinations, such as directly re-entering to the ionosphere. Past observations indicate that the trapped plasma along the geomagnetic bottle in the inner magnetosphere drifts according to magnetic drift and ExB drift, but their flux decays in time, with faster decay for sub-keV range than 10 keV range (Ebihara et al., 2004; Yamauchi and Lundin, 2006).

The decay of the flux of trapped ions in the inner magnetosphere is due to three major reasons: **(1)** some ions precipitate into the ionosphere after pitch-angle scattering (change of magnetic moment) through, e.g., wave-particle interactions, **(2)** some ions are converted to neutral after striping electrons (charge exchange) with exospheric neutrals (Brandt et al., 1999; Ebihara et al., 2001; Fok et al. 2014), and **(3)** some ions experience magnetopause shadowing, i.e., reaching the magnetopause during the drift motion and escape to the magnetosheath (Marcucci et al., 2004, Darrouzet et al., 2009). All these processes are relevant to both cold and hot ions all the time. For example, the magnetopause shadowing is important for both the ring current hot ions coming from the magnetotail and the plasmaspheric cold ions, and can occur both during quiet times (e.g., plasmaspheric wind (Dandouras, 2013)) and disturbed periods (e.g., plasmaspheric plumes that are detached from the plasmasphere (Pierrard et al., 2008)).

Among these three mechanisms, the majority of the precipitating ions return (with small amount of sputtering neutrals contributing to escape), and all the ions at the magnetopause escape, but the fate of ions that charge-exchange with neutrals (considering only neutral atoms is sufficient because molecules are very small fraction), can be both: **(2a)** If the source ions are cold (e.g., less than escape energy), the charge-exchanged neutrals remain in the exosphere. **(2b)** Even if the generated neutral atom after the charge

exchange has escape energy (we call neutral atoms with escape energy as "energetic neutral atoms" **(ENA)** in this proposal, and can be as low as 10 eV according to **Table 1.3**), it still returns to the atmosphere if the motion is downward at the time of charge exchange. **(2c)** If such ENA is moving upward at the time of charge exchange, it will escape because the mirror altitude is normally above the exobase and we can ignore collisions. Here, more than half of the produced ENAs are expected to escape into space (2b ≤ 2c) because the source ions are gyrating around the geomagnetic field.

Evaluating the relative importance between (1), (2), and (3) is the key for estimating the percentage of net escape in the inner magnetosphere, which includes all return flows from the magnetotail. Past satellite observations indicate that the precipitating ion flux is one order of magnitude lower than the outflowing ion flux (Moore et al., 1999; Yamauchi et al., 2005). Therefore, we need a good evaluation of the amount of (2). Unfortunately, measurement of neutrals below 0.5 keV is unreliable (no measurement exists for < 100 eV with energy analyses), while the flux of trapped ions less than 1 keV is quite large in the inner magnetosphere (Ebihara et al., 2008; Yamauchi et al., 2009b), and the measured amount gives only line-of-sight integration but not the local production. Therefore, a good time-dependent model of the exosphere and the charge exchange efficiency in the space environment (most likely different from laboratory values as mentioned in §1.3) are required for a more detailed estimation of the real contribution of the charge exchange process to the escape.

Another escape channel relevant to the exosphere is cold ion loss from the plasmasphere as mentioned above. Although the ionosphere is known to fill cold ions to the plasmasphere, the exosphere is also a candidate source region that directly provides plasmaspheric ions. One of the reasons for such a speculation is the high concentration of He^+ ions, accounting for approximately 5–10% of the plasmasphere plasma (Darrouzet et al., 2009). This suggests that it could be formed by charge-exchange with solar wind alpha (He^{++}) particles. Investigating the efficiency of such interactions (ionisation and recombination, or charge exchange) between the plasmaspheric ions and exospheric atoms is also important.

N/O ratio for diagnosing mass-fractionation during non-thermal escape

One of the missing elements in the past work on the non-thermal escape is the N^+/O^+ ratio of the escaping ions. There are observation of N^+/O^+ ratio for both cold ions by Akebono (Yau et al., 1993) and energetic > 30 keV ions by AMPTE (Hamilton et al., 1988), but these energy ranges covers a minor fraction of the escaping ions. These limited observations so far showed that the N^+ flux increases during major magnetic storms even more than the O^+ flux increases, as shown in **Fig. 1.10**. Since the increase of the O^+ escaping flux with solar UV flux and geomagnetic activity (Moore et al., 1999; Cully et al., 2003) is already by two orders of magnitude from nominal conditions to the geomagnetic storms during solar maximum (**Fig. 1.1**), the degree of increase of the nitrogen escape with these external drivers must be very drastic, and the actual degree is still unclear. It might be possible that the short total duration of big events of nitrogen escape may account more than the total nitrogen escape during the rest of the time. Also the fact that O^+/H^+ ratio increases with the geomagnetic activity (Cully et al., 2003; Peterson et al., 2006) indicates that the composition of the non-thermal escape must be different in the past when the external driver conditions are different from the present.

The independence of O^+ outflow and N^+ outflow is also expected from the different photochemistry between nitrogen and oxygen in the thermosphere, exosphere, and ionosphere (cf. **Table 1.2**), because the dissociation energy is different between N_2 (triple bonding: 9.8 eV binding energy) and O_2 (double bonding: 5.2 eV binding energy) while the ionisation energy is similar between atomic N (14.5 eV) and atomic O (13.6 eV). Since these two species are the most abundant atmospheric components, the N^+/O^+ ratio of hot ions that are actually escaping from the polar cap is important to diagnose the effect of atmospheric escape on the atmospheric evolution.

The knowledge of the N/O ratio of the escaping hot ions is also important in estimating the isotope-fractionation by the non-thermal escape mechanisms. While the isotope ratio of the seed (cold ion) population can be directly measured over a broad altitude range, it is not possible to measure the isotope ratio of hot ions (all other than cold ions) with the available resources of a spacecraft. Fortunately, the non-thermal acceleration is driven by the electromagnetic fields, which treat ions only by their mass and charge but not by the nuclear composition. For example, the non-thermal escape mechanism does not distinguish between D^+ and H_2^+ or CO_2^+ and N_2O^+. By examining the acceleration energy of N^+ and O^+, and by comparing the N^+/O^+ ratio of cold background ions and hot escaping ions, we can obtain a good picture of mass-filtering by the non-thermal escape mechanism itself.

We should also note that molecular nitrogen ion (N_2^+) is as important as atomic ion (N^+). While O^+ is normally formed from atomic O, N^+ is normally formed after N_2^+ dissociation due to the very different

chemical binding energies of N_2 and O_2. This means that the ionisation height and the dependency on the solar EUV and solar wind activity are quite different between these two abundant elements in the atmosphere, despite their similar molecular masses. Molecular nitrogen ions are actually observed (Craven et al., 1985; Yau et al., 1993) as shown in **Fig. 1.10**. Measuring the N/O ratio of escaping ions is thus important, but our current knowledge is far from sufficient, mainly because of the lack of proper instrumentation with N^+/O^+ separation and energy analysis in past space missions. Fortunately, such measurements are now possible, and ESCAPE will take advantage of these technological developments.

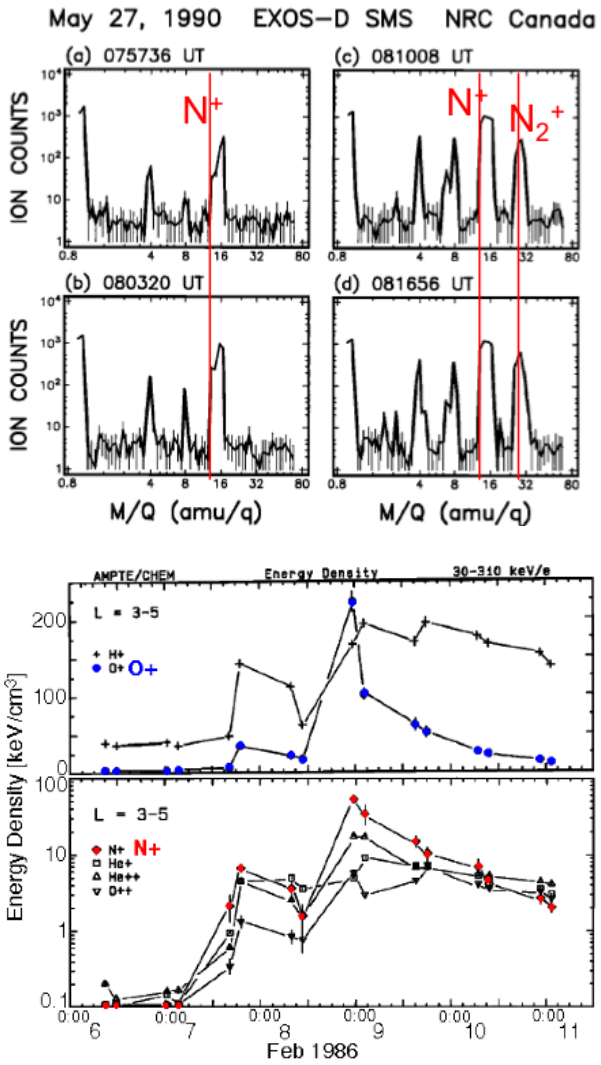

Fig. 1.10: (top) Akebono observations of cold ions at < 20 eV (SMS instrument, Yau et al., 1993), and (bottom) AMPTE observation of energetic ions at > 30 keV CHEM instrument, Hamilton et al., 1988): The broadening of M/q=16 in Akebono data is combination of N^+ and O^+, while no O_2^+, is detected in the N_2^+ channel. Both data sets indicate more dynamic change of N^+ compared to O^+.

1.6. What should be measured?

The science questions related to the atmospheric escape from the Earth are summarized as:

#1: What is the quantitative state of the atmosphere at altitudes of 500-2000 km?

- Exospheric altitude density profiles and temperature as a function of different drivers such as solar EUV, solar wind and geomagnetic conditions (§1.3)
- Establish isotope ratios for both neutrals and ions and compare them with those found at the Earth's surface and in other solar system objects. (§1.4)
- Exospheric altitude profile of ion/neutral ratios and estimate ionisation/neutralisation efficiencies (§1.4)
- Temporal and spatial variations of the density of major exospheric species (§1.3)
- Correlation of such variability with upper atmosphere parameters, and with different incident energies when particle precipitation is present (§1.3, §1.4)

#2: What are the dominant escape mechanisms, and their dependence on drivers?

- Estimate thermal escape flux for neutral and ion species for different conditions. (§1.3)
- Estimate the prevailing escape mechanisms and the relative importance of thermal or non-thermal escape for different driver conditions. (§1.2, §1.5)
- Estimate the response of the ionisation and neutralisation efficiencies, isotope fractionation and the N/O ratio to different drivers. (§1.4, §1.5)
- Estimate the degree of recirculation of plasma after it has left the ionosphere. (§1.5)

The task includes several first-time measurements such as the **systematic quantitative measurements of the entire exosphere** that leads to

#3: How are fundamental physics/chemistry processes affected by the space environment?

- How are isotopes fractionated in the space environment? (§1.4)
- What are the ionisation/neutralising efficiencies in the space environment? (§1.4)

What should be measured where?

The mandatory species to measure for both thermal and non-thermal escapes are H, He, N, O, N_2 and their single-charged ions, which are the most abundant in the magnetosphere and exosphere. Except for ionised atomic oxygen (O^+) and atomic hydrogen (H), the observational knowledge on the escaping flux or relevant background density is either missing or very poor, and we need a wide range of measurements.

We need to know the exospheric/ionospheric density for both ions and neutrals, simultaneously, to

obtain the net ionisation rate at different altitudes. In addition, we need densities of all atomic masses up to 50 in order to separate isotopes such as H and D, or ^{16}O, ^{17}O, and ^{18}O, or ^{14}N and ^{15}N. We examine several isotopes because some isotopes have the same atomic masses as molecules ($D=H_2$, $^{15}N=CH_3$, $^{18}O=H_2{}^{16}O$) and could be difficult to separate.

For the species mentioned above, we also need the altitude profile from about 500 km to at least 2000 km (exobase is most likely not located higher than this altitude) to have a good input for modelling the thermal escape. For He, N, and O, we also need to measure up to 3 R_E geocentric distance such that we can examine the relation between the plasmasphere and the exosphere/ionosphere. In addition, knowing the neutral temperature is essential for modelling the thermal escape flux.

For the non-thermal escape, cold and hot ions must be measured in the high-latitude region where the ion escape takes place, such as the low-altitude region of **Fig. 1.9**: **(a)** polar cap, **(b)** auroral region and **(c)** sub-auroral region. These regions expand during active periods when the escape flux increases, and therefore, the measurement must cover > 55° geomagnetic latitude, with an altitude range from at least 1000 km up to as high as possible.

To have the information needed to extrapolate the loss rate to the past Earth, we also need to measure the energy input to the ionosphere/exosphere as the most direct driver. The largest energisation of the ionosphere is associated with particle precipitation from space (both ions and electrons for both hot and energetic up to 100 keV) and resultant large-scale charge separation between electrons and ions (i.e., large-scale electric potential) that causes the ionospheric Joule heating. This energy input takes place in nearly the same region as the outflow, and therefore, the plasma observations must cover all directions. These precipitating particles are also important as the energy input to the exosphere, because their effects are seen in the thermospheric neutral distribution (Meier et al., 2015). The precipitation measurement also provides an estimate of the return flow.

Another form of the energy input to the ionosphere is through the electromagnetic waves. However, these measurements, as well as the particle precipitation measurements (including in the form of field-aligned current), give only local values. Therefore, we need a global monitor of the auroral and magnetospheric activities. Part of such monitoring can be done both from space by auroral, airglow and ENA imaging of tens of keV (Brandt et al, 1999; Wang et al., 2010) and by ground-based measurements such as the AE/Dst indices and EISCAT_3D mentioned in §1.1.

Studies from past satellites have revealed that the non-thermal escape is strongly related to the electric field along the geomagnetic field and low-frequency electromagnetic waves, and that different types of ion energisation result in different mass-filtering. Therefore, low frequency wave information will help in classifying the non-thermal escape in terms of its mass-filtering and its dependence on the external conditions. The measurements of photoelectrons and magnetic field will identify different magnetospheric regions.

Finally, the solar UV radiation and the solar wind are mandatory information but are always monitored by other (space weather) satellites and ground-based facilities.

General strategy of the observation: Combination of different types of measurement methods

Although the scientific tasks require a broad range of measurements, it is possible to cover these measurements with a well-equipped single spacecraft. The technical details are explained in §3 and §4. Here, only a general overview is given.

For the exospheric measurements, we combine both in-situ ion/neutral measurements for local values and UV line-of-sight measurements for global values. This is possible even with a single spacecraft by pointing the line-of-sight remote sensing region to include the spacecraft trajectory. It is also possible to make such "dual measurements" covering a wide altitude range within a single traversal by having a highly elliptic orbit.

There is, however, an upper limit to the apogee that is required from space debris regulation: the orbit must avoid the geosynchronous (GEO) orbit. Therefore, apogee will be about 6 R_E (33000 km altitude) and perigee around 500 km (this oscillates, as described in §4.1).

The measurements of the plasma environment additionally require coverage of the high-latitude region. Therefore, the orbit must have a high inclination (> 80° to cover the geomagnetic pole). Such a high-inclination and highly elliptic orbit can actually cover the entire magnetospheric region due to the drift of apogee in both longitudinal (RAAN drift) and latitudinal directions.

Finally, ESCAPE will take advantage of ground-based observations, particularly the 3-D volume measurements by the newly operating EISCAT_3D radar (cf. §1.1 and **Fig. 1.2**) during the traversals when the spacecraft is geomagnetically conjugate with the radar observation area. Since ESATRACK Kiruna station is located in the same as EISCAT_3D, orbit should be optimised to use Kiruna station for operation and downlink as much as possible.

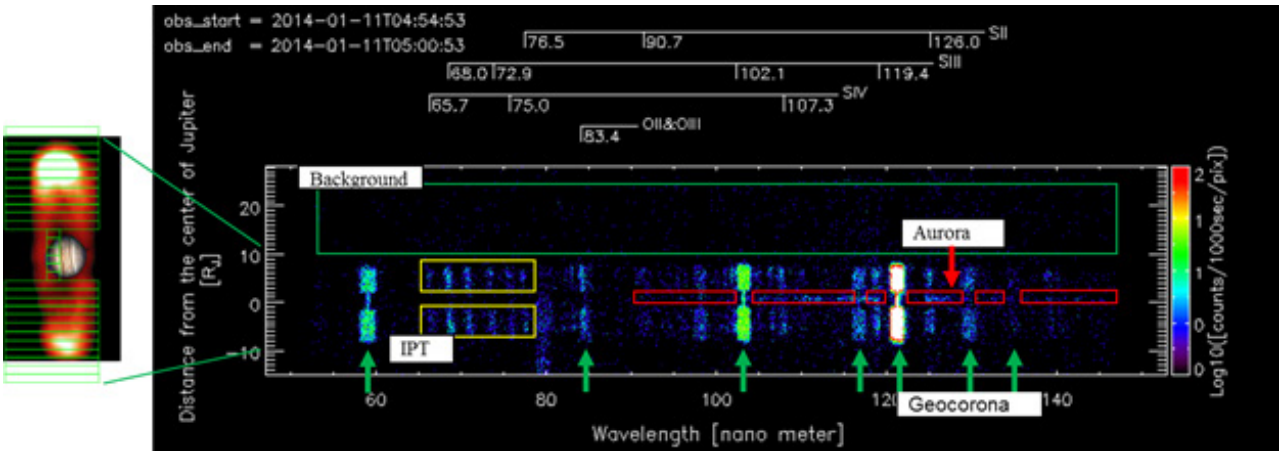

Fig. 1.11: An example (a 6 min cycle) of EUV (50-150 nm) observation of Jupiter by Hisaki (Yoshikawa et al., 2016, submitted to GRL) using an instrument with similar design as UVIS in this proposal. The emission from the exosphere (marked by green arrows) is stronger than the emission from the Io plasma torus (marked by yellow rectangles) and the Jovian aurora (marked by red rectangles).

1.7. Scientific spin-offs

The set of measurements summarized in §1.6 will also provide important knowledge in other fields.

Evolution of planetary atmospheres

One obvious spin-off is the relevance to the evolution of other planets, like Mars and Venus. By knowing the relative importance of the thermal and non-thermal escape, we will have better estimates of past escape for weakly magnetized planets such as the ancient Mars and Earth during the first 1.5 billion years (Sumita et al., 2001; Solomon et al., 2005), and even for the non-magnetised planets, for which the thermal (including photochemical) escape and exosphere play the central role. A comparison to the Mars (MAVEN) results will improve the knowledge of the effect of the geomagnetic field. Also the investigation of the isotope ratio improves the estimation of past atmospheric escape from planets, and improves the estimate of initial water inventory on Venus and Mars.

Correction of exospheric absorption in optical (astrophysical) observation

Knowledge of the exospheric distribution is also useful in astrophysical spectroscopic observations because the emission or absorption by the exospheric neutrals is one of the most significant sources of background light contaminations. For example, Hubble Space Telescope observations of hydrogen and oxygen lines of astrophysical and planetary objects are often severely affected by the geocorona emission lines. Japanese planetary telescope Hisaki selected the orbital altitude above 1000 km to minimize such a contamination from the lower exosphere (while the minimisation of the radiation belts background requires as low altitude as possible). Yet, the contamination from the exosphere is very strong as shown in **Fig. 1.11**. The model of the exosphere obtained from ESCAPE will provide a better correction scheme for astrophysical/planetary spectroscopy observation.

Ionospheric physics

The ESCAPE measurements include detailed composition and energy distribution of the ionosphere. The combination of EISCAT_3D with a volume 3D observation allows us to investigate the relation between the lower/upper ionospheric conditions, precipitating particle conditions, and ion/neutral dynamics at the spacecraft altitude: what kind of ionospheric conditions generate what kind of ion energisation and ion-neutral interaction, both with precipitating particles and without precipitating particles. Such observations can be as fine as the auroral arc thickness in the ionosphere because the spatial resolution of the EISCAT_3D will be much less than 10 km at > 500 km altitude, and that for ESCAPE is about 10-20 km (one looking direction in the 3 rpm spin is about 1.2-2.5 sec).

The altitude profile of the isotope ratio also gives a large-scale overview of the convection as mentioned in §1.4 (although need > 500 km total thickness to detect). Since the spacecraft covers a wide range of altitudes, we can also find the altitude of initial preheating of ions before the escape starts.

Exospheric effect on Ionosphere-Plasmasphere coupling

The plasmasphere has been considered a passive region that receives cold ions from the ionosphere. However, the high He^+ concentration is still a puzzle. It may be due to direct ionisation from the exosphere where the light neutrals (He) extend to much higher altitudes than O, N or N_2, particularly under the

influence of precipitating particles, electric field, and electromagnetic waves. There is also some speculation that there is a contribution from the solar wind He^{++} through the charge exchange. Another question is how much do the plasmaspheric ions return to the ionosphere. The new knowledge on the exosphere with direct observations of He and cold He^{+} and the ionisation/neutralisation efficiencies will give hints on these questions.

Magnetosphere-Ionosphere coupling

The spacecraft orbit covers various escape routes as well as the auroral acceleration region (cf. **Fig. 1.9**) with comprehensive plasma measurement (ions at all energy range and DC and AC magnetic field), and simultaneously monitors the ionospheric conditions with optical measurements (aurora and some ion density). Therefore, we should be able to determine the mass flow and energy flow (both directions between the ionosphere and the magnetosphere) and its dependence on ionospheric conditions or precipitating particles. In addition, extra species N^{+} and N_2^{+} that are separated from O^{+} will provide new information on magnetospheric dynamics. For example, it should allow time dependent tracing of the route during active periods when the N^{+}/O^{+} ratio changes (the time difference of the N^{+}/O^{+} ratio change between the inner magnetosphere and the ionosphere indicates the travel time, and hence the route because they should follow the similar trajectories).

---

2. Requirements for instrument specification

2.1. General goal on measurement quality

We first define the target accuracy. Since more than an order of magnitude differences in flux is expected between the dominant 3–4 mechanisms (e.g., Lammer et al., 2005a,b, 2008), we need to identify the types of dominant escape (up to 3) for different driver conditions and obtain the corresponding escaping fluxes in order to estimate the composition of total escape. Also, the past estimate of the escape flux varies by order of magnitude between different observations (Peterson et al., 2008; Lundin et al., 2013). Therefore an uncertainty of a **factor of 3** in estimating the flux is acceptable and adequate. With this accuracy, we can determine the resolution and sensitivity/dynamic range of each measurement that is proposed in §1.6, as described below.

2.2. Required resolution and dynamics range

Spatial, temporal, and energy resolutions

For thermal escape, the gravity determines the escape energy (escape energy is inverse proportional to geocentric distance as seen in **Table 1.3**), the temperature and energy created by photochemical reactions determines the fraction that exceeds the escape velocity, and the density determines the amount of escaping flux from each location. Therefore, the basic information that we need is the altitude profile of density and temperature.

Theoretically, the temperature of the "collision-free" exosphere is expected to be constant over different altitudes and the densities of major species are expected to decrease smoothly and exponentially with a constant scale height. Therefore, interpolation from 100 km altitude resolution data can provide the necessary accuracy (like **Fig. 1.5**) even though the density decreases over 100 km is by more than one order of magnitude for N_2 and nearly one order of magnitude for O as shown in **Figure 1.3**.

The requirement for the temporal resolution largely comes from this spatial resolution. The 100 km altitude resolution requirement in the ellipse orbit requires about 1 min resolution and < 0.1° slit resolution for remote sensing data (UV instrument) and < 25 sec integration time for in-situ measurements, as shown in **Fig. 2.1**. The latter sets the spin period to about 20 sec. The other requirements for the temporal resolution are not demanding. The shortest change of the exosphere observed so far is about 6 hours at Mars (Yamauchi et al., 2015), and hence, we can use one-orbit averaged value as the baseline if the spacecraft orbital period is less than half day. For the non-thermal escape, we are not examining the fine variation of the escape but the average response to the external conditions, and 5-minute resolution (solar wind OMNI database are given for 1 hour and 5 min resolutions) is sufficient.

The energy resolution for the ion measurements comes from mass-velocity relation (cf. **Table 1.1**). This relation can be classified into three main types: no dependence (electrostatic acceleration), proportional to mass, and proportional to the square root of mass. This means an energy difference of about 13% between N^{+} and O^{+} for the proportional case (when the velocities are the same), and about 7% for the square root proportional case. In the latter case, however, we often observe H^{+} simultaneously, and therefore, 13% energy stepping is still sufficient for the present purpose. A sparse resolution is acceptable for > 1 keV.

For electrons, we also consider detecting photoelectron at < 30 eV ranges such that we can map the geomagnetic connectivity (Frahm et al., 2006; Coates et al., 2008). The mapping information is useful in diagnosing the origin and destination of the ions that are simultaneously observed with electrons. If photoelectrons are to be classified in terms of chemical reactions, energy resolution of < 1 eV is required. However, if one just aims to obtain the total flux of photoelectrons, the same $\Delta E/E$ as ions is still fine.

While the required energy resolution is rather high compared to the past plasma missions, we do not require high angular resolution, because we study the amount of escaping and trapped flux, and do not plan to identify loss cone. We only need to classify 5 directions (parallel, oblique and perpendicular) with respect to the geomagnetic field.

Resolution of ground-based measurements (EISCAT_3D)

The spatial resolution of the EISCAT_3D volume observation of the ionospheric plasma conditions (density, temperature, velocity) is as low as 10 km at 500 km altitude. This is comparable to the spatial resolution of the spacecraft observations (10 km distance at perigee means about 1 sec flight time, which is about the observation cycle of ions and neutrals for a single direction and a limited energy range).

Dynamic ranges

The TIMED/GUVI observations indicate that the H density is around $10^{4\text{-}5}$/cc over 400-1000 km range (Qin and Waldrop, 2016) and the O density around $10^{6\text{-}7}$/cc at around 500 km with 30-40 km scale height (Meier et al., 2015). The ion density is lower than neutral density by 2-3 orders of magnitude (10^6/cc at ionospheric F region). Since our interest is the extension of the high-density region toward high altitudes, we target the upper limit 10^6/cc for neutrals and 10^3/cc for ions. If this is measured remotely as a column density, we multiply the peak density by the effective length of highest-density region (about 1000-10000 km), implying the column densities of major neutrals ranging $10^{9\text{-}13}$ cm^{-2}

The lower density limit (sensitivity) is determined from the isotope ratio because both the main isotopes and minor isotopes are to be measured. For O and D, the isotope ratios at the surface level is about 10^{-3} to 10^{-5} (cf. **Fig. 1.7**), and this is expected to decrease with altitude. Therefore, the density of minor isotopes at around 500-1000 km altitude will be 0.1–10/cc for D and 1–10^3/cc for neutral ^{17}O and ^{18}O.

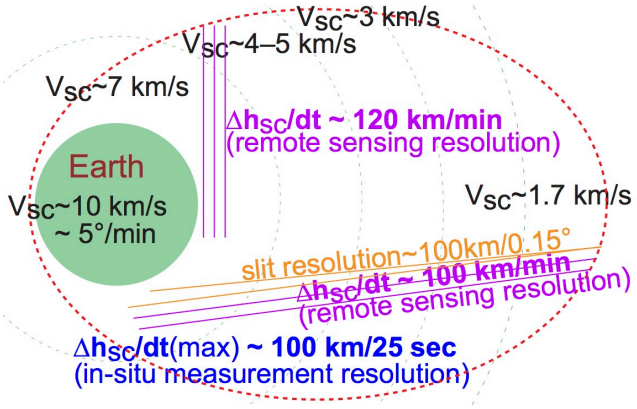

Fig. 2.1: Spatial resolution determined by the orbital motion for 32000 km x 500 km orbit.

Table 2.1: Required dynamic range for the planned measurements (with 1 minute resolution)

What to measure	Target range	Particle SI*	Other SI*
Density of major neutrals (H, N, O, N_2=CO, NO, O_2) and cold ions (H^+, He^+, N^+, O^+, N_2^+), simultaneously	neutrals 1–10^6/cc ions 0.1–10^3/cc	INMS, WCIMS	UVIS, SLP, ASPOC
Density of minor isotopes (D, ^{15}N, ^{17,18}O, D^+, $^{15}N^+$, $^{17,18}O^+$)	neutrals 10^{-2}–10^3/cc ions 10^{-4}–10^1/cc	INMS	SLP, ASPOC
Neutral temperature	500–1500 K	WCIMS	density+model
The energy distribution of major outflow ions (H^+, He^+, N^+, O^+, N_2^+)	$10^{5\text{-}9}$ keV cm^{-2} s^{-1} str^{-1} keV^{-1}	MIMS, NOIA	MAG, SLP
The flux of major returning energetic ions (H^+, He^+, O^+, N^+, N_2^+)	$10^{6\text{-}9}$ keV cm^{-2} s^{-1} str^{-1} keV^{-1}	EMS	MAG
The energy distribution of electron and photoelectron	$10^{7\text{-}11}$ keV cm^{-2} s^{-1} str^{-1} keV^{-1}	ESMIE	MAG
Ionospheric auroral condition	$10^{2\text{-}6}$ R		AMC, ground
DC/AC field energy flux into to the ionosphere	1–10^2 W/km^2		MAG, WAVES
Electromagnetic wave associated with ions	0.1–10^3 Hz		MAG, WAVES
ENA flux for charge-exchanged trapped keV ions	$10^{2\text{-}5}$ cm^{-2} s^{-1} str^{-1}	ENAI	

* The scientific instruments (SI) are described in **Table 3.1** and §3.

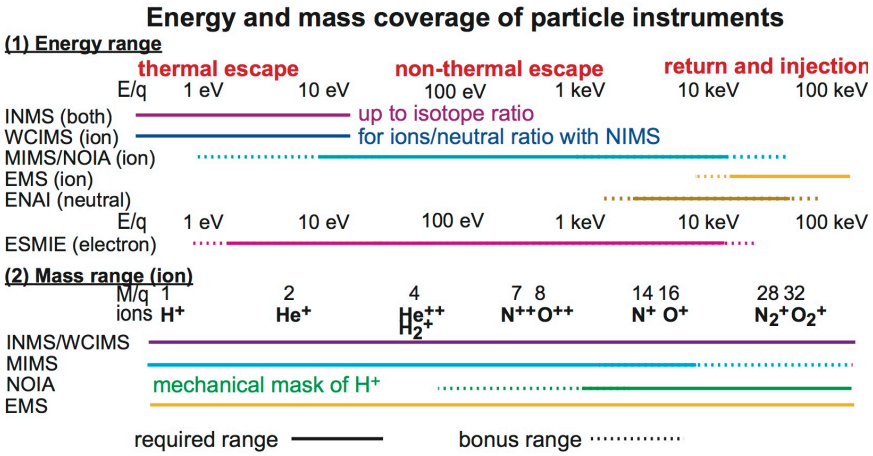

Fig. 2.2: Measurement targets for particle SIs. All SIs are for in-situ measurements except ENAI which is the line-of-sight integration measurements

We target the lowest measurable density as 0.01/cc for neutrals and 10^{-4}/cc for ions. For temperature, TIMED/GUVI observations and model predicts about 500-1500 K, and therefore, the ideal dynamic range is 400–2000 K with margin.

For the non-thermal escape, we must obtain the flux at different energies; i.e., we must measure the differential energy flux. From the past observations, we expect up to 10^{9} keV cm^{-2} s^{-1} str^{-1} keV^{-1} for the ion outflow and 10^{11} keV cm^{-2} s^{-1} str^{-1} keV^{-1} for the electron injection (cf. **Fig. 1.1**, DMSP, FAST, and Cluster observations). The recommended dynamic range is at least 10^{4} to include minor species for ions and photoelectrons for electrons, i.e., $10^{5\text{-}9}$ keV cm^{-2} s^{-1} str^{-1} keV^{-1} for ion and $10^{7\text{-}11}$ keV cm^{-2} s^{-1} str^{-1} keV^{-1} for electrons.

Summary of dynamic ranges and relevant instruments

The target dynamic ranges, including the other measurements, are summarised in **Table 2.1**. The actual values can be higher than the upper limits and can be saturated, but such cases are classified as extreme events, and what we need to know is its altitude extension because that determines the thermal escape rather than the density value of low altitudes. In the table, the information directly needed for estimating the escape flux is listed in blue, while the rest (black) is for background conditions.

Table 2.1 also lists the proposed scientific instruments (SI) and support payloads for each measurement target. The technical details of SIs are described in section §3. We need many types of particle instruments in order to cover different targets as shown in **Fig. 2.2**.

Here, WCINS will include a neutral sensor that allows measurements of velocity distribution and temperature of neutrals. In addition to these particle instruments, UVIS measures the line-of-sight integration of the EUV emission lines, SLP measures the spacecraft potential using Langmuir probes on long wire booms, ASPOC controls the spacecraft potential to < +5 V, MAG measures DC magnetic field, AMC takes the auroral images, and WAVES (package of search coil magnetometer (SCM) and wave analyser) measures low-frequency electromagnetic waves.

2.3. Conversion to the instrument sensitivity

The requirement of dynamic range is eased by changing the integration time up to about 1 min. The spin (~ 20 sec) resolution for in-situ measurements mentioned above is required only near the Earth where density is relatively high. For example, the required dynamic range for the in-situ neutral density measurement by INMS and WCIMS is eased to $10^{1\text{-}6}$ cm^{-3} every 5 sec, and the UVIS should be able to detect $10^{10\text{-}13}$ cm^{-2} for neutrals and $10^{8\text{-}10}$ cm^{-2} for ions every 5 sec. This requirement determines the target wavelength as *85–140 nm* (*103 nm/122 nm* for H, *95 nm/113 nm* for N, *99 nm* for O), and as optional at *83 nm* for O^{+}, *58 nm* for He, and *30 nm* for He^{+}.

For the energy distribution, MIMS and NOIA must cover a range of $10^{5\text{-}9}$ keV cm^{-2} s^{-1} str^{-1} keV^{-1}, for EMS $10^{6\text{-}9}$ keV cm^{-2} s^{-1} str^{-1} keV^{-1}, and for ESMIE $10^{6\text{-}11}$ keV cm^{-2} s^{-1} str^{-1} keV^{-1}. The required geometric (G-) factors are determined by these "one-count level" and the integration time. For example, an instrument with the G-factor of 5×10^{-4} cm^{2} str and integration time of 10 ms has the one-count level as 2×10^{5} keV cm^{-2} s^{-1} str^{-1} keV^{-1}.

In addition to the requirements for the particle instruments, we need to keep the spacecraft potential as low as possible to allow cold ion enter the instruments (INMS and WCIMS, both have acceptance energy range up to 20-30 eV) nearly as it is. This will be done by ASPOC that keeps the spacecraft potential within +5 V. Simultaneously, the spacecraft potential must be measured with an

accuracy of 1 V for correct density estimate, and such an accuracy also helps correct energy measurements for hot ions (within 10 eV) and photoelectrons. To measure the spacecraft potential with this accuracy, SLP must be outside the spacecraft sheath region when the density is high (in low-density regions, the ion energies are normally high, so that the spacecraft potential does not influence the flux estimation). Therefore, SLP must be placed at a distance of 15-20 m from the spacecraft.

The mass resolution requirement is tricky, because the minor component is sometimes hidden by the major component at a nearby mass. For example, just separating N and O in the ideal situation requires $M/\Delta M > 8$, but that gives only three possible classifications: N and O are about the same amount, N is negligible compared to O, and vice versa. If we need to differentiate the N/O ratio with a 10% accuracy, we need at least three more independent mass points between the two species, resulting in a requirement of $M/\Delta M > 30$. This is what is required for the cold ambient plasma and neutrals component. The mass separation between isotopes is the toughest one. With $M/\Delta M \sim 1100$, INMS can measure D with *S/N* ratio of about 10 in one min integration.

Separation of hot atomic ions and hot molecular ions of < 10 keV also needs another caution because time-of-flight (TOF) type instruments require detection of the passage of "start" surface/grid, through which (1) the molecular ions can be dissociated and (2) different species will loose different energy due to different chemical properties. The high flux of H^+ in the polar cap (originally coming from the solar wind) is another problem for all hot ion instruments because two counts within the integration time mess up the mass detection. To avoid these problems, the best method is to have two separate instruments (cf. **Fig. 2.2**), one with TOF concentrated on atomic ions (m/q=1-20) and the other without TOF (e.g., magnetic method) and mechanically masking H^+ and He^+, targeting heavy mass only (m/q=10-40). By overlapping m/q=10-20, these two instruments provide a smooth mass coverage. In other words, ESCAPE will abandon the traditional concept of "one instrument measures everything".

2.4. Avoiding operation in the radiation belts

The spacecraft orbit passes through the radiation belts, where MeV particles penetrate the containers of the payload, adding significant background noise to the measurements and degrading detectors such as the micro channel plate (MCP) detectors (Kistler et al., 2013; Yamauchi et al., 2013). Since non-thermal escape in this region is much smaller than thermal escape, the relevant instruments must be turned off to keep the sensors healthy. There are two radiation belt regions: the inner belt and the outer belt (e.g., Ganushkina et al., 2011). We will switch off most of the instruments in the inner belt, and switch off some instruments even in the outer belt (e.g., UVIS, AMC, INMS, WCIMS, NOIA).

In past missions (e.g., Cluster), such a sleep mode had been pre-programmed using the predicted location of the radiation belts. This approach is still useful for the inner radiation belt. However, the outer radiation belt is so dynamic that the high-flux region is often shifted from the predicted location (e.g., Reeves et al., 2016). Fortunately, the payload includes an energetic ion instrument (EMS) and the total count from that instrument can be used to flag the passage through the radiation belts. In order to provide this information to the relevant instruments, the spacecraft DPU will process a part of the EMS data package and send sleep commands to the instruments. This function of the DPU comprises a virtual instrument "radiation belt monitor".

2.5. Key differences from the past missions

Different approach for exosphere observations

Except for DE-1 (launch 1981) and some atmospheric satellites in the 1970's, past mission obtained density profiles of the thermosphere and exosphere only by remote sensing methods using line-of-sight integrated values of UV. These old in-situ measurements from 40 years ago are the basis for the present model that must be revised as described in §1.3, while reduction of local density from the line-of-sight integrated measurements strongly rely on the model (for example, the temperature of the exosphere is derived from the scale height with an assumption of nearly constant temperature). By combining in-situ measurements and remote-sensing measurements, we can construct density profiles without the assumptions that are inevitable for line-of-sight observations. In addition, ESCAPE is the first mission that will carry systematic isotope measurements in the exosphere.

Different approach for plasma missions

All past missions relevant to ion escape measurements around the Earth (e.g., Cluster) were focused on the mechanisms to energise ions, with emphasis on wave-particle interactions and auroral acceleration. ESCAPE takes a different approach, focusing on the consequences (flux) of such escape mechanisms by taking into account the chemical properties of the escaping species. In fact, Mars Express did not carry a magnetometer or wave instruments, but our knowledge on the ion escape flux under different internal, seasonal, and external conditions has significantly advanced. This is why

we do not aim for high temporal/angular resolution or wide frequency range of wave detection, which have been available on many modern plasma missions around the Earth.

2.6. Redundancy (in case one or more instruments do not work)

The strong package of particle measurements allows backup (with less resolution) solutions for the key values such as the density and ion fluxes. The density is measured by particle instruments, SLP and UVIS. The hot ions are measured by different instruments at different mass ranges but with some overlap. The energetic ion instrument has some energy overlap with the hot plasma instruments. Even if we miss some species, we still obtain important information from the remaining species. The ionospheric conditions are monitored both by AMC and the ground-based facilities. Even if the magnetometer fails, the spacecraft attitude and the photoelectron information give us some knowledge on the direction of the ion flow and region.

Table 3.1: Proposed payloads for the required and recommended measurements

In-situ	**target**	**parameter**	**Heritage / TRL**
INMS (*U.Bern*)	neutral isotopes (>0.1/cc) cold ion isotopes (>10^{-4}/cc)	density mass (M/ΔM~1100)	Rosetta (2004) TRL=7-8
WCIMS (*GSFC*)	neutral (total) major cold ions (>1/cc)	density, temperature	Exocube (2015) TRL=7
MIMS (*IRAP*)	major light ions (hot < 40 keV) ΔE/E<13%, > $5\cdot10^5$ keV cm^{-2} s^{-1} str^{-1} keV^{-1}	differential flux mass (M/ΔM≥15)	new TRL=5
NOIA (*IRF*)	major heavy ions only (hot < 30 keV) ΔE/E<13%, > $5\cdot10^5$ keV cm^{-2} s^{-1} str^{-1} keV^{-1}	differential flux atomic/molecular ions	MEX (2003) TRL≥6
EMS (*UNH*)	major energetic ions (20–200 keV/q) ΔE/E<30%, > $5\cdot10^5$ keV cm^{-2} s^{-1} str^{-1} keV^{-1}	differential flux mass (M/ΔM≥15)	Solar Orbiter TRL≥6
ESMIE (*MSSL*)	hot electrons (10 eV–10 keV), ΔE<2 eV for <30 eV, > 10^8 eV cm^{-2} s^{-1} str^{-1} eV^{-1}	differential flux	Solar Orbiter TRL≥6
SLP (*BIRA-IASB*)	2 V accuracy	SC potential plasma density	PICASSO TRL=4-5
MAG (*IWF*)	-5000 - +5000 nT, ΔB<5 nT, 10% accuracy in direction	magnetic field:	MMS (2015) TRL=8
WAVES (*ASCR/IAP & LPC2E*)	10 Hz – 10 KHz df/f < 10% for < 20 Hz	electromagnetic and electrostatic waves	Solar Orbiter TRL≥5
Remote	**target**	**parameter**	
UVIS (*U.Tokyo*)	91 nm (N^+), 108 nm (N^+), > 0.5 count s^{-1}R^{-1}	UV emission over light-of-sight	Hisaki (2013) TRL=6-7
ENAI (*IAPS*)	line-of-sight integrated ENA flux (2–200 keV)	differential flux	Bepi Colombo TRL>5
AMC (*TohokuU*)	630 nm, 670 nm, and 558 nm images > 0.1 count s^{-1}R^{-1}	Auroral emission over light-of-sight	IMAP (2012) TRL=7-8
Subsystem*			
DPU (*ESA/NKUA*)	data management and compression radiation belt boundaries and warning	Radiation belt boundaries	Several SC TRL=7-8
ASPOC (*ESA*)	keep SC potential < 3 V		Cluster (2000) TRL=8
booms (*ESA*)	SLP to be placed > 15m from SC MAG and WAVES to be placed ~5m from SC		Bepi Colombo TRL=7

* Subsystem hardware will be prepared by ESA, while technologies for ASPOC and 15-20 m wire booms are available at IWF (PI for MAG), and Royal Institute of Technology (KTH) together with IRF.

3. Proposed Scientific Instruments

Table 3.1 summarises the measurement target and the technological readiness level (TRL) of the proposed scientific instruments (SIs). The payload is classified into four categories: (1) in-situ particle measurements; (2) in-situ electric and magnetic field measurements; (3) line-of-sight integrated measurements; and (4) remote monitoring of the ionospheric conditions.

Nearly all SIs are basically the same design (or closely derived) as existing instruments from recent missions, or those following a recent flight model delivery, and therefore achieved the required TRL >5-6.. Furthermore, sensitivity, dynamic range, and resolution of most of the SIs have achieved the required level.

The table also contains the required subsystems in order to make reliable measurements, i.e., DPUs for data processing and for warning on the radiation belts passage, ASPOC for controlling the spacecraft potential that affects the detection of cold ions, and booms to make the field measurements accurate.

3.1. SIs for in-situ particle measurements

(i) Ion and Neutral Mass Spectrometer (INMS)

Instrument design principle: INMS is a time of flight (**TOF**) coincidence mass spectrometer with $M/\Delta M \approx 1100$ resolution over a mass range of M/q = 1-1000. The ambient ions entering within the field-of-view (**FOV**) are extracted into the acceleration region by a high-voltage, high-rate (10kHz) pulsed potential. Then each ion packet is shaped and accelerated inside the ion source by a series of acceleration electrodes towards the grid-less ion mirror (reflectron). After passing the first leg of a field-free drift path, ion packets are reflected by the reflectron (potentials up to 5 kV), which allows energy and spatial focusing (time domain focusing), and are then directed onto a fast **MCP** (micro-channel plate) detector. During their TOF the initial ion packet separates into several ion packets according to mass-per-charge. The ions are recorded on a detector, with 2 MCPs in the chevron configuration and an impedance-matched anode (Wurz and Gubler, 1994, 1996). The resulting charge pulse on the anode is registered by a fast analog-to-digit converter (ADC) system with 2 Gs/s sampling rate and 8 bit vertical resolution (Luna-Glob heritage). The sequence of charge pulses, the TOF spectrum, is converted into a mass spectrum in a straightforward manner.

Operation: TOF spectra are recorded continuously and accumulated typically for 5 sec. to achieve a dynamic range of at least 6 decades in an accumulated spectrum. Accumulation time can be set via command between 1 to 300 s to accommodate

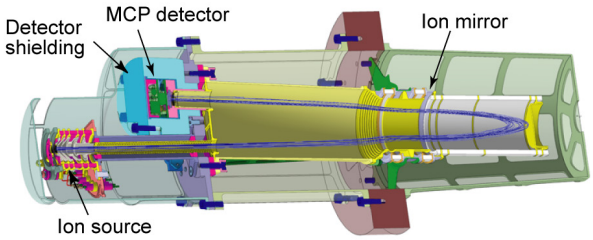

Fig. 3.1: Ion-optical design drawing of INMS sensor, with the ion source and the detector at the left side, and the ion mirror on the right.

different operation scenarios. For example, INMS can measure D with *S/N* of about 10 in 1 min. For ions, density of about 10^{-3} to 10^{3} cm^{-3} (six orders of magnitude) can be measured every 5 sec.

Heritage: INMS has heritage from Rosetta/RTOF (Scherer et al., 2006; Balsiger et al., 2007) and is significantly reduced in size already for JUICE/PEP, for which the prototype has been verified (Wurz et al., 2012). Radiation shielding is already fitted to high radiation environment of Jupiter.

(ii) Wide field of view Cold Ion Mass Spectrometer (WCIMS)

Instrument design principle: The WCIMS instrument will measure the mass composition of cold ions in the mass range 1-40 amu with mass resolution M/dM~50 adequate to resolve the ions H^+, He^+, N^+, O^+, OH^+, N_2^+, NO^+ and O_2^+ along the ecliptic trajectory of ESCAPE with primary focus at the exobase (Annex-C). In addition to mass spectroscopy the instrument will measure the temperature of the ion distribution in the range of 500K to 3000K and ion drifts, cross track and along the track in the range of ±3000m/sec. The instrument neutral side will measure the velocity distribution and hence the temperature.

The instrument design is based on a gated time of flight with pre-acceleration, and a reflectron for mass analysis as shown in **Fig. 3.2**. Cold ions enter the 360° ion aperture primarily from the ram direction and from an elevation angle in the range of ±22.5°, selected by the front ion steering optics. Thus the instrument continually measures the ion velocity distribution around the 360° azimuth direction while scanning the elevation direction in the ±22.5° range. In addition, a combination of circular **RPA** (retarding potential analyser) grids, located right inside the steering lenses, is used to scan the radial direction for the along-the-track ion velocity estimation. Ions at the exit of the RPA are radially pre-accelerated and focused through a circular electric gate structure, into a top hat electrostatic analyser (**ESA**), focused into a reflectron, and finally hit an annular MCP with

arrival times organized as $M/q = 2\ E/q * (TOF/L)^2$, where E is the total energy, and L is the TOF path from the first gate (start) to the MCP (stop). The ESA, biased at a fixed potential, filters out-of-band particles and UV light, whereas the reflectron increases the mass resolution due to energy spread. A gating electronic duty cycle control (~ 20% ±0.002%) allows optimum trade-offs of sensitivity and dynamic range. Time of flight is read out in 400 bins of 5 ns per bin and 2000 μs total range. Delay line position sensitive anodes with TOF ASIC / FPGA are used for 120 angles around the azimuth. One sec. accumulation of TOF spectra for ±10 elevation sectors and ±10 azimuth sectors (out of the 120 total) around the RAM direction are used to measure the mass spectrum, temperature and cross-track ion drifts (Paschalidis, 2002). Neutrals are measured with the same principle, except for the use of an annular thermionic ioniser, and the velocity distribution function will be measured in the cross track direction within 16 angular slices.

Operation: WCIMS has primarily two modes of operation: (a) Mass Species - Density - Temperature - Ion Cross Drifts; and (b) RPA mode. In mode (a) the instrument continually scans the ion velocity distribution in a FOV of ±22.5° x ±22.5° around the RAM direction with mass spectroscopy on; from those measurements the ion composition, temperature and cross drift velocities are extracted. (b) In this mode the RPA scans the RAM direction with the mass spectroscopy turned off (electric gate off); this mode gives the along-the-track ion drift – given knowledge of the spacecraft potential – and a redundant temperature measurement. The expected sampling time is 1 sec, with 0.7 sec allocated to mode (a) and 0.3 sec to mode (b).

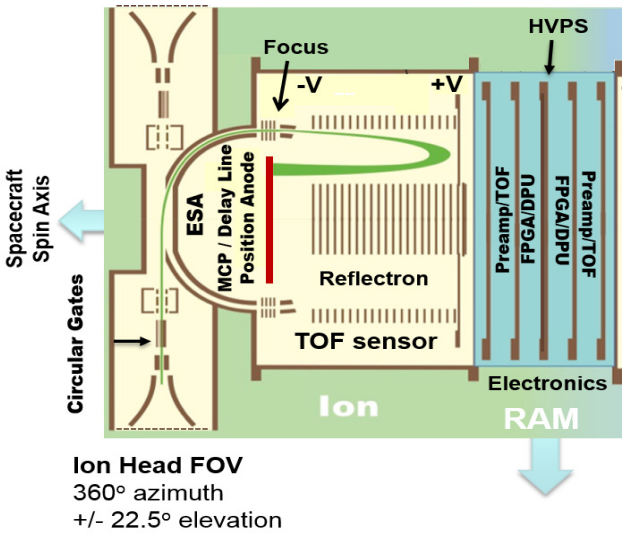

Fig. 3.2: Schematic view of the WCIMS with ion sensor and electronics. Particle trajectories are shown in green entering from ram direction.

Heritage: A miniature WCIMS without the reflectron has flown on two Cubesat missions: Exocube in 2015 and Dillinger in 2016 (Paschalidis et al., 2014).

Accommodation and Operation: WCIMS should be accommodated at one side of the cylindrical satellite. Also the 360° aperture of the instrument is expected to be elevated above the surface of the spacecraft. As the spacecraft rotates around its spin axis and moves around its orbit, the RAM direction of the flow is expected to always enter one of the sectors of the 360° azimuthal aperture of the instrument.

(iii) MCP Ion Mass Spectrometer (MIMS)

Instrument design principle: The MCP Ion Mass Spectrometer (MIMS) instrument on the ESCAPE spacecraft is a time-of-flight ion mass spectrometer, capable of obtaining full three-dimensional ion distributions (about 5 eV to 40 keV) within one spacecraft spin (~20 sec) and with a high-resolution mass-per-charge composition determination. Ions are selected as a function of their E/q (energy per charge) ratio, by sweeping the high voltage applied between the two hemispheres of a rotationally symmetric toroidal electrostatic analyser (360° x 5° instantaneous field of view). Then they go through a post-acceleration of ~5 kV and they subsequently enter into the TOF section, where the velocity of the incoming ions is measured, which allows the calculation of their m/q (mass per charge) ratio.

MIMS is internally divided into two sub-instruments, using the same electrostatic analyser, post-acceleration and TOF section, each one corresponding to a ~180° x 5° instantaneous FOV:

- One sub-instrument using a specially designed thin MCP as a conversion surface for the production the start TOF signal secondary electrons (**Fig. 3.3**). This technique takes advantage of the processes occurring during the scattering of the particles off a surface, i.e. kinetic electron emission. The energy loss of an incoming ion as it is scattered through a channel of this thin MCP is minimised, which minimises the uncertainty of the TOF signal, allowing a very good mass resolution ($M/\Delta M \geq 15$ (Annex-C)). This sub-instrument is based on the prototype developed and successfully tested at IRAP, Toulouse (Devoto et al. 2008; Cadu et al., 2012) and it is optimised for the study of low to medium energy (5 eV to 20 keV) ions.

- One sub-instrument using a thin carbon foil (1 μg/cm^2) for the production the start TOF signal secondary electrons. This sub-instrument is optimised for the study of medium to high energy (10 keV to 40 keV) ions, and it is based on the same

principle as the successful CODIF instrument onboard the Cluster spacecraft (Rème et al., 2001), but with thinner carbon foils for improved mass resolution ($M/\Delta M \geq 10$).

Subsequent detection of the ions (stop TOF signal) and of the secondary electrons (start TOF signal), for both sub-instruments, is performed by MCP detectors in chevron configuration. There are 7 x 22.5° discrete detection sectors for each sub-instrument, whereas the remaining two 22.5° sectors are "blind" and serve to provide a clear separation of the detection areas of the two sub-instruments, minimising any potential cross-talk between them. The two sub-instruments operate in parallel, and the 10–20 keV overlap in energy between them allows for a cross-calibration between the two sub-instruments. The front end electronics are based on custom developed low-power hybrid circuits (Devoto et al., 2004).

Accommodation: The MIMS instrument on the ESCAPE spacecraft has a 360° x 5° instantaneous FOV, and will be mounted on the spacecraft with its FOV tangential to the spacecraft cylindrical skin but just outside it, to have a clear view.

Operation: The MIMS instrument has a large amount of flexibility in the selection of the operational mode. These modes provide for the selection of different combinations of telemetry products and / or different energy /angular / mass / time resolution of the transmitted 3D distribution functions, allowing different schemes with respect to the above given typical instrument telemetry products description.

It is foreseen that during a typical orbit there will be at least two different modes used, one for operations close to perigee and one for the outer part of the orbit. In addition, during the passage through the inner radiation belt the instrument will be put in a safe mode (reduced high voltages).

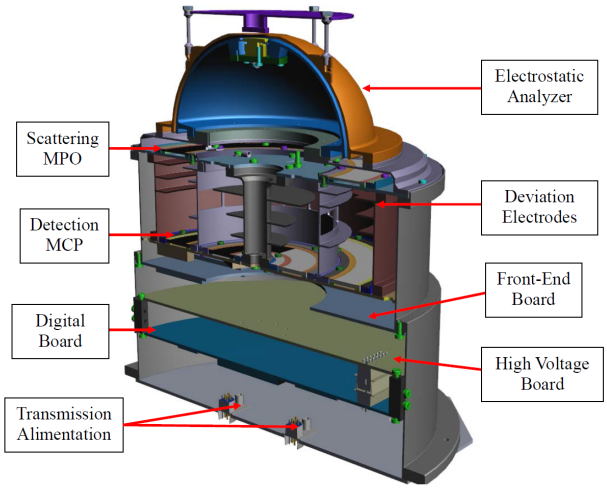

Fig. 3.3: Instrument system overview of the MIMS ion mass spectrometer: sub-instrument using a thin MCP as conversion surface for the production the "start" TOF signal.

Data handling: The MIMS instrument is controlled by FPGAs. It generates 3D distribution functions for typical ion species and detailed mass histograms (4096 TOF bins x 16 bits). These are then compressed, within the instrument digital board, to 64 ion species: The instrument provides data packets with compressed data. The MIMS electrostatic analyser performs 16 full energy sweeps per spacecraft spin (22.5° angular resolution in azimuth). For a ~20 sec spin period this corresponds to ~1250 ms per energy sweep, each sweep consisting of typically 200 energy micro-steps. There are five main categories of telemetry products, sent in parallel, with total telemetry rate: ~10 kbps.

Heritage: the MIMS sub-instrument with the thin MCP "start" conversion surface is based on the successfully tested prototype, developed at IRAP (Devoto et al. 2008; Cadu et al., 2012). The other sub-instrument, using a thin carbon foil for the "start" signal, is based on the CODIF instrument on board the Cluster spacecraft, part of the CIS experiment operating since 2000 (Rème et al., 2001). There are actually more than ~1000 papers published in refereed journals, based on the analysis of the data provided by this experiment (http://cluster.irap.omp.eu/public/publications/CIS_publications_list.htm).

(iv) Nitrogen-Oxygen Ion Analyser (NOIA)

Instrument design principle: The NOIA instrument has a traditional top-hat design (16 sectors over 360° entrance) using a magnetic mass separation system as shown in **Fig. 3.4**. Ions entering NOIA first pass a semi spherical electrostatic energy analyser, then a two-slit electrostatic lens, and finally the mass analyser using 16 radially oriented permanent magnets, where light ions (H^+, He^{++}, and He^+) are deflected completely away from the 100mm diameter MCP. The sampling time of each energy step is about 25 ms, covering 96 energy steps (from 10 eV to 10 kV or 1 eV to 1 keV) every 2.5 sec that correspond to 45° angles with 20 sec spin. After converting the electron shower from the MCPs to a raw count at each anode of the two-dimensional anode system (32 rings representing ion mass and 16 sector anodes, giving 640 kpbs), the data are processed to the required resolution (27 kbps), and after noise-reduction of isolated one-count events, compressed by a loss-less RICE compression method to about 6-8 kbps. In addition to data processing, the DPU also receives commands from the spacecraft, monitors voltages and temperatures, and sets the operation mode, including the energy table.

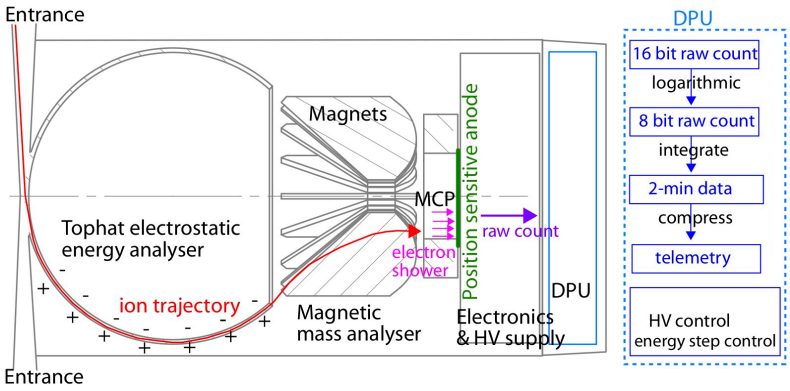

Fig. 3.4: Instrument design and flow of ion count generation and its processing by NOIA.

Accommodation: Top-hat FOV tangential to the spacecraft cylindrical skin but just outside it.

Operation: NOIA operation modes mainly concern different energy stepping, because the 6% energy resolution and an ideal stepping can cover only a factor of 96 over 250 steps. Therefore, different stepping schemes must be used, depending on the region. In-flight a cross calibration with MIMS will be needed.

Heritage: NOIA is as magnetic type mass-separating ion instrument, and is based on successful MEX/IMA (2003) and Rosetta/ICA (2004) that were built by IRF. MEX/IMA is still in operation and Rosetta/ICA worked until the end of the mission the 2 instruments without instrument degradation (Barabash et al., 2006; Fedorov et al., 2006; Nilsson et al., 2015). IMA and ICA are capable of separating molecular ions from atomic ions with a similar efficiency, because the entered ions do not rely on grid or surface interactions with this method, and they reached $M/\Delta M$=4 (Carlsson et al., 2006). They are designed for a 3-axis stabilised platform, which required an extra deflection system in the entrance to cover a third dimension, but this is not required for NOIA, simplifying the design. The other alternation is increasing the diameter of the electrostatic energy analyser to extend it to 145° instead of 127° for IMA, and to use 40% larger magnets than IMA's magnet. This maintains the right angle trajectory to the MCP and more than doubles the mass resolution (this will give $M/\Delta M \geq 8$ keeping the geometric factor according to 3-D ion tracing simulations of the instrument (Annex-C)) whereas the required ability is to separate N_2^+ and O^+.

(v) Energetic Mass Spectrometer (EMS)

Instrument design principle: The Energetic Mass Spectrometer (EMS) instrument combines an energy per charge selection with a time-of-flight and energy measurement to determine ion mass and mass-per-charge over the energy range 10 keV/e to 220 keV/e. The design is closely based on the Solar Orbiter Heavy Ion Sensor (HIS). A schematic of the sensor and dataflow is shown in **Fig. 3.5**. The entrance system is a half-toroidal section electrostatic analyser (ESA) that selects ions by energy per charge. The ion passes through the ESA, and then through a thin (~ 1 µg/cm^2) carbon foil. Electrons knocked off the carbon foil are steered to MCPs to give the start signal. A position sensitive anode below the MCP is used to determine the position information. The ion travels across a 9 cm flight path and hits the solid state detector (SSD). Electrons emitted from the SSD are steered to a second MCP that gives the stop signal. The time of flight is determined from the difference between start and stop. The combination of the time-of-flight and the energy per charge from the analyser gives the mass per charge of the ion. Combining the time-of-flight with the energy from the SSD allows the mass and charge state to be determined separately. The main design difference between HIS and EMS is that HIS also has post-acceleration, which allows lower energy ions to be measured. Because EMS is not required to measure below 10 keV, the post-acceleration is not needed, which greatly simplifies the design.

Accommodation: The EMS instrument on the ESCAPE spacecraft has a 160° x 4° instantaneous field of view (FOV). The instrument will be mounted with its FOV perpendicular to the spacecraft skin, with the 160° fan along the spin axis.

Operation: This EMS instrument is designed to be flexible. While the default mode has all species binned at the same energy angle and time resolution, different combinations are possible to optimise the telemetry for different regions. In addition, the energy stepping is controlled by a look-up table and so special stepping sequences (for example a fixed energy for high angular resolution) could also be selected.

Data handling: The EMS instrument is controlled by FPGAs. The HIS electrostatic analyser will be commanded to step through a defined stepping sequence 16 times per spacecraft spin (22.5° angular resolution in azimuth). In the default mode, each

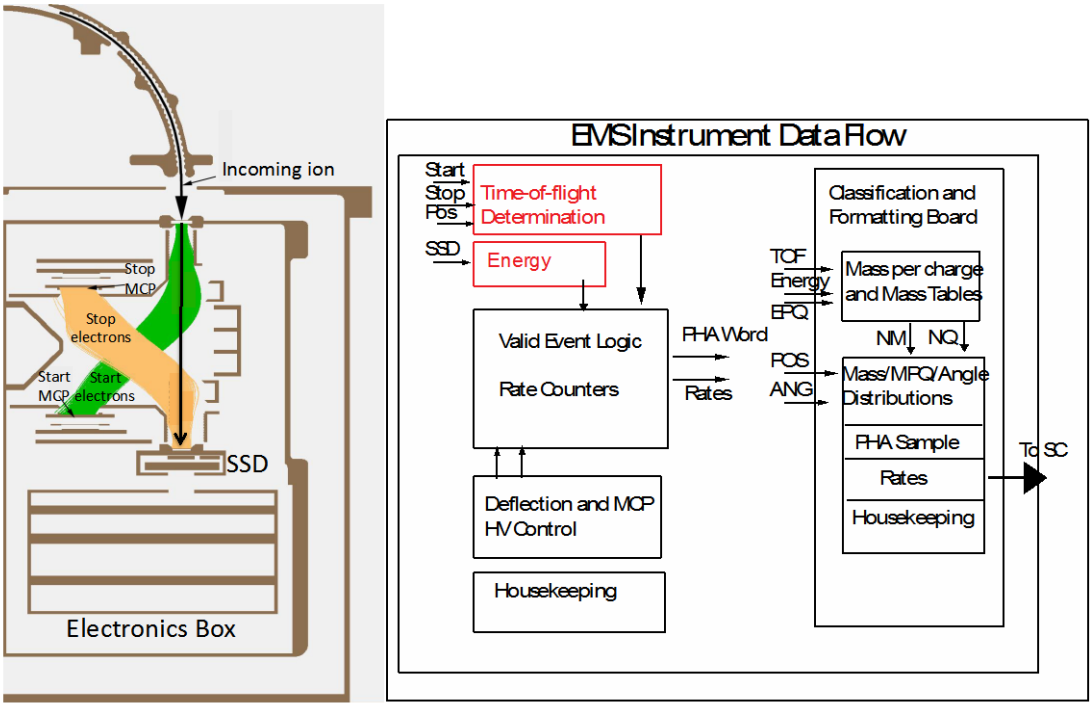

Fig. 3.5: The EMS instrument schematic and data flow.

sweep covers 12 energy steps. The stepping sequence will alternate between a high energy spin and a low energy spin, so that the full range is covered in two spins. The data will be summed over 6 spins to give 2 minute time resolution.

As illustrated in **Fig. 3.5**, the raw measurements for valid events will be combined to form pulse-height analysis (PHA) words that contain all the information (time-of-flight, energy, position, sweep step, and spin phase) for the event. The mass and mass per charge of each event will be determined from this information using lookup tables. The events will then be binned based on mass, mass per charge, angle and energy. This binned data as well as sample individual events will be used to form the science data products.

Heritage: The sensor configuration is based on the Solar Orbiter HIS (Livi et al., 2012). The time-of-flight section for HIS, as well as the MCP power supplies and anode boards were designed and built at the University of New Hampshire, while the electrostatic analyser was designed and built at IRAP. The principle of the instrument (combination of electrostatic analyser, time-of-flight and energy measurement) is the same as the STEREO/PLASTIC instrument, which was designed and built at the University of New Hampshire, led by Dr. A. Galvin. For ESCAPE, the instrument will be built predominantly at the University of New Hampshire based on the HIS optical design, using subsystem elements based on those designed for STEREO PLASTIC and HIS.

(vi) Electron Sensor for Magnetospheric and Ionospheric Electrons (ESMIE)

Instrument design principle: The ESMIE instruments will use the classic top-hat electrostatic analyser design (two separate top hat analysers attached to a single sensor electronic unit) in which electrons are energy-selected using a swept high voltage applied between a pair of hemispheric electrodes and angle selected using a pixelated anode. The second angular direction is sampled by performing multiple sweeps during the spacecraft spin and the spacecraft rotation will ensure that during every spin. This allows ESMIE looking along the magnetic field direction where the ionospheric photoelectrons (IP) are expected to be seen in the energy range 20 - 35 eV with an energy resolution of ~ 1 eV below 35 eV (while $\Delta E/E \sim 3\%$ in the energy range 10 eV to 60 eV). ESMIE also measures the magnetospheric electron population in the energy range ~10eV to ~10 keV with a coarser energy resolution of $\Delta E/E \sim 13\%$ up to 20 keV. There will be an option to float the energy range coverage relative to the spacecraft potential information from SLP.

Additionally, the collimator will be adjusted to reduce $\Delta E/E$; the corresponding reduction in geometric factor will be compensated by longer accumulation times to ensure adequate count rates. A more elegant approach that will be explored is to use a single larger top hat analyser with an electrostatically variable energy resolution, as an adaptation

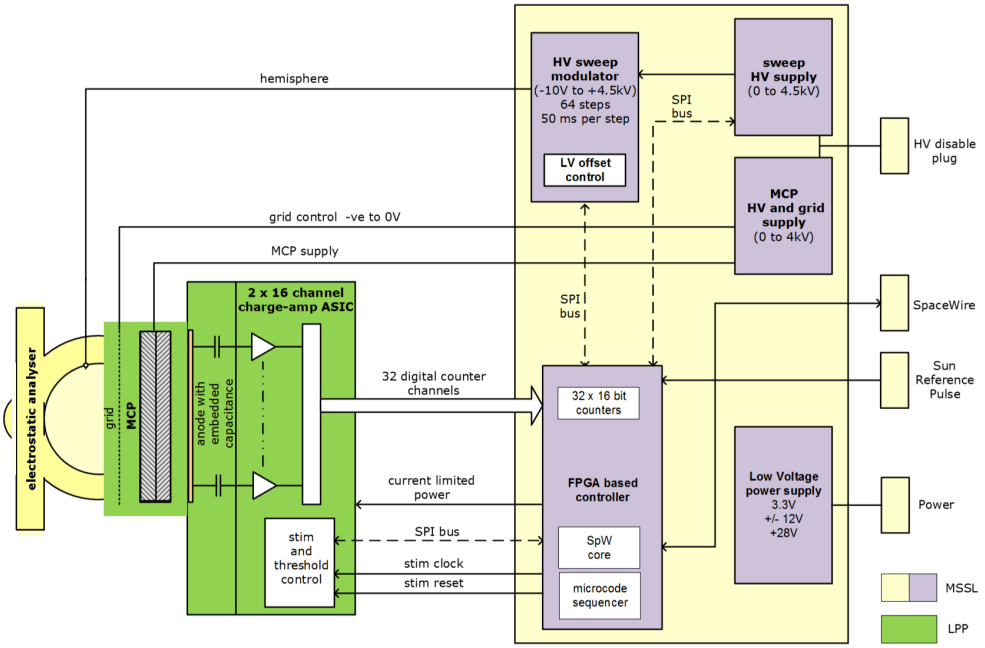

Fig. 3.6: Instrument design and flow of electron count generation and its processing of ESMIE

of the "variable geometric factor system" on Solar Orbiter SWA-EAS.

Operation and data handling: The operation of the instrument is controlled by an FPGA, synchronised to the spacecraft spin. Data will be collected during each spin, accumulated and compressed in the instrument to produce data at the required 2 min cadence, but the instrument can provide data at other cadences if required.

Heritage: The instrument will be closely based on the dual-analyser Solar Orbiter SWA-EAS, with the aperture deflection grids removed.

3.2. SIs for in-situ electric and magnetic field

(vii) Sweeping Langmuir Probe (SLP)

Instrument design principle: The Sweeping Langmuir Probe (SLP) instrument on the ESCAPE spacecraft uses classical spherical Langmuir probes mounted on booms. The main goals of the instrument are (1) to measure the spacecraft potential; (2) to measure the plasma density and electron temperature; and (3) to measure the low frequency electric field (DC to 2.5 KHz).

Measurement in Langmuir probe mode consists in setting the probes potential and measuring the collected current to establish the current-voltage relation (*I-V* curve), from which spacecraft potential, electron density and electron temperature are derived. Measurement in electric field mode is based on a differential measurement to infer the electric field from the floating potentials of both probes. The maximum measurement rates are 10 *I-V* curves / s and 5 KHz for the Langmuir probe mode and electric field mode, respectively.

Accommodation: The probes are mounted at the extremity of two 15-20 m long wire booms positioned opposite to each other with respect to the spin axis. This allows the probes to be outside the spacecraft sheath in most of the high-density environments (where the non-thermal escape is important) and leads to an adequate spacing between the probes (> 30m) to infer the electric field with sufficient accuracy (0.3mV/m).

Operating modes: The SLP instrument performs 10 sweeps per second, with each sweep covering 200 points. Basic modes are (a) Langmuir probe mode with transmitting the full *I-V* curve every time, (b) Langmuir probe mode with transmission of one full *I-V* curve plus a number of on-board derived potentials, densities, and temperatures at higher time resolution, (c) electric field mode, and (d) instrument housekeeping mode.

Heritage: The SLP instrument heritage is from the PICASSO SLP cylindrical probe instrument. The TRL is 4-5 presently, but will increase rapidly with the implementation of ESA's PICASSO in orbit demonstrator.

(viii) Magnetometer (MAG)

Instrument design principle: The DC magnetometer is a dual-sensor fluxgate magnetometer for measuring the ambient magnetic field. The design of the magnetometer consists of two triaxial sensors and the related magnetometer electronics, digital processing unit, power supply, and electronics box.

Each sensor consists of two entwined ring-cores to measure the magnetic field in three directions and is housed in an 8 x 8 x 5 cm package. One sensor is placed at the end of a solid boom and the second at

an intermediate distance along the boom to enable reliable subtraction of any residual spacecraft magnetic field. The magnetometer electronics are based on the MMS/FIELDS suite and employ the same Magnetometer Front-end ASIC (MFA-3). This provides major improvements in miniaturisation, mass and power, and provides 300 krad TID radiation hardness. The core of the electronics is the MFA-3, a third-generation magnetometer front-end ASIC developed at IWF. The digital processing unit of MAG will be based on the design of the Bepi Colombo MPO magnetometer.

TRL level: The fluxgate type is a matured instrument and has a high TRL(8). IWF led the fluxgate magnetometer for Venus Express and is leading the digital fluxgate magnetometer (DFG) on board MMS launched in March 2015.

Noise level and EMC requirement: The DC magnetometer will return magnetic field vectors (low range of ±500 nT to high-range of ±8000 nT) with > 20 bits digital resolution and with a noise floor less than 0.006 nT/√(Hz) at 1 Hz. An appropriate magnetic cleanliness plan such as implemented on previous space missions is required for the magnetometer measurements.

(ix) Waves signal processing (WAVES) with Search Coil Magnetometer (SCM)

Instrument design principle: The WAVES instruments processes the electric signal from SLP and the magnetic signal from the search coil magnetometer (SCM) in the frequency range up to 20 kHz.

SCM is a magnetic sensor of inductive type (**Fig. 3.7**). This is the sensor intended to measure the three components of the magnetic field from near DC (5 Hz) to about 20 KHz. It is composed of 3 ELF-VLF magnetic antennas (search coils) made of a ferrite core with a primary coil of 16000 turns. A secondary coil is used as a flux feedback, to create a flat frequency response on a bandwidth centred on the resonance frequency of the main coil. This active part is potted inside an epoxy tube (104 mm long, external diameter 20 mm). The magnetic antennas are assembled orthogonally in the most compact way possible by the body of the sensor. This mechanical support is made in a nonmagnetic material (PEEK KETRON) and stands for the interface with the satellite. The amplification electronic circuit is made using 3D technology. The 3D module will be boarded in the sensor's foot (close to the antennas) to reduce the signal-to-noise ratio. The sensitivity of SCM is 2.10^{-3} nT/(Hz)$^{1/2}$ at 10 Hz and 8.10^{-6} nT/(Hz)$^{1/2}$ at 2 kHz.

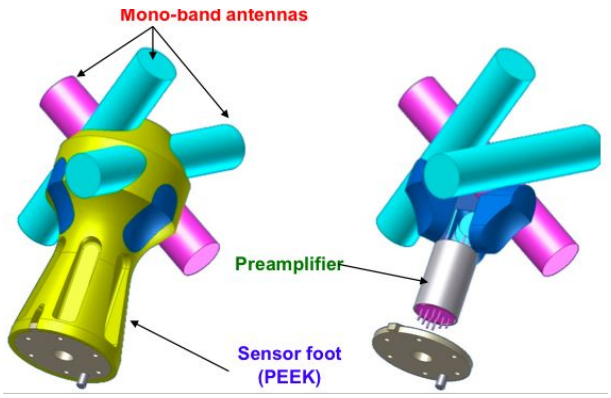

Fig. 3.7: SCM design (photo is found in Annex-C)

WAVES is composed of a wave analyser board (LFR) responsible for digitisation and processing of signals from SLP and SCM in the frequency range up to 20 kHz, a Digital Processing Unit (DPU), a power converter, and an electronic box. The data digitised by LFR are processed by integrated digital logic implemented in an FPGA, performing filtering, decimation and spectral analysis of the signals. This on-board pre-processed digital data from WAVES and SLP units are transmitted to the DPU for formatting and compressing before being transmitting to the spacecraft. DPU software will also perform numerical calculations such as producing the wave properties from the complex spectral matrices.

Heritage: IAP has significant heritage in the development of wave analysers for recent missions (Solar Orbiter, TARANIS, JUICE etc.). IAP will be responsible for the delivery of two complete LFR boards (all required models), including FPGA firmware and Ground Support Equipment. IAP has also a strong heritage in the DPU hardware.

Data products: WAVES is capable of producing four different products: (1) The magnetic waveform at a 122 Hz cadence. (2) The magnetic spectral matrices that are also produced continuously at an 1sec resolution with 200 bins in frequency. The bin widths are distributed following a logarithmic scale. (3) The full 2 sec waveform snapshot of 4 components (including one electric field component from the Langmuir probe), one snapshot per minute, to study the electrostatic emissions, and generally, the electric component of the emissions. (4) With only one electric component, it is still possible to get the Poynting flux orientation. Total of all products occupies 140 kbps after compression with 20 bit/data. Since the mission requires much lower resolution data, WAVES will actually produce only 10-20 kbps after compression.

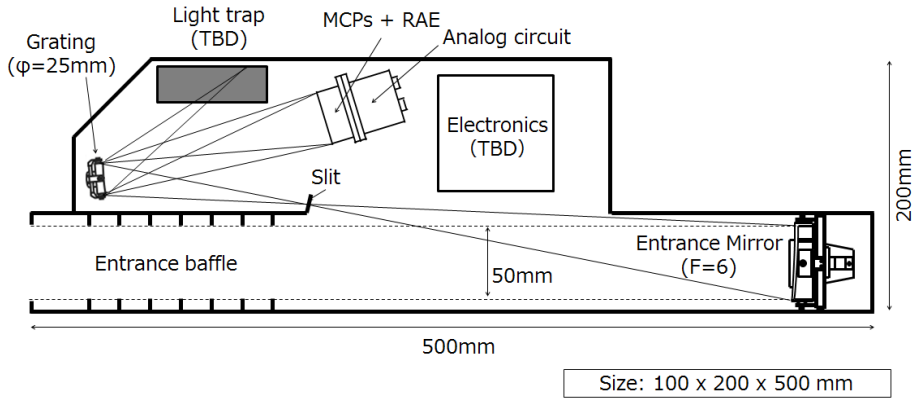

Fig. 3.8: Optical concept of the UVIS.

3.3. SIs for of line-of-sight integrated measurements

(x) Ultraviolet Imaging Spectrometer (UVIS)

Instrument design principle: **UVIS** (Ultraviolet Imaging Spectrometer) is a EUV imaging spectro meter with a spectral range 85 nm -140 nm (nitrogen and oxygen) and with three additional channels for O^+ (83 nm), He (58 nm), and He^+ (30 nm). UVIS uses an holographic diffraction grating. The optical scheme is shown in **Fig. 3.8**. The field of view is defined by a slit (2° x 0.1°) placed between the primary mirror and the grating. The intensified detector is placed at the focal plane of the diffraction grating. Photon detection is obtained by combining MCP based intensifiers with a CsI photocathode. The read-out is made by a cross-delay anode with one axis for the spectral dimension and the second axis for spatial imaging along the long dimension of the slit.

Operation: All operations consist of successive acquisitions of detector images made at different positions of the orbit. The acquisition time varies between 0.1 sec up to 100 sec depending on the line brightness. Calibration will be monitored by looking at bright calibration stars on a weekly basis during the mission. These calibrations do not require special manoeuvres.

Accommodation: UVIS will be placed on the despun platform articulated mounting (cf. §4.2.2). This allows orienting the 2° FOV in the limb direction and to perform scans so as to obtain the best altitude resolution with the 0.1° slit.

Special request: In the integration and pre-launch phase, the UV detector will be pumped at all times. For special periods, like vibration tests, the detector pumping can be stopped. Each period without pumping should be limited to two days.

Heritage: UVIS is the same design as on previous UV experiments on board Hisaki (**Fig. 1.9**; Yoshikawa et al., 2014; Yoshioka et al., 2014) and on PHEBUS-Bepi Colombo.

(xi) Energetic Neutral Atoms Imager (ENAI)

Instrument design principle: ENAI detects and images ENAs (energetic neutral atoms) at a 2–200 keV range with mass separation capability (H, He and O) by the TOF system at triple coincidence principle. As shown in **Fig. 3.9**, its FOV of 90° x 10° is further divided by the 5 plates of the entrance collimator and detection is by 6° x 6° anode pixels. The collimator acts as a background suppressor for charged particles (HV deflector) and photons (UV filter), as in the ELENA instrument on-board Bepi Colombo (Orsini et al., 2010).

At the ENAI entrance (1 x 2 cm^2) a thin Carbon Foil (CF) allows to identify the ENA passage and the START signal by the extracted secondary electrons. These are accelerated and collected by an MCP detector (START-MCP). The particles, passing through the entrance CF, follow their straight line in the TOF chamber. The primary Stop detector, composed of SSD at the end of the path, registers the energy of the particle above a mass-dependent threshold energy E_T. The SSD signal provides a STOP event characterised in energy and position (1D array). The second Stop detector is an MCP collecting again secondary electrons coming from a CF placed in front of SSD. The energy threshold in this case is lower than the previous one. This second STOP event allows to measure particles of lower energy and to have a triple coincidence in TOF measurement in an instantaneous 1D array.

The proximity electronics are based on custom developed circuits. High Voltage Power Supply (HVPS) supplies polarisation voltages to the instrument grids, the deflector plates and the MCPs.

Accommodation: The ENAI FOV central axis will be perpendicular to the ESCAPE spin axis, so that in a spin a full 90° x 360° image will be obtained.

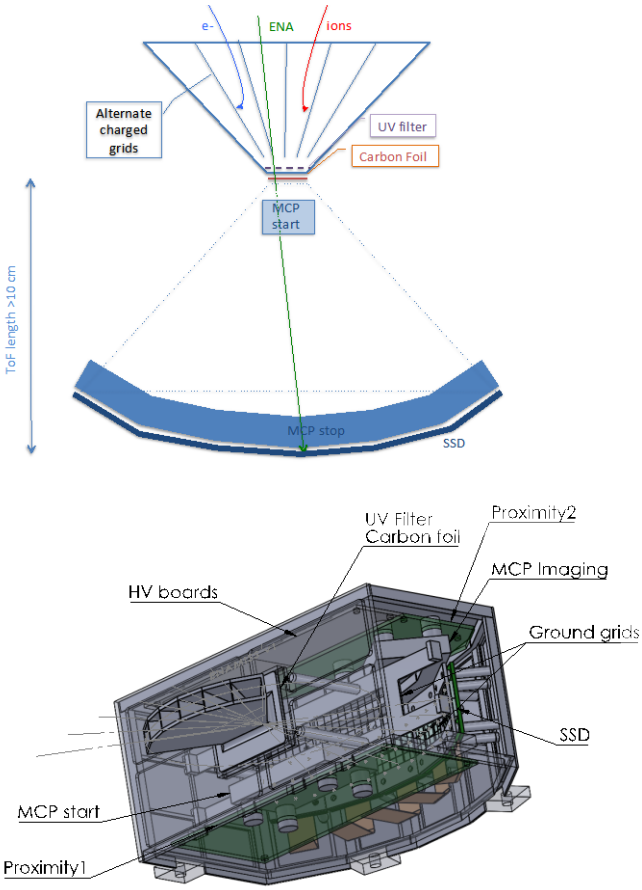

Fig. 3.9: ENAI concept (top) and 3D internal box (bottom)

Data handling: The ENAI instrument is controlled by FPGAs. It collects the particle transit time information and processes the combination of the coincidences from the different sources of event ID signal, and accumulates those events in a dedicated memory. However, FPGAs operate also an event-by-event mode to dump in real time the raw stream of the events. The event stream packs the following five basic informations: Energy, START-STOP$_{SSD}$ time interval, position P$_{SDD}$, START-STOP$_{MCP}$ time interval and position P$_{MCP}$. The telemetry products have several different modes.

Operation: The ENAI instrument has flexibility in the selection of the operational mode. These modes provide for the selection of different energy/angular/mass-TOF/time resolutions of the transmitted images.

Heritage: The ENAI instrument is based mostly on the TWINS designs (McComas et al., 2009), and the collimator and electronic boards (proximities and HVPS) take profit of the heritage of the Bepi Colombo/SERENA-ELENA sensor (Orsini et al., 2010).

3.4. Remote monitor of the ionospheric conditions

(xii) Aurora and Airglow Monitoring Camera (AMC)

Instrument design principle: AMC has two CCD cameras. Each one consists of an interference filter, objective lens, and CCD detector that is connected with a thermal path to a radiator (**Fig. 3.10**). The interference filters have centre wavelengths that are optimised for measuring the auroral O band at 630 nm (from high altitude, representing low-energy precipitation) and N_2 first positive band at 670 nm (from low altitude, representing high-energy precipitation), respectively. The objective lenses have a 10° FOV covering, e.g., a square area of 400 km measured from 2400 km altitude, for the auroral altitudes. The CCD detector, using fused silica for blocking radiation, has an efficiency better than 0.7 when it is cooled to -10°C to -30C° to reduce thermal noise. Cooling is achieved by a Peltier cooling thermal path connected to the radiator.

Accommodation: AMC, like UVIS, will be placed on the despun platform articulated mounting (cf. §4.2.2). to be able to point to the winter ionosphere from apogee, for auroral oval or airglow observations.

Data production: The CCD pixels of 1024 x 1024 are divided into an 8 x 8 binning (for aurora) or 16 x 16-pixel binning (for airglow), because the mission does not require high spatial resolution. The exposure time is a few seconds for faint airglow emissions. The estimated data rate will be 10 – 40 kbps.

Heritage: AMC is based on the multi-spectral auroral camera (MAC) on the Reimei satellite (Sakanoi et al., 2003) and IMAP/VISI on the international space station (Sakanoi et al., 2011). In these past missions the CCD detectors have been relatively resistant to radiation, although a commercial-based front-illuminated interline type has been used. CCD

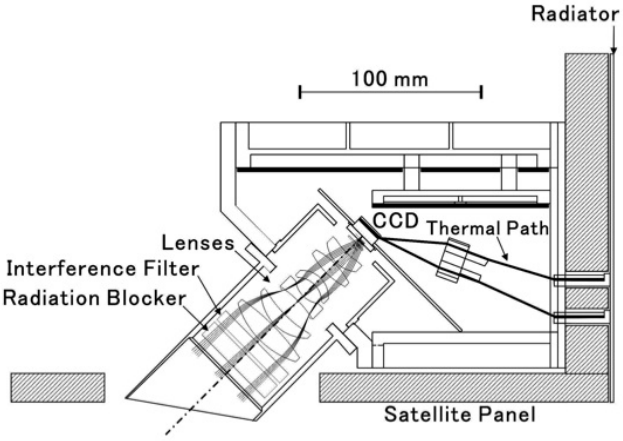

Fig. 3.10: Schematic of AMC and its accommodation.

can be replaced with a space-qualified on request. The objective lens and cooling unit are custom made to obtain sufficient performance in space.

3.5. Mandatory subsystem (needed to understand data from core instruments)

(xiii) Active spacecraft potential control: (ASPOC)

By emitting indium ions with energies 4–10 keV, to compensate for the photoelectron emission, ASPOC reduces the positive spacecraft potential to less than 5 V when the spacecraft surface is conductive (activated when more than 1 V), allowing for much more accurate plasma measurements at energies less than 50 eV (Riedler, et al., 1997). For this reason, ASPOC should be located on the shadow side of the SC. ASPOC contains a pair of ion emitter units, each connected to a dedicated high voltage supply. The number of emitters (four for the Cluster case) is determined based on lifetime and redundancy reasons (MMS emitters have lifetimes of > 9000 hours, i.e., 1 full year). Since ASPOC was successfully used on Cluster, TRL level is 8.

IWF (Graz) has extensive know-how on ASPOC. However, since this is a facility instrument not performing scientific measurements, we consider it as an ESA supplied hardware, like the spacecraft subsystems (cf. §5.2.).

Spacecraft DPUs and a "virtual instrument"

Table 3.2 gives the expected payload data production rates. For data processing and compression, we have 2 DPUs, one on the main spacecraft body (DPU-1) and one on the despun platform (DPU-2). The hardware should be provided by ESA, while the SI teams (NKUA) will take care of the software for compression and data handling.

In addition, the DPU processes high-energy particle data from EMS (and MIMS for redundancy) on a real-time basis to estimate the radiation belt presence, as mentioned in §2.4. This "virtual" instrument will need information of (1) total counts of energetic particles a in a representative energy channel of EMS, (2) double coincidence rates between start and stops signals of MIMS. From this information, the virtual instrument program issues alerts of different levels within the spacecraft DPU, adding extra commands for "sleep" to relevant SIs. Radiation belts boundaries identification is a derived scientific product.

Table 3.2: SI data production rate.

Instrument **for DPU-1**	Normal Data Rate kbps	Peak Data Rate kbps
INMS	2	34
WCIMS	4	16
MIMS	10	30
NOIA	8	40
EMS	4	16
ESMIE	5	20
SLP *1	30	120
MAG *1	2	8
WAVES *1	30	140
ENAI	20	60
Instrument **for DPU-2**	Normal Data Rate kbps	Peak Data Rate kbps
UVIS	10	40
AMC	10	40
Total	135 kbps	546 kbps

*1: These instruments have their own DPU and it is possible, as an option, to directly interface them with the spacecraft OBDH.

4. Mission Configuration and Profile

4.1. Orbit design

4.1.1. Requirements for the orbit

To fulfil the measurement requirement as described in §1.6, §2.2 and Fig. 1.9, the spacecraft must meet the following conditions:

- The spacecraft (SC) must slowly cover the polar cap magnetospheric region where the escaping flux maximises three dimensionally at different altitudes (1000 – 30 000km), latitudes and longitudes, within 3 years.
- The SC should traverse a wide altitude range of the lower exosphere, i.e. 500 to 3000 km altitude, such that the in-situ density measurements can give a snapshot of its vertical structure and composition.
- The SC should traverse the ring current region in the equatorial inner magnetosphere to measure the ions injected back from the magnetotail.
- Since we can avoid observations contamination from penetrating particles in the inner radiation belt by putting the instruments off or in an appropriate mode, the orbit may traverse the radiation belts.
- The 3-year radiation dose shall not require a higher level of shielding than 5 mm to reach <50 krad on EEE level.
- Orbital parameters must be designed to require as few manoeuvres as possible (e.g., free drift).
- The SC must not enter the geostationary ring during the operational phase; i.e., considering the latitudinal drift of the orbit parameter, apogee should be placed < 35 000 km altitude.
- The line-of-sight observation from the SC must cover the exosphere of 500-2000 km at different altitudes and solar zenith angles (longitude).
- The orbit should provide long periods for magnetically conjugate observations with the EISCAT-3D covered area.
- At mission completion SC can be de-orbited.

The best solution is a **highly elliptic polar orbit with perigee close to the exobase and apogee at ~33 000 km altitude** (cf. **Fig. 4.1**).

4.1.2. Proposed orbit

Within the above requirements, and following a series of different test runs we performed, the following orbit parameters turned out to be close to optimal:
- Perigee: ~500 to 800 km altitude; 800 km initial perigee altitude
- Apogee: ~33 000 km altitude (6.2 R_E geocentric distance)
- Orbital plane inclination: 90°
- Initial latitude of the line of apsides: 85° N

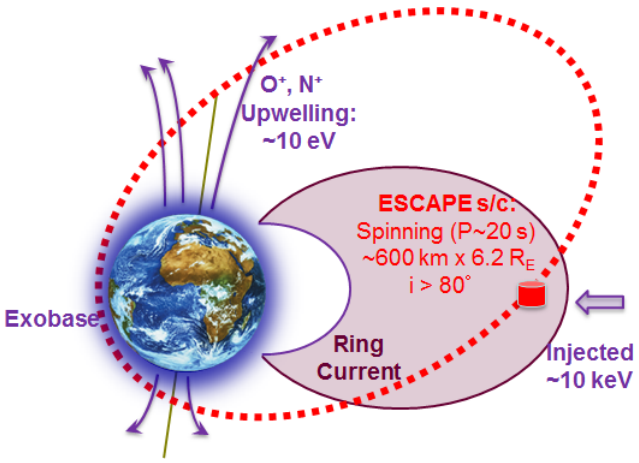

Fig. 4.1: Schematic representation of the ESCAPE orbit with respect to the mission target zones.

It results that the proposed orbit has then a 9 hours and 45 minutes orbital period.

The natural erosion of the above orbit, due to atmospheric drag and gravitational perturbations, was examined with the use of the STELA (Semi-analytic Tool for End of Life Analysis) CNES software. The dimensions of the satellite (cf. §4.2.2) were considered, giving a 0.00744 m^2/kg surface-to-mass ratio, and the simulations show that the **perigee altitude will fluctuate between 800 and 480 km** (cf. **Fig. 4.2**, left panel), depending on the initial altitude and argument of perigee.

This natural perigee altitude evolution provides the extra bonus of surveying the lower exosphere at different altitudes, down to just below the exobase, during the 3-year nominal mission and without needing the execution of any manoeuvres. In order to avoid the denser thermosphere as much as possible, the initial perigee altitude is chosen at 800 km (cf. **Fig. 4.2**).

The longer term simulation of the perigee altitude evolution, i.e. over 100 years, shows that the ESCAPE orbit perigee oscillates but never goes below 450 km (cf. Fig. 4.2, right panel), which implies that the natural orbit evolution will not lead to an atmospheric re-entry in the foreseeable future. A **de-orbiting manoeuvre** is thus necessary at the end of mission, to insure the atmospheric re-entry, and two options are available:

- Either a ΔV~20 m/s manoeuvre, to reduce the perigee altitude at 395 km, which would then expose the satellite to increased atmospheric drag and lead to a natural re-entry within 25 years;
- or a ΔV~87 m/s manoeuvre, that would immediately reduce the perigee altitude to 0 km (controlled re-entry). The hydrazine monopropellant mass necessary to execute such a manoeuvre is 23 kg (cf. §4.2.3).

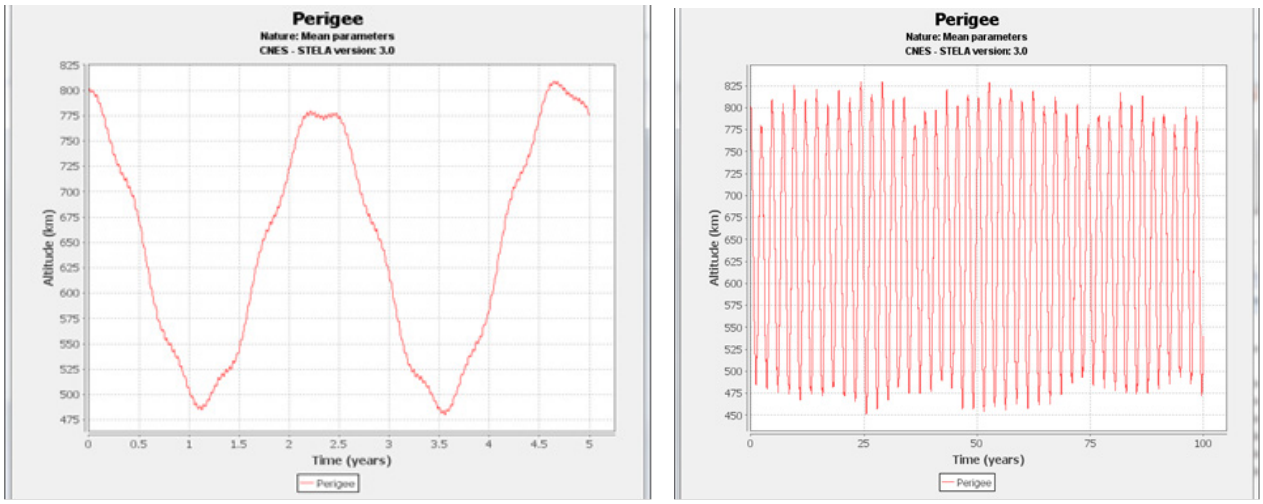

Fig. 4.2: ESCAPE orbit natural evolution of the perigee altitude, on the short term (left panel), and over 100 years (right panel).

The proposed orbit, with **90° inclination**, is almost inertial and the orbital plane maintains a fixed orientation in space along the year. The apogee thus, during the year, is successively in the magnetotail, dusk-side inner magnetosphere, noon-side inner magnetosphere / cusp and dawn-side inner magnetosphere, allowing a complete survey of the escape routes and ion circulation.

Due to gravitational interactions (mainly *J2*) the line of apsides is subject to a rotation of -0.21°/ day within the orbital plane, which leads to a natural southward drift of the apogee latitude. This **line of apsides rotation is thus 76.6°/year** (cf. **Fig. 4.3**).

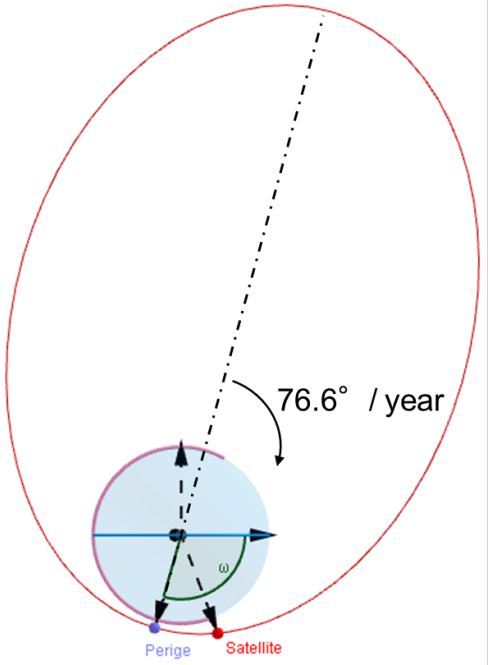

Fig. 4.3: Initial ESCAPE orbit (red) and 1000 km altitude projection (magenta). The rotation of the line of apsides, within the orbital plane, is indicated.

An initial latitude of 85° N of the line of apsides is adopted as optimal, allowing an early survey of the northern polar cap ion escape route. The subsequent rotation of the line of apsides allows then a detailed coverage of the ring current region in the equatorial inner magnetosphere, to measure the ions injected back from the magnetotail, and then the southern polar cap escape route. Note, however, that even a single orbit can pass successively through the polar cap and the ring current (cf. **Fig. 4.1**), allowing the study of short-term effects during a solar event.

Table 4.1 below summarises the parameters of the proposed ESCAPE orbit.

Table 4.1: ESCAPE orbit parameters.

Initial Perigee Altitude	800 km
Apogee Altitude	33 000 km (6.2 R_E geocentric distance)
Orbital Period	9 h 45 min
Orbital Plane Inclination	90°
Initial Latitude of the Line of Apsides	85° N
Argument of Perigee	255°
Required routine orbit maintenance manoeuvres	None
Resulting Slow Oscillation of the Perigee Altitude	Between 800 and 480 km
Resulting Rotation of the Line of Apsides	-0.21°/ day (230° in 3 years)

4.1.3. Target regions coverage by the proposed orbit

To test the coverage of the scientific target regions by the proposed orbit, during the 3-year nominal mission, we have geometrically defined three regions for the **in-situ measurements** (cf. **Fig. 4.4**):

- **Lower exosphere:** 500 – 1000 km altitude: 1.56 % per orbit, i.e. ~22 minutes per day, equivalent to 11.2 hours per month. It is the red zone region in Fig. 4.4.
- **Ion upwelling regions (North or South Polar Cap):** 1000 – 5000 km altitude and geomagnetic latitude > 70° (or < -70°): 1.47 % per orbit, i.e. ~21 minutes per day, equivalent to 10.6 hours per month (average over 3 years, taking into account the rotation of the line of apsides). It is the Fig. 4.4 yellow zone region.
- **Ring current region:** 2.5 – 5 R_E geocentric distance and -45° < geomagnetic latitude < 45°: 34 % per orbit, i.e. > 8 hours per day. It is the green zone region in Fig. 4.4.

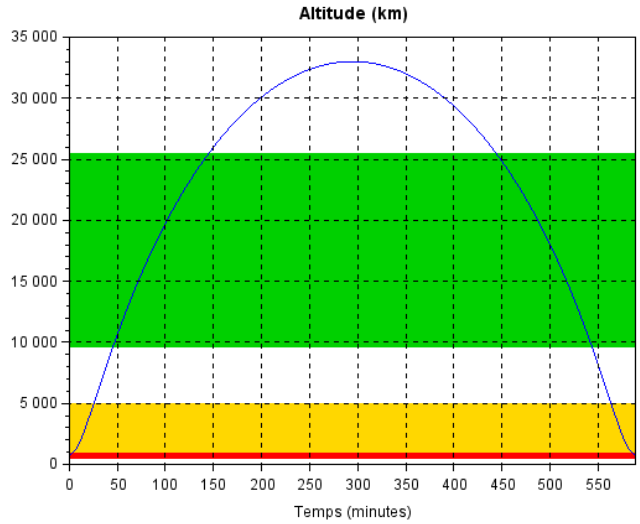

Fig. 4.4: ESCAPE orbit altitude versus time (in minutes) after perigee pass. Red zone: Lower exosphere; Yellow zone: Ion Upwelling region; Green zone: Ring current region.

We note that the "white and green zone" above 5000 km altitude, in **Fig. 4.4**, is perfectly suited for **remote sensing observations** of the lower exosphere and limb, using the UVIS and AMC instruments. It is also used for in-situ measurements of the upper exosphere.

4.1.4. ESCAPE spacecraft launch

Considering a ~700 kg total wet mass satellite, including all margins (cf. §4.2.4), and the ESCAPE orbit parameters, an **Ariane A62 launcher** is the most suitable for an injection to the mission operational orbit, as shown below.

A scaling of the announced (for a GTO orbit) A62 performance characteristics to the ESCAPE orbit shows that A62 is capable to launch ~2800 kg to the ESCAPE orbit, i.e. a ~2700 kg satellite considering a ~100 kg satellite adapter. There is thus more than adequate mass margin for the proposed mission launch.

Taking into account the re-ignition capacity of the A62 upper stage, the constraints on the argument of perigee are weak.

The A62 launcher can thus perform a **direct injection into the ESCAPE operational orbit**, with the satellite spin axis initially along the velocity vector direction, and no major orbital manoeuvres are then required by the satellite. The remaining manoeuvres are for attitude control, with an orientation of the satellite spin axis along the Sun direction followed by the spin-up manoeuvres.

4.1.5. Radiation environment of the ESCAPE orbit

In order to estimate the total ionising and non-ionising doses expected during the ESCAPE 3-year mission the **SPENVIS tool has been used**, and a series of simulations have been performed to test various combinations of orbit parameters:

- Perigee altitude (km): 450, 500, 600
- Apogee altitude (km): 27 000, 33 000
- Inclination: 75°, 80°, 85°, 93°
- Argument of perigee: 60°, 90°, 120°
- Mission years: 2029-01-01 to 2032-01-01.

The results show that the inclination has very little effect on the total dose. The reason for this is that modifying the inclination does not really change the fraction of time spent in the radiation belts.

Concerning the perigee change there is little difference between 450 km or 500 km perigee, but the total ionising dose for a 600 km perigee orbit is about 4 times lower.

We will thus show the simulation results for a 500 x 33 000 km 75° inclination and 90° argument of perigee orbit, one of the most demanding.

We consider both the solar minimum and solar maximum case for the trapped radiation. Note that for SEPs and GCR we use the expected radiation levels for the actual epoch. The results, for the 4π sr dose in the centre of an aluminium sphere, are shown in **Fig. 4.5** separately for electrons, trapped protons, SEPs, bremsstrahlung X-rays and the total dose.

It appears that the total dose is by about a factor of 4 lower for the trapped particles for solar minimum conditions (if no absorber is present), indicating that the trapped particles dominate. For shielding thicknesses below 3 to 4 mm Al the trapped electron flux dominates; whereas for larger absorber thicknesses the trapped proton flux sets the limits. For the non-ionising dose calculations performed here, the trapped protons are important (**Fig. 4.6**). There is little difference between solar minimum and solar maximum conditions for the AP-8 flux, so the non-ionising dose is similar in both cases.

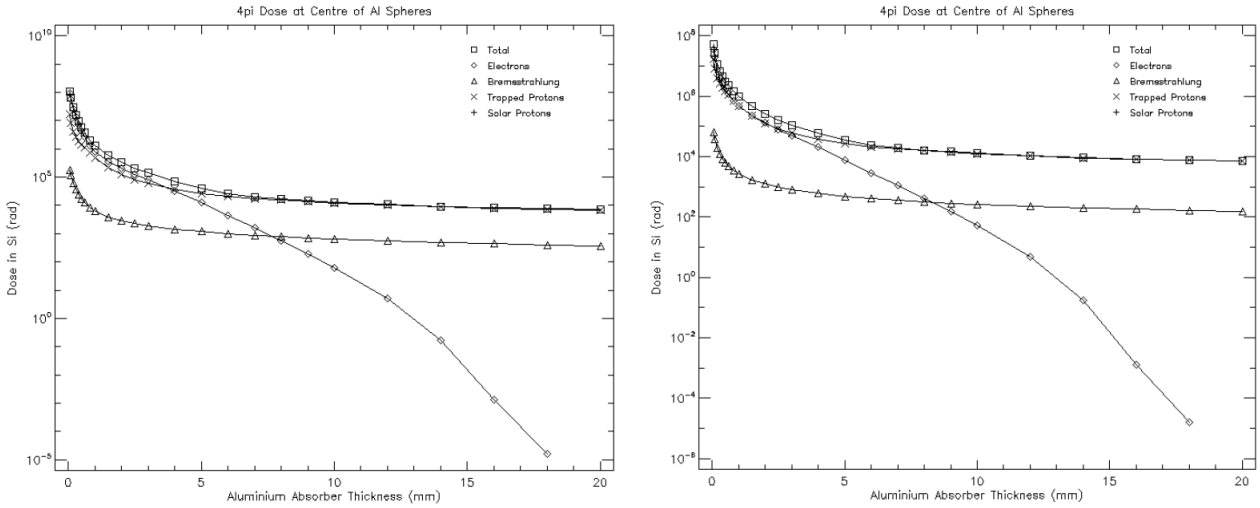

Fig. 4.5: Total ionising dose in silicon (rad) as a function of the aluminium shielding thickness (mm) for: solar maximum (left panel) and for solar minimum (right panel) conditions.

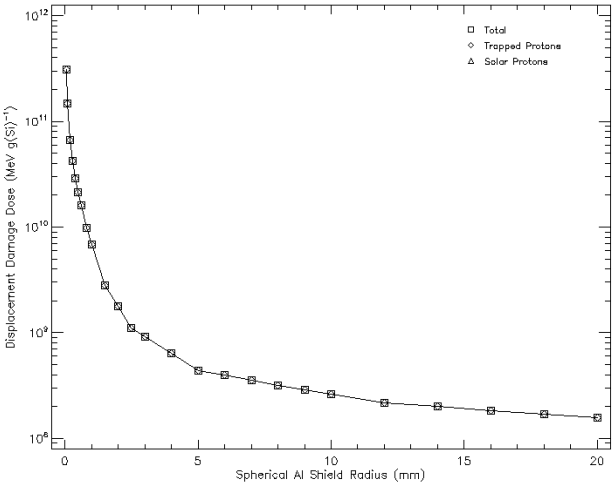

Fig. 4.6: Total non-ionising dose for trapped particles under solar maximum conditions.

In conclusion, the radiation environment of the ESCAPE mission is strongly influenced by the trapped radiation belts. The larger part of the dose is due to the trapped electrons, **shielding is therefore rather effective**. Our study shows that **ESCAPE will experience total ionising doses, after 3 years, of maximum ~35 – 40 krad behind 5 mm of aluminium shielding**, which is thus adequate to satisfy the <50 krad on EEE level requirement. Behind only 3 mm Al the expected total ionising doses would be ~150 – 200 krad.

More detailed orbit simulations will have to be performed during a Phase A study to obtain a more precise assessment of the dose, including the effects of the natural evolution of the orbit as the mission proceeds (cf. §4.1.2) and to estimate also the expected SEU rate.

4.2. Spacecraft design

4.2.1. Requirements for the spacecraft design

To accommodate both the in-situ measurement instruments and the remote sensing instruments some unique characteristics are required:

- The SC must be spinning, so as to allow the particle detection instruments to cover the full 3D space every spin. The SC must be spinning also to allow the deployment of the SLP wire booms.
- The spin period should be 20 – 24 s. This is defined from the energy sweeping time scale and the required angular resolution of the particle detection instruments (about 2.5 – 3 s full energy sweep and 8 azimuthal sectors).
- The SC must have a constant attitude with respect to the Sun, so as to maintain the SLP probes continuously exposed to sunlight. The SC must have a constant attitude with respect to the Sun also in order to maintain a constant spacecraft surface exposure to sunlight. This helps to avoid evaporation of eventual condensed volatiles if cold shadowed surfaces were to be suddenly exposed to sunlight.
- The SC must provide a pointable platform for the mounting of the remote sensing instruments (UVIS and AMC), allowing stable pointing to the selected remote sensing target region: lower exosphere, auroral oval, or limb scans.
- The required pointing accuracy is 1° (0.1° knowledge).
- The SC must allow, for the remote sensing instruments, auroral zone view for the inbound and/or outbound orbit legs.
- The instruments must be placed such that there is minimum blockage by spacecraft appendages.
- The SC must satisfy moderate (Cluster level) magnetic cleanness and EMC requirements.

- External conductive surfaces, linear regulated power system, and distributed single-point-ground power system are required for basic EM cleanliness.
- The power and telemetry supported by the SC must allow continuous operation of all experiments.
- 10 GByte onboard memory is required for data storage before transmission to a ground station.
- During the operational phase of the mission the SC should not use for orbit or attitude control nitrogen containing propellants, e.g. hydrazine. Nitrogen is a key element of the ESCAPE measurements, and any contamination of the measurements by decomposition / condensation / evaporation of propellants or their fragmentation products should be avoided. For the same reason CH_4 (propane) as propulsion gas has also to be excluded, because propane has major fragments on mass 28 ($^{14}N_2$) mass 29 ($^{14}N^{15}N$) and also a bit on mass 15 (^{15}N).
- Outgassing and material decomposition under the influence of solar UV must be minimised, to avoid contamination of the measurements by gas.
- The optical instruments (UVIS and AMC) should avoid the contamination by solar UV.
- The SC must execute an end-of-life deorbiting manoeuvre.

4.2.2. Proposed spacecraft design

Following an analysis performed in cooperation with the CNES PASO (*Plateau d'Architecture des Systèmes Orbitaux*), to satisfy in an optimum way the above requirements we propose a **Sun-pointing spin stabilised spacecraft** (~3 rotations per minute), **equipped with a despun platform**.

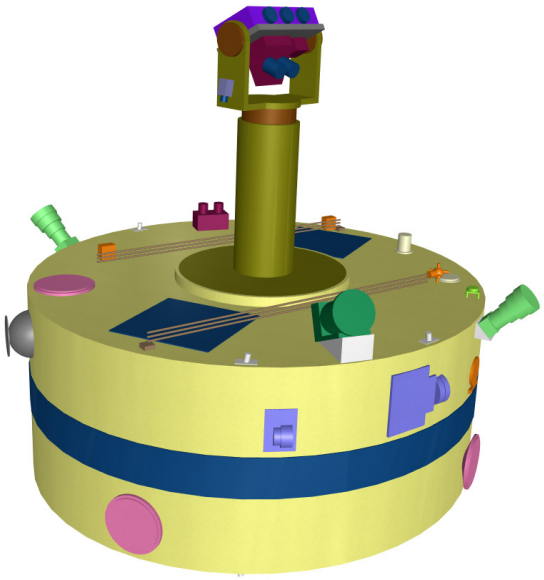

Fig. 4.7.a: ESCAPE spacecraft design, equipped on its top with a despun platform. Booms not deployed in this representation.

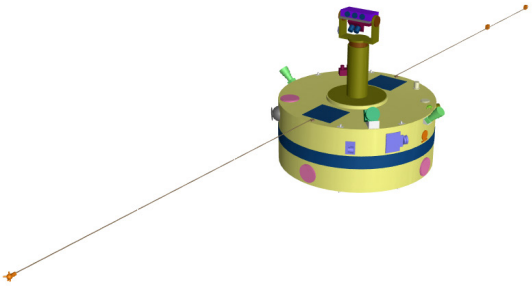

Fig. 4.7.b: ESCAPE spacecraft design, all booms deployed. The rigid boom at the upper right bears the two MAG sensors. The boom at the lower left bears the Search Coil sensor. The SLP sensors are at the tips of two wire booms and one of them is visible (not in scale) at the upper left corner.

The main structure of the spacecraft is a 3500 mm diameter x 1000 mm height cylinder, equipped on its centre with a 350 mm diameter x 1500 mm mast bearing on its top the despun platform (cf. **Fig. 4.7.a** and **4.7.b**).

The **despun platform** has an one-axis articulation for elevation scans and bears the UVIS instrument ("blue" instrument on the top) and the AMC camera ("magenta" instrument). Next to AMC is a DPU for serving both instruments and providing a digital interface with the main spacecraft. One side of the despun platform is equipped with a small service camera, looking towards the main spacecraft: visual control of the booms deployment, of the despun platform phasing, etc. A rotating contacts slip-ring assembly is used for power and serial digital signal transmission between the despun platform and the main spacecraft. Heaters are used to maintain the temperature on the optics of the two instruments, and avoid condensation.

Such despun platforms have been used previously for the Giotto spacecraft antenna and also for the antenna assemblies of Meteosat 1st generation and, more recently, Meteosat 2nd generation satellites (7-year life expectancy, P_{spin} = 100 rpm).

The main structure of the ESCAPE spacecraft has the particle detecting instruments on its periphery, and two deployable rigid booms, 5-meters each, at its top surface (cf. **Fig. 4.7.**a and b). One of these booms is for the magnetometer sensors and the other for the ELF-VLF Search Coil sensor. The SLP sensors are at the tips of two 15 – 20 -meters wire booms, orthogonal to the rigid booms, deployed by centrifuge.

4.2.3. Spacecraft attitude and orbit control system

As indicated, the spacecraft has its **spin axis Sun-pointing**. In order to avoid exposure to sunlight of the remote sensing instrument, the **despun platform**

is in the anti-sunward direction (always in the shadow of the spacecraft, which is favourable for optical instruments), whereas the opposite of it side of the spacecraft, which is facing the Sun, is covered with solar panels. A narrow belt of solar panels, all around the spacecraft periphery, and two small solar panels at the spacecraft top surface, insure power supply following launch, i.e. before the orientation of the spin axis to the operational Sun-pointing attitude, or in case of contingency.

Maintenance of the Sun-pointing spin direction requires **regular attitude manoeuvres**, i.e. a ~1° per day manoeuvre, to compensate for the yearly Earth movement around the Sun (**Fig. 4.8**).

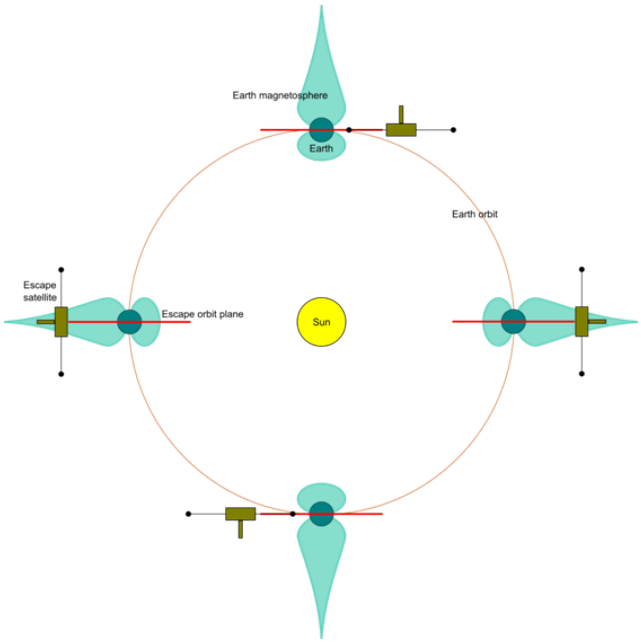

Figure 4.8: ESCAPE orbital plane (red) with respect to the Sun-Earth system, during the year. The SC despun platform (small brown mast) is always in the anti-sunward direction, whereas the SLP probes are continuously exposed to sunlight. The Earth's magnetosphere is represented in light blue.

The proposed spacecraft attitude control system uses as input: (a) two solar sensors, at the two opposite sides of the spacecraft; (b) two star sensors, obliquely looking around the anti-solar direction (the low light-green baffles in **Fig. 4.7**).

Since an hydrazine-based attitude control system is not allowed (cf. §4.2.1), and methane or cold nitrogen are not allowed either, an **inert cold gas system based on Xenon or Krypton** has to be adopted. Although the specific impulse values of these two gases (27 and 35 s respectively) are not high, they offer the advantage of not polluting the measurements of the particle instruments and, as we will show, their performances are more than adequate for the mission requirements.

The proposed system is based on (cf. Annexe-C):

- 8 thrusters at the "edges" of the spacecraft, inclined at 15° to generate thrust or torque in all necessary directions. Each of them develops a 20 mN thrust and they are used for the spin-up, attitude manoeuvres , or for eventual orbit manoeuvres.
- 4 small (300 mm diameter) cold gas tanks.

The estimation, of the thruster operation duration necessary to perform the 1° daily attitude manoeuvre has been performed based on the spacecraft moment of inertia and a symmetric 2x2 thrusters operation at two opposite sides (~100 mNm torque). The resulting thrust duration, for a 1° spin axis pointing manoeuvre, is ~57 s, which is relatively long compared to the spin period (~20 s). So the thrust has to be fractioned in a small series of shorter pulses, synchronised with the spin phase. Considering that the efficiency of such a pulsed thruster operation is about 40% of a nominal continuous operation, and the use of Xenon as propellant gas, it results that the propellant consumption is 7 g per day for attitude control, or **7.6 kg of Xenon for a 3-year mission**.

The proposed spacecraft configuration, considering a 75% tank filling, **provides ~120 kg of Xenon**. Since only 7.6 kg of Xenon are necessary for attitude control during the nominal 3-year mission and A62 can perform a direct injection of the spacecraft into its operational orbit, there is a huge propellant margin available for:

- eventual mission extensions;
- eventual orbit modifications during the mission.

For the **end-of-life deorbiting manoeuvre** the hydrazine avoidance requirement is not any more mandatory. A **monopropellant hydrazine system** is thus proposed (I_{sp}=200 s), with a 20 N thruster and a 500 mm diameter hydrazine tank at the central axis of the spacecraft. Considering again a 75% filling this **provides ~50 kg of hydrazine**. A **controlled re-entry manoeuvre** (ΔV~87 m/s, cf. §4.1.2) would **require ~23 kg of hydrazine**. A perigee altitude reduction manoeuvre (ΔV~20 m/s) would require ~5 kg of hydrazine. In both options there is a huge margin available for any manoeuvres or contingency.

It is noted that the re-entry manoeuvre is preceded by an attitude manoeuvre, using the nominal Xenon thrusters system, in order to orient the spacecraft spin axis in the required direction.

4.2.4. Spacecraft mass budget

Table 4.2 provides the spacecraft bus mass break-down, with/without margins. The total **dry** spacecraft bus mass **including margins** is **338.7 kg**.

The **propellant mass**, considering as indicated in section 4.2.3 a tank filling at 75% of the maximum capacity, is 120 kg Xe + 50 kg hydrazine = 170 kg, or **204 kg including margins**. We note however

that, as indicated previously, to satisfy the nominal mission requirements a mass of ~10 kg Xe + ~24 kg hydrazine = 34 kg would be adequate.

Table 4.2: ESCAPE spacecraft bus mass budget, including propellants for extended mission/contingencies.

PAYLOAD	Target wet mass [Kg] :				Without margin [Kg]	Margin [%]	Margin [Kg]	Including margin [Kg]
Subsystem	Unit							
	Name	Quantity	Mass [Kg]	Margin [%]				
Subsystem Ion and Neutral Mass Spectrometer					5,50	20,00%	1,10	6,60
Subsystem MCP Ion Mass Spectrometer					7,50	20,00%	1,50	9,00
Subsystem Nitrogen Oxygen Ion Analyser					8,00	10,00%	0,80	8,80
Subsystem Plasma Electron And Current Experiment					7,00	20,00%	1,40	8,40
Subsystem MAG					3,40	12,35%	0,42	3,82
Subsystem Sweeping Langmuir Probe					12,60	20,00%	2,52	15,12
Subsystem WAVES					7,40	11,89%	0,88	8,28
Subsystem Energetic Neutral Atoms Imager					6,00	20,00%	1,20	7,20
Subsystem UV Imaging Spectrometer					8,50	20,00%	1,70	10,20
Subsystem Auroral Airglow Camera					14,20	20,00%	2,84	17,04
Subsystem Active Spacecraft Potential Control					3,50	20,00%	0,70	4,20
Subsystem Energetic Mass Spectrometer					9,60	20,00%	1,92	11,52
Subsystem PLDPU					6,00	20,00%	1,20	7,20
	DPU Particle Instruments	1	3,00	20,00%	3,00	20,00%	0,60	3,60
	DPU Cameras	1	3,00	20,00%	3,00	20,00%	0,60	3,60
Subsystem Wide field Cold Ions Mass Spectrometer					5,00	20,00%	1,00	6,00
Total dry mass without system margin					**104,20**	**18,41%**	**19,18**	**123,38**
System margin						20,00%	**24,68**	**148,06**
Total wet mass including all margins								**148,06**

Table 4.3: ESCAPE payload mass budget.

BUS	Without margin [Kg]	Margin [%]	Margin [Kg]	Including margin [Kg]
Subsystem				
Subsystem STRUCTURE	74,55	20,00%	14,91	89,46
Subsystem POWER	51,42	20,00%	10,28	61,70
Subsystem AOCS	5,47	9,88%	0,54	6,01
Subsystem COMS	21,70	14,52%	3,15	24,85
Subsystem OBDH	19,00	20,00%	3,80	22,80
Subsystem PROPULSION	29,91	6,50%	1,95	31,86
Subsystem Despun Platform	38,02	19,87%	7,55	45,57
Total dry mass without system margin	**240,07**	**17,57%**	**42,18**	**282,26**
System margin		20,00%	**56,45**	**338,71**
Propellant mass	**170,00**	**20,00%**	**34,00**	**204,00**
Total wet mass including all margins				**542,71**

Table 4.3 provides the payload mass break-down, with/without margins. The **total ESCAPE payload mass, including margins and booms, is 148 kg**.

The **total system mass**, i.e. spacecraft bus + payload + propellants (filling at 75%) + all margins is **690.7 kg, including margins**, which implies that a spacecraft not exceeding 700 kg, during launch, is the baseline of the proposed mission.

4.2.5. Spacecraft power budget

Table 4.4 provides the spacecraft bus power break-down, during the different mission phases,

with/without margins. The **maximum spacecraft bus power** consumed, during data transmission to a ground station (most demanding configuration) and **including all margins, is 299.1 W**.

Table 4.4: ESCAPE spacecraft bus power budget.

BUS						
+ -	Subsystem	↑↓ Element Modes >	LAUNCH	MISSION	MISSION + TRANSMISSION	DEORBITATION
			Element mode LAUNCH	Element mode MISSION	Element mode MISSION + TRANSMISSION	Element mode DEORBITATION
▼	POWER Subsystem	Without margin [W]	0,1	24,2	24,2	24,2
		Including margin [W]	0,12	29,04	29,04	29,04
▼	AOCS Subsystem	Without margin [W]	0	17	17	17
		Including margin [W]	0	17,85	17,85	17,85
▼	COMS Subsystem	Without margin [W]	13,15	13,15	148,2	13,15
		Including margin [W]	14,37	14,37	176,43	14,37
▼	OBDH Subsystem	Without margin [W]	36,8	44,8	44,8	36,8
		Including margin [W]	41,08	50,68	50,68	41,08
▼	PROPULSION Subsystem	Without margin [W]	0	19,1	19,1	47,6
		Including margin [W]	0	19,1	19,1	47,6
▼	Despun Platform Subsystem	Without margin [W]	0	6	6	0
		Including margin [W]	0	6	6	0
Consumed power without margin			50,05	124,25	259,3	138,75
Consumed power including margin			55,57	137,04	299,1	149,94

Table 4.5: ESCAPE payload power budget.

PAYLOAD					
+ -	Subsystem	↑↓ Element Modes >	OFF	In-situ measurements	In-situ + Cameras
			Element mode OFF	Element mode IN-SITU	Element mode IN-SITU + CAMERAS
▼	Subsystem Ion and Neutral Mass Spectrometer	Without margin [W]	0	17	17
▼	Subsystem MCP Ion Mass Spectrometer	Without margin [W]	0	8	8
▼	Subsystem Nitrogen Oxygen Ion Analyser	Without margin [W]	0	8	8
▼	Subsystem Plasma Electron And Current Experiment	Without margin [W]	0	8	8
▼	Subsystem MAG	Without margin [W]	0	5,5	5,5
▼	Subsystem Sweeping Langmuir Probe	Without margin [W]	0	0	0
▼	Subsystem WAVES	Without margin [W]	0	9,6	9,6
▼	Subsystem Energetic Neutral Atoms Imager	Without margin [W]	0	9	9
▼	Subsystem UV Imaging Spectrometer	Without margin [W]	0	0	20
▼	Subsystem Auroral Airglow Camera	Without margin [W]	0	0	22
▼	Subsystem Active Spacecraft Potential Control	Without margin [W]	0	3,7	3,7
▼	Subsystem Energetic Mass Spectrometer	Without margin [W]	0	7,1	7,1
▼	Subsystem PLDPU	Without margin [W]	0	3	6
▼	Subsystem Wide field Cold Ions Mass Spectrometer	Without margin [W]	0	3	3
Consumed power without margin			0	81,9	126,9
Consumed system power margin		20,00%	0	16,38	25,38
Total consumed power including system margin			0	98,28	152,28

The **instrument power** break-down is given in Table 4.5. Note that here the margins are not given per instrument, but a total payload power margin of 20% is added at the bottom of the table. The maximum payload power consumed**, including all margins**, is **152.3 W.**

The **total system power budget**, i.e. spacecraft bus + payload, during data transmission to a ground

station (few minutes per day, cf. §4.2.6) and **including all margins, is 451.4 W**. The main solar panels, at the "bottom" side of the spacecraft which is continuously facing the Sun during normal operations, are thus sized for a 450 W power supply. Outside data transmission windows the total system power budget, including all margins, is 289.3 W.

A battery is foreseen for eventual peak power situations, launch operations, eclipses and contingencies.

4.2.6. Spacecraft telemetry and command system

For **payload telemetry (TM)** transmission, which is the most demanding, an **X-band system** is chosen whereas for **housekeeping telemetry and for commanding (TC)** an **S-band system** is considered as the baseline.

The proposed ESCAPE TM telecoms system has been designed to be operated around apogee (i.e. above 20 000 km), where the passes are longer. The following ESATRACK stations are proposed, considering the slow rotation of the line of apsides described in §4.1.2:

- Kiruna during the 1st year, when the ESCAPE orbit apogee is mostly in the northern hemisphere;
- Kourou successively, when the apogee is close to the equator;
- New Norcia or Malargüe when the apogee is mostly in the southern hemisphere.

New Norcia and Malargüe are DSN stations equipped with 35 m de diameter antennas, whereas Kiruna and Kourou are equipped with 15 m antennas.

Table 4.6: ESCAPE visibility of the selected ESATRACK stations, in minutes per day.

Station visibility (minutes/day)	Kourou	Kiruna	Malargüe	New Norcia
1st year	411	986	174	191
2nd year	404	270	637	611
3rd year	242	41	955	906

Table 4.6 gives the daily visibility of each of these stations during the 3 years of the nominal ESCAPE mission. It results that:

- During the 1st year Kiruna is the best suited station, even if Kourou can supply some additional coverage if needed.
- During the 2nd year the two southern hemisphere stations provide sufficient coverage, even if Kourou can again supply some additional coverage if needed.
- During the 3rd year the use of the southern hemisphere stations is necessary.

Concerning the onboard antenna configuration, the use of isoflux antennas is proposed. To ensure a 4π sr coverage, the baseline configuration is:

- 1 antenna on each of the +Z and -Z sides of the main structure of the spacecraft;
- 4 antennas on the periphery of the spacecraft, switched from one to the next one at the spin frequency and used when Earth is visible "at the side". A 10 dB gain is proposed.

The proposed onboard equipment is dimensioned for 13m ground antennas, and is based on a travelling waves tube amplifier of 30 W RF. The amplifier efficiency being ~45%, the consumed electric power during emission is ~70 W, plus 30 W for coding, modulation, etc., i.e. 100 W total. The maximum transmission rate is then estimated at 100 Mb/s.

The expected payload data production rates are given in §3.5, Table 3.2.

Considering a 90% normal data rate and a 10% peak data rate production, and adding packets overhead and margins, there are **~18.6 Gb per day to download to ground stations**. For a 50 Mb/s data download rate this requires 6.2 minutes per day of station visibility, or 3.1 minutes per day for a 100 Mb/s data download rate. A comparison with the available station visibility windows, shown in Table 4.6, indicates that there are **enough margins and only a small fraction of the available visibility windows is needed for data transmission**.

4.2.7. TRL level of the proposed spacecraft subsystems

The spacecraft bus subsystems and equipment, in the proposed spacecraft preliminary design, are either:

- based on existing flight-proven equipment, used e.g. onboard the *Myriades* or *Pléiades* product line, or are off-the-shelf equipment, and in this case their **TRL level is 9**; avionics and attitude control and propulsion equipment are such examples;
- or derived from existing flight-proven equipment, but some adaptation or development would be required, and in this case their **TRL level is at least 6**; the battery is such an example;
- or needing development, but are based on simple or commonly used elements, and a **TRL level 6 will be reached at the end of Phase A study**. This is particularly the case of the despun platform, which is based on elements such as two main mechanical parts, two electric motors + two position encoders, a slip-ring assembly and a command and control module. As indicated in §4.2.2 similar despun platforms have shown their reliability.

The scientific instruments TRL level is given in section 3, Table 3.1.

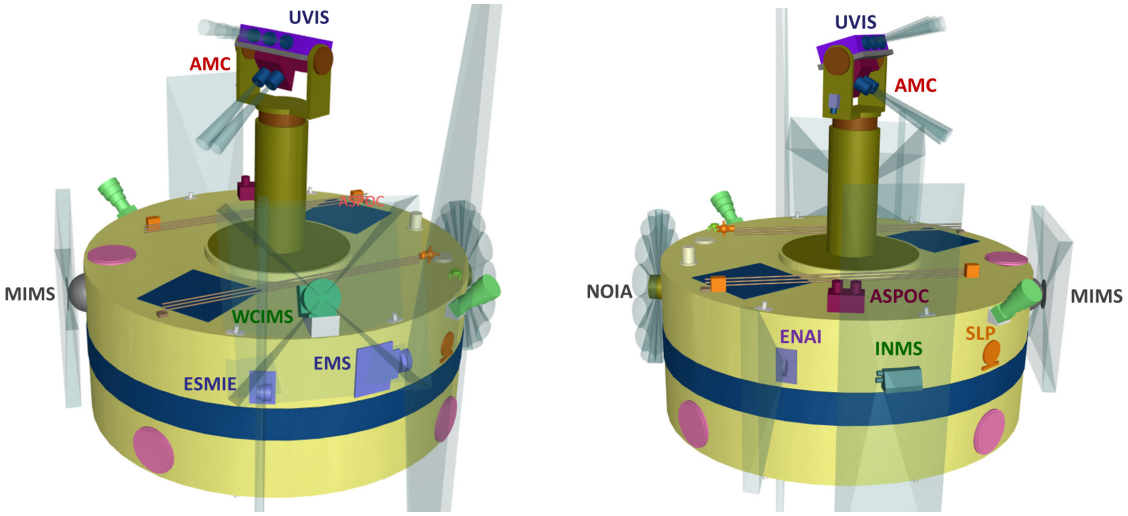

Fig. 4.9: Instrument accommodation on the ESCAPE spacecraft, with their FOVs. Two opposite sides of the spacecraft are shown. The booms, in these representations, are not deployed.

4.2.8. Instrument accommodation

The accommodation of the scientific instruments on the ESCAPE spacecraft, with their fields-of-view (FOV), is shown in **Figures 4.9**. A cut-view of the instruments accommodation is given in Annex-C. All instruments have a FOV clear of spacecraft appendages or other obstacles.

4.3. Ground segment

ESCAPE spacecraft TC/TM transmission and ground station coverage are described in §4.2.6

All commands, including the instrument on/off, will be performed by time-tagged commanding after the initial commissioning period of first 2 months. Real-time commanding will be required only for instrument commissioning and for contingencies.

All received TM data are processed first at ESOC where the level 0 (telemetry) data are unpacked and converted to level 1 (raw) data, for distribution to each PI institute. Due to the non-criticality of the platform operation (no real-time manoeuvres during the nominal mission), weekly platform commands are uplinked from ESOC.

Higher-level data processing and science products generation is performed at the PI institutes.

4.4. Operations

4.4.1. Science operation phases and modes

The mission has four phases:

(1) Initial health check phase and commissioning (from the launch until the end of the functional test of each instrument after sufficient outgassing of the spacecraft). During this time we need real-time or semi-real-time operations and therefore the ground stations must provide good real-time contact. Since many instruments use HV supplies, we need to wait one month (outgassing) before the first instruments with HV supplies can be switched on. We also need to examine the level of ion contamination from both manoeuvres and attitude control. This will take about 2 months from the launch.

(2) Nominal science phase (3 years): The high initial apogee latitude allows the spacecraft to spend large amount of time over the northern polar cap escape route in its outbound leg, favouring at the same time conjugate observations with EISCAT -3D, and in the ring current during the inbound leg (cf. **Fig. 4.1**). Due to the natural orbit evolution the apogee successively moves close to the equatorial plane (2nd year), surveying the ring current near the equatorial region, just outside the outer radiation belt where many past observations by the geosynchronous satellites have been performed. This allows us to compare our high mass resolution results with ion measurements from geosynchronous satellites and to cross check the energy and effective geometric factors. At the same time the perigee is in the equatorial lower exosphere, another target region. During the 3rd year the ESCAPE orbit apogee will be in the southern hemisphere, to survey the southern polar cap escape route, while the perigee will be in the northern lower exosphere. This mission time will cover quick rise of the solar activity from the solar minimum to solar maximum.

(3) Bonus phase (in case a 2-year extension is approved): Continued orbit evolution, in conjunction with eventual orbit manoeuvres, will allow an extended coverage, and hopefully observations during an early declining phase of the solar activity.

(4) End of mission phase (deorbiting): We switch-on all instruments, taking advantage of the unique re-entryinto the atmosphere, because we expect unusual heavy ion formation. This could be used as a reference for meteor burning.

During nominal operations the pointable despun platform will be programmed for looking on selected targets: lower exosphere, atmospheric limb scans, auroral zone imaging, zenith observations, or stars for calibration. This is achieved through the two degrees of freedom capabilities of the despun platform system: one-axis articulation (axis perpendicular to the spacecraft spin axis, cf. **Fig. 4.7**) and spin-phase adjustment for the despun function.

4.4.2. Calibration

We will also have cross calibration between different ion instruments, by comparing over the range where more than two instruments cover the same parameter (overlapping mass and energy for particle instruments, and overlapping frequency for MAG and the search coil). We do not need to have a special campaign for such calibrations but can just compare data taken during normal modes. However, as mentioned above, the use of the cold gas propulsion (Xe or Kr) for the attitude control gives us the opportunity of mass calibration for the cold or low energy ion mass spectroscopy, and therefore we will sometimes keep instruments on during (or immediately after) such attitude control manoeuvres.

5. Management scheme

5.1. Organization and responsibility

During the pre-study phase and until ESA appoints the **Project Scientist(s)** from ESA, the **ESCAPE Science Working Team (SWT)** that includes all instrument PI teams and CoIs teams is led by four European core teams: IRAP (Dandouras), IRF (Yamauchi), BIRA-IASB (De Keyser) and ISS (Marghitu). IRAP (mission PI institute) is the single point contact and is working in close cooperation with IRF (mission Co-PI institute). ISS is the Interdisciplinary Analyses Coordinator institute, to enhance the multi-disciplinary nature of the mission. In addition to this European core, UNH (Kistler) is the scientific contact point between ESA and NASA (through IRAP). The scientific contact point to JAXA (ISAS is the actual manager) is IRF's role.

The Project Scientist will chair the SWT and is responsible for all the above interfaces between ESA and the PI/CoI teams. The SWT is responsible for (1) science planning including calibration and telemetry re-distribution, and (2) science operations planning. Based on the approved plans, each PI team creates data products for data analysis and archives them for open use (see §5.4 for details). It also creates an individual command plan, which is assembled by ESOC based on the operations plan. All the ESOC activities are ESA's responsibility.

Since the payload includes also US instruments and Japanese instruments, the mission needs support from NASA and JAXA for the SI level. We do not expect those agencies to provide spacecraft support. All manufacturing and operation elements, except SIs, are ESA's responsibility. No other space agency is involved. As for the coordinated observation with the ground-based facility, EISCAT will be the main contact during the mission, with IRF as contact during the preparation phase. The financial situation for the payload support is summarised in §6.2.

5.2. Tasks during mission study and implementation (Phases A-D)

Throughout Phases A-D the SWT's tasks are, in addition to the tasks as SI preparation:

- Keep update of SI's maturity margin.
- Review and approve proposals of new CoIs on the hardware level.

5.2.1. Phase A

This phase is led by ESA, and the SI teams are responsible for working closely with ESA for the mission and spacecraft preliminary design, evaluation of possible technical options, preliminary design of their instruments, or implementing requests from ESA about the design of their instruments. The major tasks for ESA during this phase are as follows.

- Instrument TRL level is examined. Although the majority of the SIs are simply copies or minor modifications of instruments that actually took data in the past or on on-going space missions, several SIs are newly developed (they reached TRL=5-6). All SIs will be re-examined from the viewpoint of the purpose and area of operation (relatively high radiation dose) of the mission, mainly through documentation, during this preliminary study phase.
- The optimum orbit and attitude control method will be tuned. Although we have done extensive analysis and found acceptable orbit parameters and attitude control methods as described in the previous section, for which the CNES PASO found it is feasible to construct an appropriate spacecraft, there may exist even better or more cost-effective solutions.
- The launch procedure must be examined in detail.

- The attitude control system, for which a preliminary analysis is given in §4.2.3, must be examined, e.g., type of inert cold gas used: Xe or Kr.
- The final satellite platform including equipment must be defined and designed through contact with all SI teams, because changing the platform for one instrument might interfere another SI's observations.
- A preliminary design will be required for the despun platform system: axis mounting, articulation, slip-rings, position encoders, power and digital data transmission to/from the platform.
- Downlink and uplink station selection must be validated, cf. §4.2.6 for a preliminary analysis.

5.2.2. Phase B (Definition phase)

The ESCAPE implementation schedule is assumed to follow the ECSS phased approach. The definition phase ends with a Preliminary Design Review. This will be followed by the RFP & Tender Evaluation Process for the System Prime Contractor.

5.2.3. Implementation Phase (C/D)

It is foreseen that ESA is Mission Responsible and issues an overall industrial contract for the space segment to a System Prime Contractor. Due to the "thin Prime approach" favoured by ESA in the Science Programme (first used on SolO), and also governed by geographic return constraints, it is foreseen that the System Prime Contractor may subcontract the provision of spacecraft elements to different suppliers.

The System Prime Contractor will be overall responsible for the integration of payload with the spacecraft and the overall System PFM Assembly, Integration, and Test (AIT) campaign. The System PFM AIT is followed by the Flight Acceptance Review (FAR), which gives the go-ahead for spacecraft shipment to the launch site. The successful FAR marks the formal delivery of the spacecraft to ESA.

ESA will rely on the national delegations for the funding and provision of the payloads, and provide these to the System Prime Contractor as Customer Furnished Equipment (CFE). Concerning the system interface to the PIs, it is proposed to be handled by a single contact point for each instrument PI. It is further assumed that ESA has the responsibility for the procurement, preparation and execution of the launch and spacecraft operations.

The development and/or procurement of booms and payload mechanisms may be included as part of the System Prime Contractors tasks, or procured separately by ESA and provided to the System Prime Contractor as CFE. In the latter case, the specification and SoW for these items shall be jointly agreed by the concerned PIs, the System Prime Contractor, and ESA.

ESA will also be in charge of the procurement of the ASPOC instrument, since this is a facility instrument (spacecraft potential control), not performing scientific measurements. ESA will also supply the hardware of the two payload DPUs, one on the despun platform serving the remote-sensing instruments and one on the main spacecraft body serving the particle detection instruments.

5.3. Tasks after launch (Phase E)

5.3.1. Launch & Early Orbit Phase (LEOP/Phase E1)

The launch campaign is proposed to be performed under overall ESA management, with full technical support provided by the System Prime Contactor. The LEOP and commissioning of the spacecraft platform is performed by ESOC with full support from the System Prime Contractor.

The **commissioning and initial tests of the instruments** will be performed after the commissioning of the spacecraft. During this period, all SI teams test different observation modes and parameter settings to determine the optimum configuration of their instruments. Since during this phase the instrument response should be observed as soon as the command is executed, we need near real-time commanding, as was done for Cluster. What we need to examine is:

- interference from other instruments;
- cross-calibration of energy ranges for ions to adjust the energy tables;
- testing of on-board particle mass classifications for ions to adjust the mass tables.

This phase concludes with an ORR (Operational Readiness Review).

5.3.2. Operational Phase (Phase E2)

The operational phase is performed entirely by **ESOC**, with support provided by the System Prime contractor on an as-needed basis. The command lists for the SIs will be generated by the **SOC** (Science Operation Centre), for checking and uplinking by the **MOC** (Missions Operations Centre). Spacecraft telemetry from the ground station will be provided as CCSDS Space Packets to MOC. The science data will be stored in a central data repository in the SOC from where it can be accessed by all PIs. All activities done by ESOC, SOC, and MOC are ESA's responsibility while the PI's activities are national funding agency's responsibility. ESA-lead facility instruments (ASPOC and boom deployment) are also ESA's responsibility, but despun platform pointing planning should be performed jointly by the UVIS and AMC teams. The SOC has to define the

radiation belt timing, to switch off the instruments, and the visibility timing for line-of-sight operation by UVIS.

ESOC also generates time-tagged commands for scientific instruments, which is an assembly of command requests from each PI. These will be uploaded to the spacecraft weekly. Since power and telemetry supported by the spacecraft allow simultaneous continuous operation of all experiments, the nominal science operation plan preparation would be straightforward. However, ESOC will need at least one week to assemble them because the instrument set is large. Since we do not plan any major manoeuvres with ΔV during the three-year mission, the operation should be relatively simple compared to missions such as Cluster.

5.4. Science management

5.4.1. Data handling and archiving

The **telemetry (Level 0)** data that are received by **ESOC** will be directly uncompressed to produce **raw data (level 1a data)**, and to produce **quick-look plots (QL)**. The format of the QL is defined by the SWT. While keeping both level 0 and level 1a data, ESOC will directly distribute both (level 0 and 1a) data to each PI institute.

Each PI institute is responsible for examining the quality of the level 1a data and processing and cleaning them to produce a **processed data set (level 2a data)** for general analyses by Co-Is as well as all the other PIs by request. The PI institutes are also responsible for producing final **physical parameters (level 3 data)** to store at ESA in a common format, like those at the Cluster Science Archive (**CSA**) or Planetary Data Archive (PDA). We strongly recommend that this final archive includes also raw count data that can easily be converted to physical parameters with a single calibration efficiency table, because this efficiency is one of the parameters that degrades in time and is subject to revision.

Data that are produced within the PI teams include also **summary plots (level 1b)**, and **digital science quality data (level 2b)**, ready to be used in scientific papers. Open distribution to the community will be performed after 1 year (this can be shortened if EU policy of open data changes). The planned content of these open-access data is summarised in **Table 5.1**. The open-access data do not have to be limited to parameters such as moment data for ions (density, velocity, and pressure), but could also include differential energy flux (J_E) or power spectrum density (PSD) that contain more information.

For the final archive we propose to use the **CEF** (Cluster Exchange Format) which has successfully been used for Cluster data exchange and archive, is machine-readable and human-readable, is self-descriptive and a variety of software tools are available for it.

Table 5.1: ESCAPE instruments typical open-access data products

Instrument	Content	Level 1b/2b data (within 1 yr): low and medium resolution	level 3 data (final archive): full resolution
INMS	Cold ions & neutrals	Counts / time	mass spectrograms; cold ions and neutrals densities
WCIMS	Cold ions	Counts / time	mass spectrograms; cold ions moments
MIMS	Hot ions	*E-t* spectrograms, ion moments	$J_E(E, p/a, m)$; Energy-mass spectrograms
NOIA	Hot ions	*E-t* spectrograms	$J_E(E, p/a, m)$; energy mass matrices
EMS	Energetic ions	*E-t* and *Mass-t* & Pitch angle spectrograms at selected *E*	$J_E(E, p/a, m)$; mass-t spectrogram for fixed energies (high resolution)
ESMIE	Electrons	*E-t* spectrogram	$J_E(E, p/a)$
SLP	SC potential, plasma density	spin averaged SC pot; spin-plane *E*-field components	spacecraft potential; estimated density; spin-plane *E*-field components
MAG	Magnetic field	spin averaged *B*-field	1 Hz data, spin averaged data; power spectrogram for < 10 Hz
Waves & Search Coil	EM waves	power spectrogram, magnetic waveform (122 Hz)	power spectrogram for 5 Hz to 20 kHz full waveform (incl. 20k Hz snapshots)
ENAI	ENA images	Counts/time plots; ENA images	$J_E(E, m)$ ENA images
UVIS	UV emission line brightness	Count on detector (spectral and spatial) vs time	Column densities and density profiles; UV images
AMC	Images (visible)	low resolution images	full resolution images
DPU	Energetic particles	Radiation belt boundaries	Radiation belt boundaries

5.4.2. Analyses software and data centre

All software related to limited telemetry processing (decompression and time ordering of received TM packets) and to create level 0 and 1a files, as well as the production of quick-look plots is ESA's responsibility. The SI PIs will provide information on data formats and compression to ESA.

Each PI is then responsible for developing the higher levels of data processing software (2a, 3) from level 0 and 1a data, as well as the programs that produce level 1b/2b data from level 1a/2a data. For data processing and analysis, within the PI teams, programs such as the cl program developed at IRAP for Cluster are expected to be used.

While some science analysis programs will be shared within the PI teams or SWT, the programs to produce level 1b/2b will be provided also to ESA and integrated in a mission-level web-interface program (like the Cluster CSDS/CSA) under ESA's responsibility. Such integration applies also to level 3 data (like those at the CSA).

Because the ESCAPE datasets will have similarities with those of Cluster, this work will be able to use some of the existing structure. The **CDPP** (http://cdpp.eu/) multi-mission data centre is also expected to hold an ESCAPE mission data archive, and to provide data access to the community.

5.4.3. Model-data comparison and Ground-based observations

Since the upwelling ionospheric ions start drifting in the inner magnetospheric after modest pitch-angle scattering, **ion drift models are a strong tool in understanding the fate of scattered ionospheric ions**. Inner magnetospheric drift models have a long history and are already quite advanced, and the proposing team has direct access to three such models. They are the Comprehensive Inner Magnetosphere-Ionosphere (**CIMI**) model (Fok et al., 2014), the Hot Electron and Ion Drift Integrator (**HEIDI**) model (Liemohn et al., 2004), and the Inner Magnetospheric Particle Transport and Acceleration Model (**IMPTAM**) (Ganushkina et al., 2011). These models can simulate the drift motion under any arbitrary magnetic and electric field considered and for any solar wind conditions, and are reliable tools in overviewing the fate of ions. **Exosphere modelling**, as discussed in section 1, is another key activity in support of the ESCAPE observations analysis.

Therefore, **collaboration with modelling experts is very important**, and we have these experts in the team (see Annex-B). University of Michigan (M. Liemohn) and Tsinghua University (F. Tian) will coordinate the modelling activity.

Ground-based 3-D ionospheric radar observations, thanks to the **ESISCAT-3D** facility, and **optical observations** will be performed regularly to **compare with the ESCAPE UV and Visible (UVIS and AMC) observations**. UVIS can cover a large range of the upper ionosphere in the polar region through limb observations by taking advantage of the ESCAPE despun platform scanning capability. It is thus possible to compare these measurements with the vertical observations from the ground even more often than ordinary conjugacy allows. Three ground stations from Scandinavia (Svalbard in Norway, IMAGE network in Finland, and Kiruna in Sweden) have agreed to collaborate in such observations. The **EISCAT Scientific Association has committed to coordinate for conjugate observations with ESCAPE**, and the EISCAT-3D facility (https://eiscat3d.se) will most likely be mature and ready for observations by 2029.

5.4.4. Coordination of different disciplines

Given the interdisciplinary dimension of the ESCAPE mission objectives, coordination between different disciplines and different science tools requires, as mentioned previously, its own coordinator. ISS is **the Interdisciplinary Analyses Coordinator** institute, to enhance the multi-disciplinary nature of the mission. The task is not limited to demand-based coordination, but the coordinator can also take outreach initiatives within the scientific community.

5.4.5. Outreach

Atmospheric escape and evolution is an issue on which there is **substantial public interest**. It is related to the **long-term atmospheric evolution and its impact on the habitability of the planet**, topics for which the society is sensitive. The recent success of the MAVEN mission, and the interest of the public to its results, is a testimony of the broad impact of the subject. Nitrogen and oxygen are familiar to everybody (including school children) and we do not need complicated explanations to persuade the general public about the importance of these elements, and their ratio, in the development of leaving organisms. The **interdisciplinary aspect of the ESCAPE mission** is another strong point for outreach.

The ESCAPE instrumentation, including **imagers** as the Auroral and Airglow Camera, the UV Imaging Spectrometer and the ENA Magnetospheric Imager, will provide material able to captivate the excitement of the public. This can provide a visual support conveying in a simple way the science targeted by the mission.

It is foreseen to make a video explaining the objectives of the ESCAPE mission to a wide level of audiences, from school children to scientists in other fields. An outreach web site will also be developed.

6. Costing

6.1. Spacecraft, launch and operations cost

Table 6.1 summarises the total cost estimate, for ESA, of the ESCAPE mission. Since the mission does not require high precision attitude control for the optical telescope measurements and many of the spacecraft subsystems and equipment are based on existing flight-proven elements, or are derived from them with some adaptation, the spacecraft design does not present any unusual complexity. The only "challenging" subsystem is the despun platform (but even for this there are analogies with the despun platforms of some other satellites such as Meteosat, or the mechanisms used in some reaction wheels assemblies). Furthermore, the mission does not require a high telemetry rate and the use of ESTRACK 13-m and 15-m antennas is baselined, rather than the more expensive 35-m antennas. Operations do not present any particular complexity also because no orbital manoeuvres are planned during the nominal mission.

The **spacecraft cost** presented in **Table 6.1** (**120 M€**) is the result of a breakdown analysis of the various subsystems in the proposed spacecraft design (cf. §4.2), and analogy/scaling with other projects. To this have to be added the cost of **ESA-procured facility instruments**, not performing scientific measurements, as the ASPOC instrument and the two DPUs, one on the despun platform and one on the main spacecraft body (**15 M€**). ESA support to **scientific instruments integration** on the spacecraft and testing is estimated to another **5 M€**.

Chemical cleanliness of the spacecraft and its subsystems implies a **specific programme for reducing outgassing** and in-flight decomposition of materials (such as MLI that decomposes under the action of solar UV). This programme, conducted from the start of the mission, is estimated to **10 M€.**

A 20% **ESA project cost** is foreseen for all these elements, i.e. **30 M€**.

The **ground segment and operations** for the nominal 3-year mission, including SOC/MOC (cf. §5.3.2), ground station tracking and data archival, is estimated at **50 M€**.

To all these items a **15% contingency** is added, i.e. **35 M€**.

Launch by Ariane A62 is a fixed price of **73 M€**.

The **total ESCAPE mission cost**, for ESA, is thus estimated at **338 M€**.

Table 6.1: ESCAPE mission cost estimate for ESA

ESCAPE Mission Element	ESA Cost (M€)
Spacecraft	120
Instrument integration and tests	5
ESA supplied payload elements (ASPOC + 2 DPUs)	15
Chemical cleanliness programme	10
ESA Project Team (ESA internal cost)	30
A62 launch	73
Ground segment and operations	50
Contingency	35
TOTAL	**338**

6.2. Financial condition of the payload

In Table 6.1 cost for the SIs is not listed because they are supported by the national funding agencies. The cost for each SI (adding PI and CoI support) is about 10-15 M€ for particle spectrometers and imaging instruments, 2-5 M€ for the other SIs depending on in-house manufacture or industrial sub-contracts, ending up with about 100-120 M€.

All **European instrument PIs** have already contacted their national funding agencies in order to obtain support and official endorsements for building their instruments.

For **US participation**, the two US instrument PIs are in the process of submitting to NASA a joint letter, in response to the recent NASA Heliophysics Division call for Supporting Letters for participation in ESA M5 proposals.

For the **Japanese participation** (two PI contributions), ESCAPE is already selected as one of the "Research Group" projects in the solar-terrestrial sub groups of JAXA. The Research Group is a preparation phase to judge if the project should start a phase 0 study (Working Group). For example, THOR is one of the Research Groups. Due to long time to the launch, start of the Working Group is normally at the time of the selection at ESA (or selection by ESA is a condition to step forward to phase 0 - Working Group). Therefore their participation, if ESCAPE is selected, is quite safe.

Annex-A: Bibliography

Abe Y., et al. (2000) Water in the early Earth, in "Origin of the Earth and Moon", edited by R.M. Canup and K. Righter, Univ. Arizona Press, Tucson, 413-433.

Aikio A.T., et al. (2004), Temporal evolution of two auroral arcs as measured by the Cluster satellite and coordinated ground-based instruments, Ann. Geophys., 22, 4089-4101.

Airapetian V.S., et al. (2014), Magnetic Interaction of a Super-CME with the Earth's Magnetosphere: Scenario for Young Earth, in "18th Cambridge Workshop on Cool Stars, Stellar Systems, and the Sun", Proceedings of Lowell Observatory (9-13 June 2014), Edited by G. van Belle & H. Harris.

Airapetian V.S. and Usmanov A. (2016) Reconstructing the Solar Wind from Its Early History to Current Epoch, Astrophys. J. Lett., 817(2), L24, doi:10.3847/2041-8205/817/2/L24

Airapetian V.S. et al. (2016), Prebiotic chemistry and atmospheric warming of early Earth by an active young Sun, Nature Geoscience, 9(6), 452-455.

Alfvén H. and Fälthammar C.G. (1963), "Cosmical Electrodynamics, Fundamental Principles", Clarendon, Oxford.

Allen A.L., et al. (2000), Thermal coupling of protons and neutral hydrogen with anisotropic temperatures in the fast solar wind, J. Geophys. Res., 105(A10), 2312323134.

André M. and Yau A. (1997), Theories and observations of ion energization and outflow in the high latitude magnetosphere, Space Sci. Rev., 80(1-2), 27-48.

Ayres, T.A. (1997), Evolution of the solar ionizing flux, J. Geophys. Res., 102(E1), 1641-1651.

Angelopoulos V., et al. (1994), Statistical characteristics of bursty bulk flow events, J. Geophys. Res., 99, 21257-21280.

Ayres T.A. (1997), Evolution of the solar ionizing flux, J. Geophys. Res., 102(E1), 1641-1651.

Balsiger H., et al. (2007), Rosina - Rosetta orbiter spectrometer for ion and neutral analysis, Space Sci. Rev., 128(1-4), 745-801, doi:10.1007/s11214-006-8335-3.

Barabash S., et al. (2006), The Analyzer of Space Plasmas and Energetic Atoms (ASPERA-3) for the Mars Express Mission, Space Sci. Rev., 126(1-4), 113-164, doi:10.1007/s11214-006-9124-8.

Barabash S. et al. (2007), Measurements from Mars Express show that the solar wind is removing only a small amount of Mars' atmosphere, implying that the formally abundant H2O and CO2 remain underground, Science, 315(5811), 501-503, doi:10.1126/science.1134358.

Berner R.A. (1999), Atmospheric oxygen over Phanerozoic time, Proc. Natl. Acad. Sci. USA, 96, 1095510957.

Bertaux J.L., and Blamont J.E. (1970), OGO-5 measurements of Lymanalpha intensity distribution and linewidth up to 6 earth radii, Space Res., 10, 591601.

Bertaux J.L., et al. (2006), SPICAM on Mars Express: Observing modes and overview of UV spectrometer data and scientific results, J. Geophys. Res., 111, E10S90, doi:10.1029/2006JE002690.

Bertaux J.L., et al. (2007), A warm layer in Venus' cryosphere and high altitude measurements of HF, HCl, H2O and HDO, Nature, 450, 646649, doi:10.1038/nature05974.

Bertucci C., et al. (2013), Temporal variability of waves at the proton cyclotron frequency upstream from Mars: Implications for Mars distant hydrogen exosphere, Geophys. Res. Lett., 40(15), 3809-3813, doi:10.1002/grl.50709.

Beth A., et al. (2016), Theory for planetary exospheres: II. Radiation pressure effect on exospheric density profiles. Icarus, 266, 423-432.

Bhattacharyya D., et al. (2015), A strong seasonal dependence in the Martian hydrogen exosphere, Geophys. Res. Lett., 42, 8678-8685, doi:10.1002/2015GL065804.

Bishop J., et al. (2004), Data-model comparison search analysis of coincident PBO Balmer α, EURD Lyman β geocoronal measurements from March 2000, J. Geophys. Res., 109, doi:10.1029/2003JA010165.

Brace, L.H., and Kliore, A.J. (1991), The structure of the Venus ionosphere, Space Sci. Rev., 55, 81-163.

Brandt P.C., et al. (1999), Energetic neutral atom imaging at low altitudes from the Swedish microsatellite Astrid: Images and spectral analysis. J. Geophys. Res., 104, 2367-2379, doi:10.1029/98JA02715.

Brecht, S.H., and Ledvina, S.A. (2006), The solar wind interaction with the Martian ionosphere/atmosphere, Space Sci. Rev., 126(1-4), 15-38, doi:10.1007/s11214-006-9084-z.

Brinkmann R.T. (1970), Departures from Jeans' escape rate for H and He in the Earth's atmosphere, Planet. Space Sci., 18, 449-478, doi:10.1016/0032-0633(70)90124-8.

Cadu A., et al. (2012), Development of grazing incidence devices for space-borne time-of-flight mass spectrometry, "International Workshop on Instrumentation for Planetary Missions", Greenbelt, MD, 2012LPICo1683.1034C, 1034.

Canfield D.E. (2005), The early history of atmospheric oxygen: homage to Robert M. Garrels, Annu. Rev. Earth Planet. Sci., 33, 1-36, doi:10.1146/annurev.earth.33.092203.122711.

Cao, J., et al. (2013), Kinetic analysis of the energy transport of bursty bulk flows in the plasma sheet, J. Geophys. Res., 118, 313-320.

Carlsson E., et al. (2006), Mass composition of the escaping plasma at Mars, Icarus, 182(2), 320-328.

Chaffin M.S., et al. (2014), Unexpected variability of Martian hydrogen escape, Geophys. Res. Lett., 41(2), 314-320, doi:10.1002/2013GL058578.

Chassefiere E. and Leblanc F. (2004), Mars atmospheric escape and evolution; interaction with the solar wind, Planet. Space Sci, 52, 1039-1058, doi:10.1016/j.pss.2004.07.002.

Chaufray J.-Y., et al. (2007), Mars solar wind interaction: formation of the Martian corona and atmospheric loss to space. J. Geophys. Res. 112(E9), E09009.

Clarke J.T., et al. (2014), A rapid decrease of the hydrogen corona of Mars. Geophys. Res. Lett., 41(22), 8013-8020, doi:10.1002/2014GL061803.

Clarke J.T., et al. (2016), submitted to J. Geophys. Res.

Coates, A.J., et al. (2008), Ionospheric photoelectrons at Venus: Initial observations by ASPERA-4 ELS, Planet. Space Sci., 56(6), 802-806, doi:10.1016/j.pss.2007.12.008.

Commeyras A., et al. (2006), Peptide emergence, evolution and selection on the primitive Earth. II. The primary pump scenario, in "Lectures in Astrobiology", edited by Gargaud M., Barbier B., Martin H., and Reisse J., Vol 1, part 2, Springer, 147-170.

Craven P.D., et al. (1985), Observations of Molecular Ions in the Earth's Magnetosphere, J. Geophys. Res., 90, 75997605.

Cully C.M., et al. (2003), Akebono/Suprathermal Mass Spectrometer observations of low-energy ion outflow: Dependence on magnetic activity and solar wind conditions, J. Geophys. Res., 108, doi:10.1029/2001JA009200.

Dandouras I. (2013), Detection of a plasmaspheric wind in the Earth's magnetosphere by the Cluster spacecraft, Ann. Geophys, 31, 1143-1153, doi:10.5194/angeo-31-1143-2013.

Darrouzet et al. (2009), Plasmaspheric density structures and dynamics: properties observed by the CLUSTER and IMAGE missions, Space Sci. Rev., 145, 55106, doi:10.1007/s11214-008-9438-9.

Devoto P., et al. (2004), A low-power timing discriminator for space instrumentation, Rev. Sci. Instr., 75, 5100.

Devoto P., et al. (2008), Secondary electron emission from distributed ion scattering off surfaces for space instrumentation, Rev. Sci. Instr., 79, 046111.

Ebihara Y. and M. Ejiri M. (2000), Simulation study on fundamental properties of the storm-time ring current, J. Geophys. Res., 105, 15,84315,859, 2000.

Ebihara Y., et al. (2001), Wedge-like dispersion of sub-keV ions in the dayside magnetosphere: particle simulation and Viking observation, J. Geophys. Res., 106, 2957129584.

Ebihara Y., et al. (2004), Multiple discrete-energy ion features in the inner magnetosphere: 9 February 1998, event, Ann. Geophys., 22, 12971304, doi:10.5194/angeo-22-1297-2004.

Ebihara Y., et al. (2008), Imaging cold ions in the plasma sheet from the Equator-S satellite, Geophys. Res. Lett., 35, L15103, doi:10.1029/2008GL034357.

Ejiri M. (1978), Trajectory traces of charged particles in the magnetosphere, J. Geophys. Res., 83, 47984810.

ESA (2011), Solar Orbiter Red Book, ESA/SRE(2011)14, http://sci.esa.int/solar-orbiter/48985-solar-orbiter-definition-study-report-esa-sre-2011-14/

Fedorov A., et al. (2006), Structure of the martian wake, Icarus, 182(2), 329-336.

Fedorova A., et al. (2008), HDO and H2O vertical distributions and isotopic ratio in the Venus mesosphere by Solar Occultation at Infrared spectrometer on board Venus Express, J. Geophys. Res., 113, E00B22, doi:10.1029/2008JE003146.

Fok M.-C., et al. (2014), The Comprehensive Inner Magnetosphere-Ionosphere Model, J. Geophys. Res. Space Physics, 119, 75227540, doi:10.1002/2014JA020239.

Frahm, R.A., et al. (2006), Locations of Atmospheric Photoelectron Energy Peaks Within the Mars Environment, Space Sci. Rev., 126(1-4), 389-402, doi:10.1007/s11214-006-9119-5.

Freda J. and McDonald D.G. (1988), Physiological correlates of interspecific variation in acid tolerance in Fish, J. exp. Biol., 136, 243-258.

Fujimoto M, et al. (2006), Cross-scale coupling within rolled-up MHD-scale vortices and its effect on large scale plasma mixing across the magnetospheric boundary, Space Sci. Rev., 122(1-4), 3-18, doi: 10.1007/s11214-006-7768-z.

Füri E. and Marty B. (2015), Nitrogen isotope variations in the Solar System, Nature Geosci., 8, 515-522, doi:10.1038/ngeo2451.

Ganushkina N. Yu., et al. (2011), Locations of Boundaries of Outer and Inner Radiation Belts as

Observed by Cluster and Double Star, J. Geophys. Res., doi:10.1029/2010JA016376.
Gordiets B.F. and Kulikov Yu.N. (1985), On the mechanisms of the cooling of the nightside thermosphere of Venus, Adv. Space Res., 5, 113-117.
Gordiets B.F., et al. (1982), Numerical modelling of the thermospheric heat budget, J. Geophys. Res., 87, 4504-4514.
Gunn J.M. and Keller W. (1990), Biological recovery of an acid lake after reductions in industrial emissions of sulphur, Nature, 345, 431-433.
Guy R.D., et al. (1993), Photosynthetic fractionation of the stable isotopes of oxygen and carbon, Plant Physiol, 101, 37-47, doi:10.1104/pp.101.1.37.
Hamilton D.C., et al. (1988), Ring current development during the great geomagnetic storm of February 1986, J. Geophys. Res., 93, 14343-14355.
Harrison J., et al. (2006), Responses of terrestrial insects to hypoxia or hyperoxia, Resp. Physiol. Neurobiolog., 154(1), 4-17, doi:10.1016/j.resp.2006.02.008
Harrison J., et al. (2010), Atmospheric oxygen level and the evolution of insect body size, Proc. R. Soc. B, 277, 19371946, doi:10.1098/rspb.2010.0001
Hashimoto G.L., et al. (2007), The chemical composition of the earth terrestrial atmosphere: Formation of a reducing atmosphere from CI-like material, J. Geophys. Res., 112(E5), E05010, doi:10.1029/2006JE002844.
Hill S. (1976), Influence of atmospheric oxygen concentration on acetylene reduction and efficiency of nitrogen fixation in intact Klebsiella pneumoniae, Microbiol., 93, 335-345, doi: 10.1099/00221287-93-2-335.
Hones E.W.Jr. (1974), Prolonged tailward flow of plasma in the thinned plasma sheet observed at r~18 RE during substorms, J. Geophys. Res., 79, 1385-1392, 10.1029/JA079i010p01385.
Jakosky B. M., et al. (1994), Mars atmospheric loss and isotopic fractionation by solar-wind-induced sputtering and photochemical escape, Icarus, 111, 271-288.
Johnson C.Y. (1969), Ion and neutral composition of the ionosphere. Annals of the IQSY, 5, 197-213.
Johnson B. and Goldblatt C. (2015), The nitrogen budget of Earth, Earth Sci. Rev., 148, 150-173, doi:10.1016/j.earscirev.2015.05.006.
Kasting J.F. and Pollack J.B. (1983), Loss of water from Venus I: Hydrodynamic escape of hydrogen, Icarus, 53, 479-508.
Kasting, J.F. and Brown, L.L (1998), The early atmosphere as a source of biogenic compounds, in "The Molecular Origin of Life", edited by A. Brack, Cambridge Univ. Press, 35-56.
Kasting J.F. and Catling, D. (2003), Evolution of a habitable planet, Ann. Rev. Astron. Astrophys, 41, 429-463, doi:10.1146/nnurev.astro.41.071601.170049.
Kistler L.M., et al (2013): In-flight Calibration of the Cluster/CODIF sensor, Geosci. Instrum. Method. Data Syst. Discuss., 3, 221250, doi:10.5194/gid-3-221-2013.
Krauss S., et al. (2012), Solar flares as proxy for the young Sun: satellite observed thermosphere response to an X17.2 flare of Earth's upper atmosphere, Ann. Geophys., 30, 1129-1141, doi:10.5194/angeo-30-1129-2012.
Kronberg E.A., et al. (2014), Circulation of heavy ions and their dynamical effects in the magnetosphere: Recent observations and models, Space Sci. Rev., doi:10.1007/s11214-014-0104-0.
Ku S.-B. et al. (1977), Effects of Light, Carbon Dioxide, and Temperature on Photosynthesis, Oxygen Inhibition of Photosynthesis, and Transpiration in Solanum tuberosum, Plant Physiol, 59, 868-872, doi:10.1104/pp.59.5.868.
Kulikov Yu.N. et al. (2006), Atmospheric and water loss from early Venus, Planet. Space Sc., 54, 1425-1444, doi:10.1016/j.pss.2006.04.021.
Kulikov Yu.N. et al. (2007), A comparative study of the influence of the active young Sun on the early atmospheres of Earth, Venus, and Mars, Space Sci. Rev., doi: 10.1007/s11214-007-9192-4.
Lammer H., et al., (2003), Loss of water from Mars: Implications for the oxidation of the soil, Icarus, 165(1), 9-25.
Lammer H., et al. (2005a), Solar wind erosion of the Martian and Venusian atmospheres, in "Solar-Planetary Relations", editted by H.K. Biernat, H. Lammer, D.F. Vogl, and S. Mühlbachler, Research Signpost, Trivandrum, India, 209-217.
Lammer H., et al. (2005b), Atmospheric evolution and the history of water on Mars, in Advan. Astrobiol. and Biogeophys., Springer-Verlag Berlin, 2543.
Lammer H., et al., (2008), Atmospheric escape and evolution of terrestrial planets and satellites, Space Sci. Rev., 139, 399-436, doi:
Lammer H., et al., (2009), What makes a planet habitable?, Astron. Astrophys. Rev., 17, 181-249, doi:10.1007/s00159-009-0019-z.
Lammer H., et al. (2013), Outgassing history and escape of the Martian: atmosphere and water inventory, Space Sci. Rev. 174, 113154, doi:10.1007/s11214-012-9943-8.
Lemaire J.F. and Gringauz K.I. (1998), "The Earth's Plasmasphere", Cam bridge University Press, Cambridge.

Liemohn, M. W., et al. (2004), Dependence of plasmaspheric morphology on the electric field description during the recovery phase of the April 17, 2002 magnetic storm, J. Geophys. Res., 109(A3), A03209, doi: 10.1029/2003JA010304.

Livi S., et al. (2012), Solar wind measurements on Solar Orbiter: discovering the links between the solar wind and the atmosphere of our Sun, 39th COSPAR Scientific Assembly Held 14-22 July 2012, 39, 1101.

Loesche W.J. (1969), Oxygen sensitivity of various anaerobic bacteria, Appl. Microbiol., 18, 723-727.

Luhmann, J.G. and Bauer, S.J. (1992), Solar wind effects on atmosphere evolution at Venus and Mars, in "Venus and Mars: Atmosphere, Ionosphere, and Solar Wind Interactions", edited by Luhmann et al., American Geophysical Union, Washington D.C., 417-430.

Luhmann J.G., et al. (1992), Evolutionary impact of sputtering of the Martian atmosphere by O + pick up ions, Geophys. Res. Lett., 19, 2151-2154.

Lundin R., et al. (1990), ASPER/PHOBOS measurements of the ion outflow from the Martian ionosphere, Geophys. Res. Lett., 17, 873-876, doi:10.1029/GL017i006p00873.

Lundin R. and Barabash S. (2004), Evolution of the Martian atmosphere and hydrosphere: Solar wind erosion studied by ASPERA-3 on Mars Express, Planet. Space Sci., 52, 1059-1071, doi:10.1016/j.pss.2004.07.020.

Lundin R., et al. (2004), Solar wind-induced atmospheric erosion on Mars: First results from ASPERA-3 on Mars Express, Science, 305, 1933-1936.

Lundin R., et al. (2013), Solar cycle effects on the ion escape from Mars, Geophys. Res. Lett., 40(23), 6028-6032, doi:10.1002/2013GL058154.

Luo et al. (2014), Evidence of strong energetic ion acceleration in the near-Earth magnetotail, Geophys. Res. Lett., 41, 3724-3730, doi:10.1002/2014GL060252.

Luz B., et al. (1999), Triple-isotope composition of atmospheric oxygen as a tracer of biosphere productivity, Nature, 400, 547-550, doi:10.1038/22987.

Marcucci M.F., et al. (2004), Energetic magnetospheric oxygen in the magnetosheath and its response to IMF orientation: Cluster observations, J. Geophys. Res., 109, doi:10.1029/2003JA010312.

Marty B., et al (2011), A 15N-poor isotopic composition for the solar system as shown by Genesis solar wind samples, Science, 332, 15331536.

McComas D.J., et al. (2009), The two wide-angle imaging neutral-atom spectrometers (TWINS) NASA mission-of-opportunity, Space Sci. Rev., 142, 157-231.

Meier R.R., et al. (2015), Remote Sensing of Earth's Limb by TIMED/GUVI: Retrieval of thermospheric composition and temperature, Earth Space Sci., 2, 1-37, doi:10.1002/2014EA000035.

Mende S.B., et al. (2009), The THEMIS array of ground-based observatories for the study of auroral substorms, In "The THEMIS Mission", 357-387, Springer New York.

Mierkiewicz E.J., et al. (2012), Observed seasonal variations in exospheric effective temperatures, J. Geophys. Res., 117, doi:10.1029/2011JA017123.

Moore T.E., et al. (1999), Source processes in the high-latitude ionosphere, Ch. 2 in "Source and Loss Processes of the Magnetospheric Plasma", Space Sci. Rev., 88, 7-84, doi:10.1023/A:1005299616446.

Nilsson H., et al. (2010), Ion distributions in the vicinity of Mars: Signatures of heating and acceleration processes, doi:10.1016/j.icarus.2011.08.003.

Nilsson H. (2011), Heavy ion energization, transport, and loss in the Earth's magnetosphere, in "The Dynamic Magnetosphere", 3, 315-327, eds. W. Liu and M. Fujimoto, Springer, doi:10.1007/978-94-007-0501-2_17.

Nilsson H, et al. (2012), Hot and cold ion outflow: Spatial distribution of ion heating, J. Geophys. Res, 117, doi:10.1029/2012JA017974.

Nilsson H., et al. (2015), Evolution of the ion environment of comet 67P/Churyumov-Gerasimenko - Observations between 3.6 and 2.0 AU, Astron. Astrophys., 583, A20, doi:10.1051/0004-6361/201526142, 2015.

Nilsson H., et al. (2016), Oxygen ion response to proton bursty bulk flows, J. Geophys. Res., 121, 7535-7546, doi:10.1002/2016JA022498.

Nordström T, et al. (2013), Venus ion outflow estimates at solar minimum: Influence of reference frames and disturbed solar wind conditions, J. Geophys. Res., 118, 3592-3601, doi:10.1002/jgra.50305.

Orsini, S., et al. (2010), SERENA: A suite of four instruments (ELENA, STROFIO, PICAM and MIPA) on board BepiColombo-MPO for particle detection in the Hermean environment, 58, 166181, doi:10.1016/j.pss.2008.09.012

Østgaard N., et al. (2003), Neutral hydrogen density profiles derived from geocoronal imaging, J. Geophys. Res., 108, doi:10.1029/2002JA009749.

Owen, T.C. (1998), The origin of the atmosphere, in "The Molecular Origin of Life", edited by A. Brack, Cambridge Univ. Press, 13-34.

Pfaff R.F. Jr. (2012), The near-Earth plasma environment, Space Sci. Rev., 168, 23–112, doi: 10.1007/s11214-012-9872-6.

Paschalidis et al. (2014), A compact ion neutral mass spectrometer for the ExoCube mission, presentation at 6th European CubeSat Symposium, Estavayet, Switzerland, Oct 2014.

Paschalidis N. P et al. (2002), A CMOS time of flight system on a chip for spacecraft instrumentation, IEEE Transactions on Nuclear Science, 49, 1156-1163, June 2002.

Peterson W.K., et al. (2006), Quiet time solar illumination effects on the fluxes and characteristic energies of ionospheric outflow, J. Geophys. Res., 111, A11S05, doi:10.1029/2005JA011596

Peterson W.K., et al. (2008), Solar-minimum quiet time ion energization and outflow in dynamic boundary related coordinates, J. Geophys. Res., 113, doi:10.1029/2008JA013059.

Picone, J.M. et al. (2002), NRLMSISE00 empirical model of the atmosphere: Statistical comparisons and scientific issues, J. Geophys. Res., 107, 1468, doi:10.1029/2002JA009430.

Pierrard et al. (2008), Influence of the convection electric field models on predicted plasmapause positions during magnetic storms. J. Geophys. Res., 113, doi:10.1029/2007JA012612.

Qin J. and Waldrop L. (2016), Non-thermal Hydrogen Atoms in the Terrestrial Upper Thermosphere, submitted to Nature Communications.

Ramstad R., et al. (2013), Phobos 2/ASPERA data revisited: Planetary ion escape rate from Mars near the 1989 solar maximum, Geophys. Res. Lett., 40, 477-481, doi:10.1002/grl.50149.

Rees M.H. (1989), "Physics and Chemistry of the Upper Atmosphere", Cambridge Atmospheric and Space Science Series, 304 pp, Cambridge Univ. Press, UK.

Reeves, G. D., et al., Energy-dependent dynamics of keV to MeV electrons in the inner zone, outer zone, and slot regions, J. Geophys. Res.: Space Phys., 121, 1, doi:10.1002/2015ja021569, 2016.

Rème, H., et al. (2001), First multispacecraft ion measurements in and near the Earth's magnetosphere with the identical Cluster ion spectrometry (CIS) experiment, Ann. Geophys., 19, 1303-1354.

Ribas I., et al. (2005), Evolution of the solar activity over time and effects on planetary atmospheres I: Highenergy irradiances (1-1700 Å), Astrophys. J., 622, 680694.

Riedler, W., et al., (1997), Active Spacecraft Potential Control, Space Sci. Rev., 79, 271-302.

Robert F., et al. (2000), The Solar System d/h ratio: observations and theories, Space Sci. Rev., 92, 201-224, doi:10.1023/A:1005291127595.

Robert F. (2006), Solar System deuterium/hydrogen ratio, in "Meteorites and the early solar system II", eds: Lauretta D.S. and McSween H.Y., U. Arizona Press, 943pp., 341-351, ISBN: 978-0-8165-2562-1

Sagan C. and Chyba C. (1997), The early faint Sun paradox: Organic shielding of ultraviolet-labile greenhouse gases, cience, 276, 1217-1221.

Sagan C. and Mullen G. (1972), Earth and Mar – Evolution of atmospheres and surface temperatures, Science, 177, 52-56.

Sakanoi, T., et al. (2003), Development of the multi-spectral auroral camera onboard the INDEX satellite, Adv. Space Res., 32, No.3, 379-384, doi:10.1016/S0273-1177(03)00273-4.

Sakanoi, T., et al. (2011), Imaging observation of the earth's mesosphere, thermosphere and ionosphere by VISI of ISS-IMAP on the international space station, IEEJ Trans. on Fundamentals and Materials, vol. 131, 12, pp.983-988, doi: 10.1541/ieejfms.131.983.

Schaufelberger A., et al. (2012), Is Hydrodynamic Escape from Titan Possible?, Planet. Space Sci. 61, 79-84, doi:10.1016/j.pss.2011.03.011.

Scherer S., et al. (2006), A novel principle for an ion mirror design in time-of-flight mass spectrometry. Internat. J. Mass Spectro., 251(1), 73-81.

Schrijver C.J., et al. (2012), Estimating the frequency of extremely energetic solar events, based on solar, stellar, lunar, and terrestrial records. J. Geophys. Res. 117, A08103, doi:10.1029/2012JA017706.

Seki K., et al. (2001), On Atmospheric Loss of Oxygen Ions from Earth Through Magnetospheric Processes, Science, 291, 1939.1941, doi:10.1126/science.1058913.

Servaites J.C. (1977), pH Dependence of Photosynthesis and Photorespiration in Soybean Leaf Cells, Plant Physiol, 60, 693-696, doi:10.1104/pp.60.5.693

Shaviv N.J. (2003), Toward a solution to the early faint Sun paradox: A lower cosmic ray flux from a stronger solar wind, J. Geophys. Res., 108(A12), 1437, doi:10.1029/2003JA009997.

Sibeck D.G., et al. (1999), Plasma transfer processes at the magnetopause, Chapter 5 in Magnetospheric Plasma Sources and Losses, Space Sci. Rev., 88, 207-283.

Slapak R, et al. (2013), A statistical study on O+ flux in the dayside magnetosheath, Ann. Geophys, 31, 1005-1010, doi:10.5194/angeo-31-1005-2013.

Slapak R., et al. (2015), O+ transport in the dayside magnetosheath and its dependence on the IMF direction, Ann. Geophys., 33, 301-307, doi:10.5194/angeo-33-301-2015.

Solomon S.C., et al. (2005), New perspectives on ancient Mars, Science, 307(5713), 1214-1220, doi:10.1126/science.1101812.

Sumita, I., Hatakeyama, T., Yoshihara, A., and Hamano, Y. (2001), Paleomagnetism of late archean rocks of Hamersley basin, western Australia and the paleointensity at early proterozoic, Phys. Earth Planet. Interiors, 128, 223241.

Tian F., et al. (2005), A Hydrogen-Rich Early Earth Atmosphere, Science, 308(5724), 1014-1017, doi:10.1126/science.1106983.

Tian F., et al. (2006), Response to Comment on "A Hydrogen-Rich Early Earth Atmosphere", Science, 311(5757), 38, doi:10.1126/science.1118412.

Tian F. et al. (2008), Hydrodynamic planetary thermosphere model: 1. Response of the Earth's thermosphere to extreme solar EUV conditions and the significance of adiabatic cooling, J. Geophys. Res, 113, E05008, doi:10.1029/2007JE002946.

Tinsley B.A., et al. (1986), Monte Carlo models for the terrestrial exosphere over a solar cycle, J. Geophys. Res., 91(12), 13631-13647, doi:10.1029/JA091iA12p13631.

Tucker O.J. and Johnson, R.E. (2009), Thermally driven atmospheric escape: Monte Carlo simulations for Titan's atmosphere, Planet. Space Sci., 57, 1889-1894.

Usoskin I.G., et al. (2013), The AD775 cosmic event revisited: the Sun is to blame, Astronom. Astrophys., 552, L3, http://dx.doi.org/10.1051/0004-6361/201321080

Vidal-Madjar A. (1978), The earth hydrogen exobase near a solar minimum, Geophys. Res. Lett., 5(1), 29-32.

Walker, J.C. (1977), "Evolution of the Atmosphere", Macmillan, New York, NY.

Wang et al. (2010), Energetic ~5-90 keV neutral atom imaging of a weak substorm with STREO/STE, Geophys. Res. Lett., 37, L08107, doi:10.1029/2010GL042964.

Wood B.E., et al. (2005), Inferences about the history of the solar wind from stellar wind measurement, in "Connecting Sun and Heliosphere", ESA SP-592,

Wood B.E. (2006), The solar wind and the Sun in the past, Space Sci. Rev., 126, 3-14, doi: 10.1007/s11214-006-9006-0.

Wurz P. and Gubler L. (1994), Impedance-matching anode for fast timing signals, Rev. Sci. Instrum., 65, 871, doi:10.1063/1.1144914.

Wurz P. and Gubler L. (1996), Fast microchannel plate detector for particles, Rev. Sci. Instrum., 67(5), 1790-1793, doi:10.1063/1.1146975.

Wurz P., et al. (2012), Mass spectrometric analysis in planetary science: Investigation of the surface and the atmosphere, Solar System Res., 46, 442-459.

Yamauchi M., et al. (2005) Unusual heavy ion injection events observed by Freja, Ann. Geophys., 23, 535-543.

Yamauchi, M. and Wahlund, J.-E. (2007), Role of the Ionosphere for the Atmospheric Evolution of Planets, Astrobiology J., 7(5), 783-800.

Yamauchi M., et al. (2009a), Magnetospheric solitary structure maintained by 3000 km/s ions as a cause of westward moving auroral bulge at 19 MLT, Ann. Geophys., 27, 2947-2969, doi:10.5194/angeo-27-2947-2009, 2009.

Yamauchi, M., et al. (2009b), Dual source populations of substorm-associated ring current ions, Ann. Geophys., 27(4), 1431-1438, doi:10.5194/angeo-27-1431-2009.

Yamauchi M., et al. (2013): Cluster observation of few-hour-scale evolution of structured plasma in the inner magnetosphere, Ann. Geophys., 31, 1569-1578, doi:10.5194/angeo-31-1569-2013.

Yamauchi M., et al. (2015), Seasonal variation of Martian pick-up ions: evidence of breathing exosphere, Planet. Space Sci., 119, 54-61, doi:10.1016/j.pss.2015.09.013.

Yamazaki A., et al. (2014), Field-of-view guiding camera on the Hisaki (Sprint-A) satellite, Space Sci. Rev., 184, 259-274, doi:10.1007/s11214-014-0106-y.

Yau A.W., and Whalen B.A. (1992), Auroral ion composition during large magnetic storms. Can. J. Physics 70, 500 509,

Yau A.W., et al. (1993), EXOS D (Akebono) observations of molecular NO+ and N2+ upflowing ions in the high altitude auroral ionosphere, J. Geophys. Res. 98, 11205-11224.

Yoshikawa I., et al. (2014), Extreme ultraviolet radiation measurement for planetary atmospheres/magnetospheres from the Earth-orbiting spacecraft (Extreme Ultraviolet Spectroscope for Exospheric Dynamics: EXCEED), Space Sci. Rev., 184, 237-258, doi:10.1007/s11214-014-0077-z.

Yoshikawa I., et al. (2016), submitted to Geophys. Res. Lett.

Zoennchen J.H., et al. (2011), The TWINS exospheric neutral H-density distribution under solar minimum conditions, Ann. Geophys., 29, 2211-2217.
Zoennchen J.H., et al. (2013), Exospheric hydrogen density distributions for equinox and summer solstice observed with TWINS1/2 during solar minimum, Ann. Geophys., 31, 513527, doi:10.5194/angeo-31-513-2013.
Zoennchen J.H., et al. (2015), Terrestrial exospheric hydrogen density distributions under solar minimum and solar maximum conditions observed by the TWINS stereo mission, Ann. Geophys., 33, 413-426, doi:10.5194/angeo-33-413-2015.

Annex-B: List of ESCAPE Team members and Supporters

1. Team Members and Supporters by Institute / Country

Austria:
Maria Andriopoulou, Maxim Khodachenko, Helmut Lammer, Herbert Lichtenegger, Werner Magnes, Rumi Nakamura, Yasuhito Narita, Aris Valavanoglou (*IWF, Graz*)

Belgium:
Michel Anciaux, Sophie Berkenbosch, Fabien Darrouzet, Herbert Gunell, Johan De Keyser, Hervé Lamy, Lukas Maes, Eddy Neefs , Romain Maggiolo, Sylvain Ranvier, Ann Carine Vandaele (*Royal Belgian Institute for Space Aeronomy, Brussels*)
Jerôme Loreau (*Université Libre de Bruxelles*)

Canada:
Andrew Yau (*University of Calgary*)

China:
Feng Tian (*Tsinghua University, Beijing*)
JinBin Cao (*Beihang University, Beijing*)

Czech Republic:
Benjamin Grison, Mykhaylo Hayosh, Ondrej Santolik, Jan Soucek, Ulrich Taubenschuss (*Institute of Atmospheric Physics, The Czech Academy of Sciences*)

Finland:
Natalia Ganushkina, Kirsti Kauristie, Noora Partamies, Walter Schmidt (*Finnish Meteorological Institute, Helsinki*)
Esa Kallio (*Aalto University, Espoo*)
Thomas Ulich (*Sodankyla Geophysical Observatory*)
Anita Aikio (*University of Oulu*)

France:
Iannis Dandouras, Pierre Devoto, Philippe Garnier, Benoit Lavraud, Philippe Louarn, Christian Mazelle, Frederic Pitout, Henri Rème, Jean-André Sauvaud, Dominique Toublanc (*IRAP, Toulouse*)
Jean-Yves Chaufray, Ronan Modolo (*LATMOS, Guyancourt*)
Pierrette Décréau, Thierry Dudok De Wit, Jean-Pierre Lebreton, Jean-Louis Pinçon (*LPC2E, Orléans*)
Jean Lilensten (*IPAG, Grenoble*)
Dominique Delcourt (*LPP, Paris*)
Fabien Letisse, Jean-Charles Portais (*LISBP-INSA, Toulouse*)

Germany:
Joachim Saur (*Köln University*)
Matthias Foerster (*GFZ German Research Centre for Geosciences, Potsdam*)
Elena Kronberg (*Max-Planck-Institute for Solar System Research, Göttingen*)
Hans Fahr, Jochen Zönnchen (*Argelander Institute of Astronomy, University of Bonn*)

Greece:
Ioannis A. Daglis, Antonis Paschalis, Ingmar Sandberg (*National and Kapodistrian University of Athens*)
George Balasis (*National Observatory of Athens*)
Theodore Sarris (*Democritus University of Thrace, Xanthi*)

Hungary:
Gabor Facsko (*Research Center for Astronomy and Earth Sciences, Sopron*)

Italy:
Elisabetta De Angelis, Piero Diego, Davide Grassi, Valeria Mangano, Anna Milillo, Stefano Orsini, Christina Plainaki (*INAF/IAPS, Rome*)
Chiara Cagnazzo (*CNR/ISAC, Rome*)

Japan:
Yoshimasa Kasaba, Takeshi Sakanoi (*Tohoku University*)
Ichiro Yoshikawa, Kazuo Yoshioka (*University of Tokyo*)
Yusuke Ebihara, Akinori Saito, Satoshi Taguchi (*Kyoto University*)
Kunihiro Keika, Shin-Ichiro Oyama, Kazuo Shiokawa (*Nagoya University*)
Yasunobu Ogawa (*National Institute of Polar Research, Tachikawa*)
Shigeto Watanabe (*Hokkaido University, Sapporo*)
Shinsuke Abe (*Nihon University, Tokyo*)
Keisuke Hosokawa (*University of Electro-Communications, Tokyo*)
Satoshi Yagitani, Mitsunori Ozaki (*Kanazawa University, Kanazawa*)
Takumi Abe, Yoshufumi Saito (*JAXA*)

Norway:
Stein Haaland (*University of Bergen*)
Fred Sigernes (*UNIS Aurora Observatory*)
Cesar La Hoz (*Arctic University of Norway*)

Poland:
Hanna Rothkaehl (*Space Research Centre, Polish Academy of Sciences*)

Romania:
Mircea Ciobanu, Octav Marghitu, Adrian Blagau (*Institute for Space Sciences, Bucharest*)

Russia:
Elena Grigorenko (*Space Research Institute of Russian Academy of Science, Moscow*)

Sweden:
Herman Andersson, Stas Barabash, Urban Braendstroem, Lars Eliasson, Johan Kero, Georgios Nicolaou, Hans Nilsson, Tima Sergienko, Martin Wieser, Masatoshi Yamauchi (*IRF, Kiruna*)
Thomas Leyser, Michiko Morooka (*IRF, Uppsala*)
Carl-Fredrik Enell, Ingemar Häggström, Craig Heinselman, Ingrid Mann, Anders Tjulin (*EISCAT Scientific Association, Headquarters, Kiruna*)
Rikard Slapak (*Luleå University of Technology*)
Lars Bylander (*KTH Royal Institute of Technology, Stockholm*)
Maria Hamrin, Timo Pitkänen (*Umeå University*)

Switzerland:
André Galli, Audrey Vorburger , Peter Wurz (*University of Bern*)

UK:
Arnaud Beth (*Imperial College, London*)
Andrew Coates, Andrew Fazakerley, Jonathan Rae, Robert Wicks (*UCL/MSSL, London*)
Michael Balikhin (*University of Sheffield*)
Ian McCrea (*Science and Technology Facilities Council, Swindon*)

USA:
Toni Galvin, Lynn Kistler, Harald Kucharek, Christopher Mouikis (*University of New Hampshire, Durham*)
Raluca Ilie, Mike Liemohn (*University of Michigan*)
Vladimir Airapetian, Alex Glocer, Sarah Jones, Nikolaos Paschalidis, Ed Sittler (*NASA/GSFC*)
Pontus Brandt (*APL, Johns Hopkins University*)
George K. Parks, John Sample (*SSL, University of California, Berkeley*)

Janet Machol (*NOAA National Centers for Environmental Information*)
Maria Usanova (*LASP, Colorado*)
Lara Waldrop (*ECE Illinois*)
Edwin J. Mierkiewicz (*Embry-Riddle Aeronautical University, Daytona Beach*)
Daniel R. Weimer (*Virginia Tech*)

2. Team Members by Instrument

Instrument	Instrument Team
INMS	P. Wurz (PI) A. Galli A. Vorburger
WCIMS	N. Paschalidis (PI) S. Jones (Co-PI) V. Airapetian A. Glocer E. Sittler
MIMS	I. Dandouras (PI) P. Devoto (Technical Manager) P. Garnier B. Lavraud P. Louarn C. Mazelle F. Pitout H. Rème J.-A. Sauvaud
NOIA	M. Wieser (PI) M. Yamauchi (Co-PI) H. Andersson (Technical Manager) G. Nicolaou H. Nilsson
EMS	L. Kistler (PI) T. Galvin H. Kucharek C. Mouikis
ESMIE	A. Fazakerley (PI) A. Coates J. Rae R. Wicks
SLP	J. De Keyser (PI) S. Ranvier (Technical Manager) M. Anciaux S. Berkenbosch F. Darrouzet H. Gunell H. Lamy L. Maes E. Neefs R. Maggiolo
MAG	R. Nakamura (PI) W. Magnes (Technical Manager) Y. Narita A. Valavanoglou
WAVES	B. Grison (PI) M. Balikhin H. Rothkaehl O. Santolik
Search Coil	J.-L. Pincon (Co-PI) S. Yagitani
UVIS	I. Yoshikawa (PI) J.-Y. Chaufray K. Yoshioka
ENAI	A. Milillo (PI) E. De Angelis (Co-PI) P. Diego D. Grassi V. Mangano S. Orsini C. Plainaki
AMC	T. Sakanoi (PI) S. Abe T. Abe Y. Kasaba
DPU	A. Paschalis
Virtual Rad-Belts Instrument	I. Daglis (Co-PI) I. Sandberg

EISCAT_3D	I. Häggström (PI) C.-F. Enell C. Heinselman I. Mann Y. Ogawa F. Pitout A. Tjulin
Other Ground-Based	G. Balasis U. Braendstroem K. Hosokawa K. Kauristie C. La Hoz S.-I. Oyama N. Partamies A. Saito K. Shiokawa F. Sigernes S. Taguchi T. Ulich
Modelling and interdisciplinary analyses	F. Tian (PI : modelling)) O. Marghitu (PI : interdisciplinary) M. Liemohn (Co-PI) V. Airapetian A. Beth P. C. Brandt J.-Y. Chaufray D. Delcourt Y. Ebihara M. Foerster N. Ganushkina R. Ilie E. Kallio M. Khodachenko H. Lammer F. Letisse H. Lichtenegger J. Machol E. J. Mierkiewicz R. Modolo G. K. Parks J.-C. Portais T. Sarris J. Saur D. Toublanc L. Waldrop J. Zönnchen

Annex-C: Pictures and figures of payload and spacecraft, including test data

1. ESCAPE payload

(a) Ion and Neutral Mass Spectrometer (INMS)

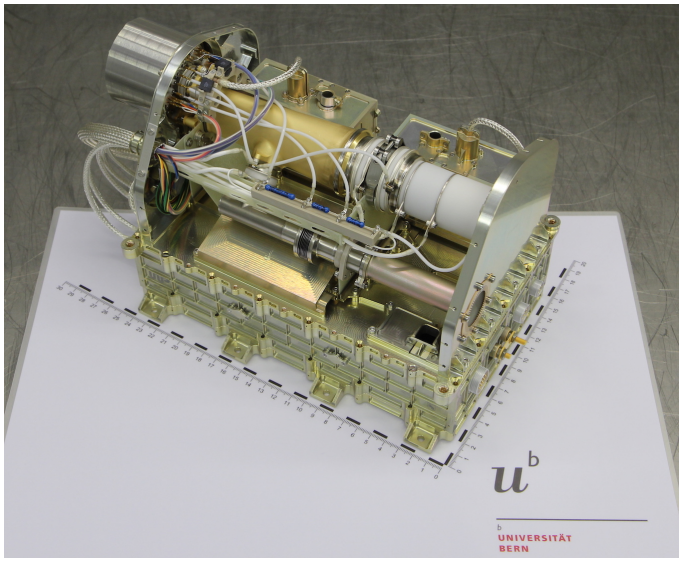

Figure C1: Picture of the flight model for Luna_Resurs. The design is the same as INMS for ESCAPE.

(b) Wide field of view Cold Ion Mass Spectrometer (WCIMS

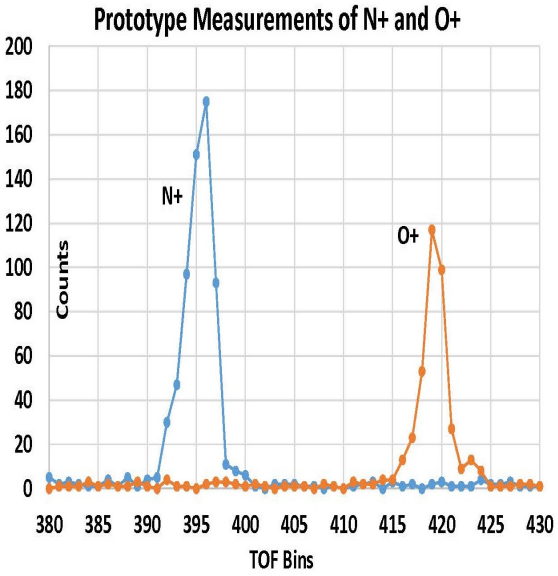

Figure C2: N^+ and O^+ measurements from the laboratory prototype with mass resolution of $M/\Delta M > 50$.

(c) MCP Ion Mass Spectrometer (MIMS)

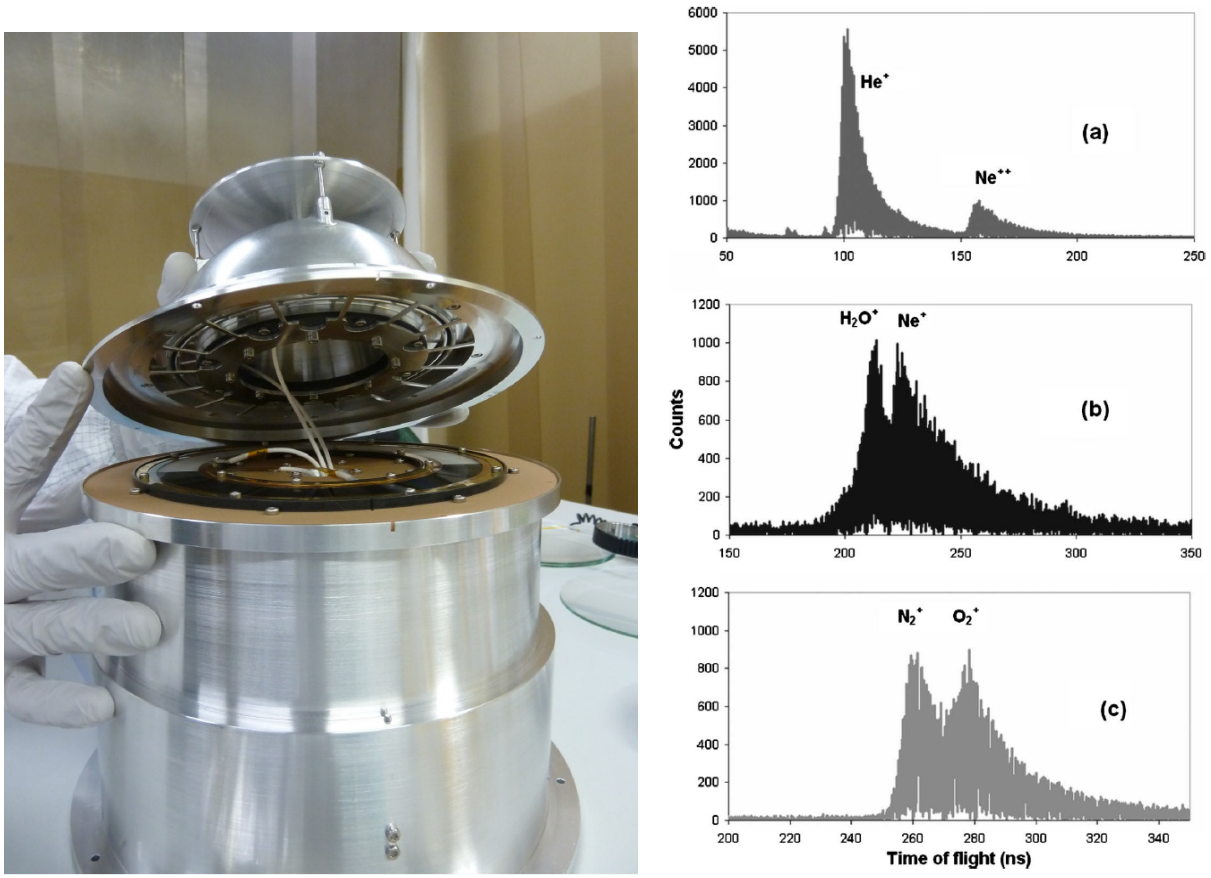

Figure C3: (left) Picture of prototype model. (right) Spectra of M/q=18 and 20, acquired in the IRAP calibration facilities with an ion beam energy of 10 keV (Devoto et al., 2008). They reveal the capacity of the instrument to clearly separate closely spaced ions, and in particular to separate nitrogen from oxygen ions.

(d) Nitrogen-Oxygen Ion Analyser (NOIA)

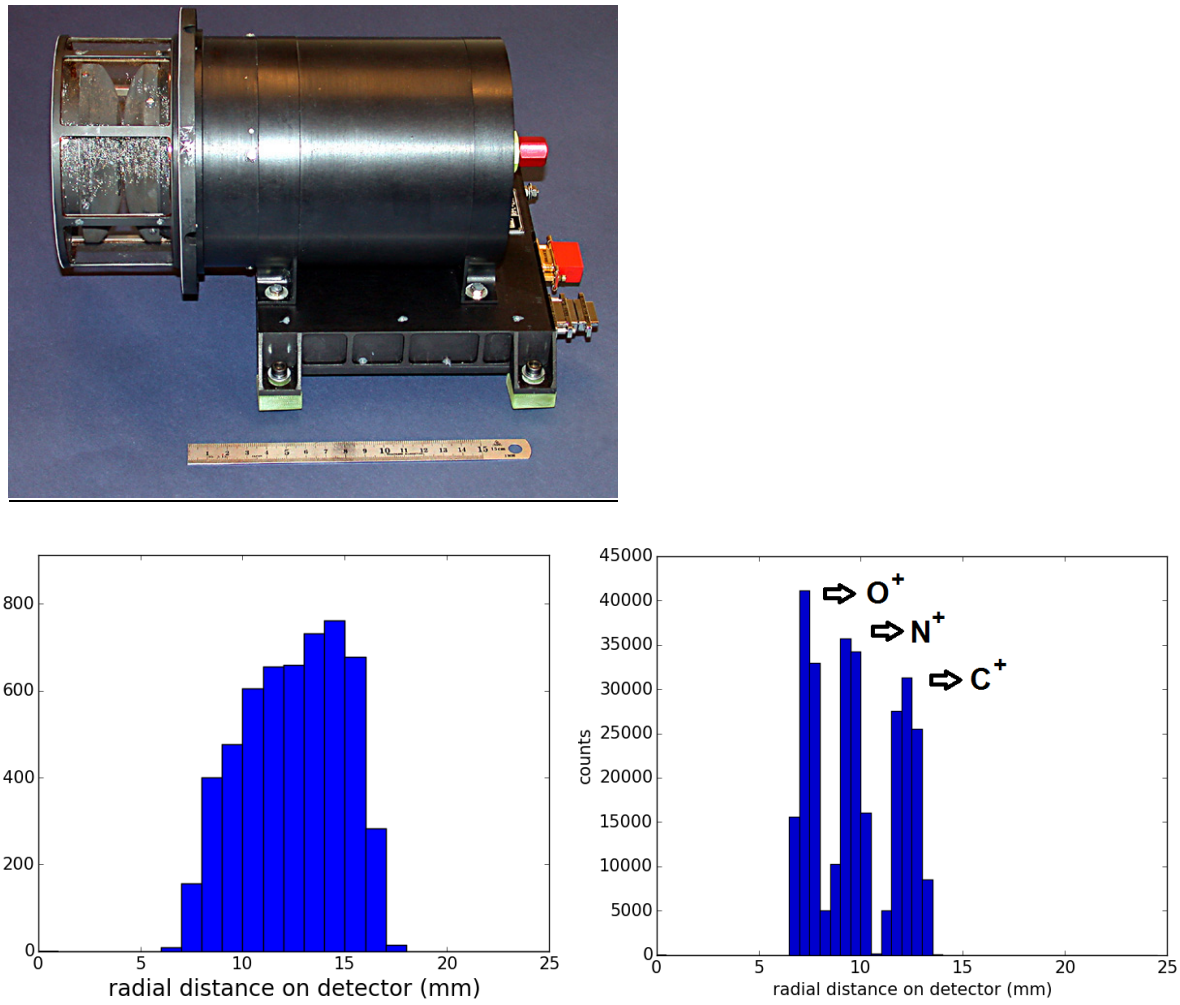

Figure C4: Flight model of ICA (top) on board Rosetta, and ion-tracing simulation trajectory results (bottom) for ICA/IMA (on board MEX, which actually separated O_2^+ and O^+) and for NOIA (with change only in geometry).

(e) Energetic Mass Spectrometer (EMS)

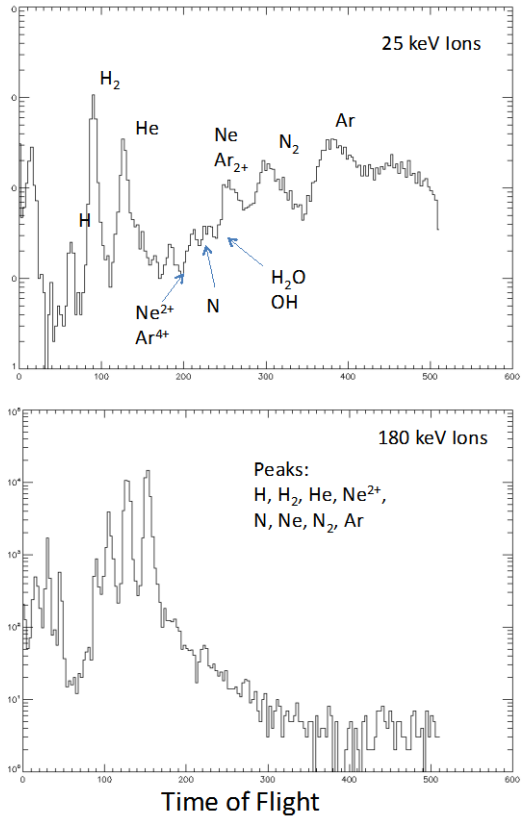

Figure C5: Example time-of-flight measurements using the HIS instrument's time-of-flight section for ions at 25 keV and 180 keV.

(f) Electron Sensor for Magnetospheric and Ionospheric Electrons (ESMIE)

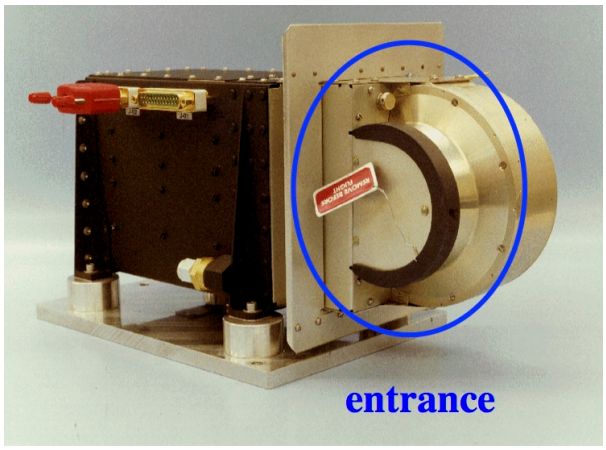

Figure C6: Cluster PEACE (the same design as ESMIE).

(g) Sweeping Langmuir Probe (SLP)

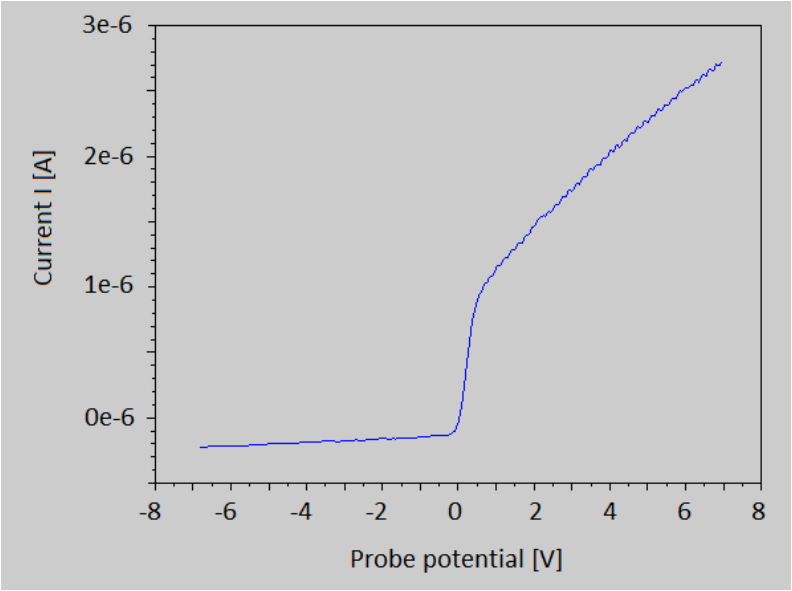

Figure C7: Current-Voltage lab measurement with the PICASSO SLP probes. Estimated N_e : 1.77e11/m³

(h) Magnetometer (MAG)

Figure C8: Magnetometer sensors and electronic box

(i) Waves signal processing (WAVES) with Search Coil Magnetometer (SCM)

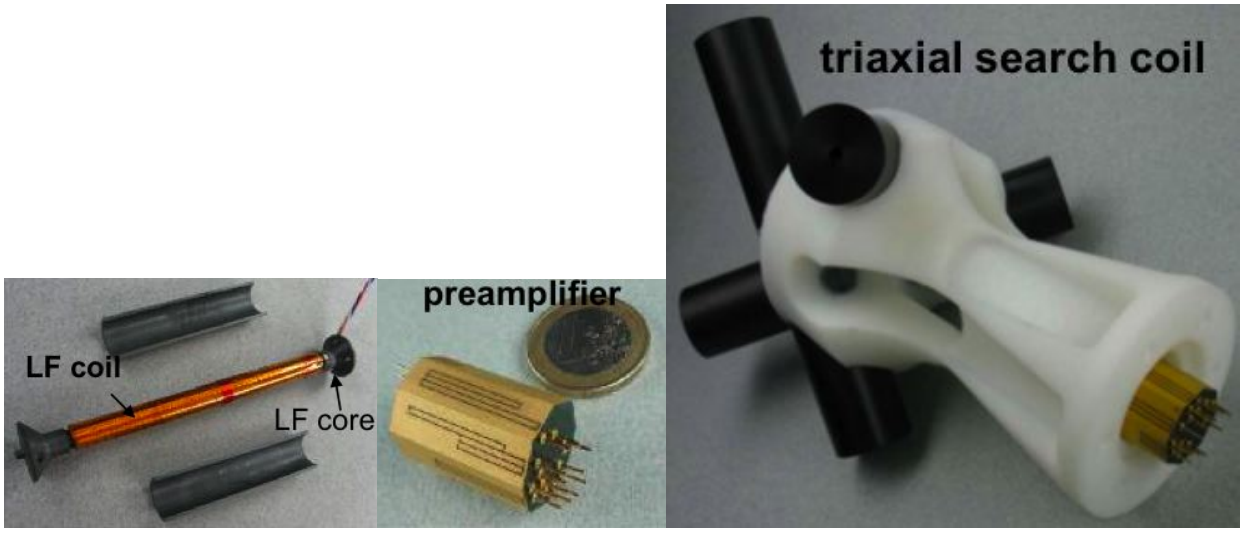

Figure C9: Sensor (left), preamplifier (middle) and sensor's foot (right) of the search coil

(j) Ultraviolet Imaging Spectrometer (UVIS)

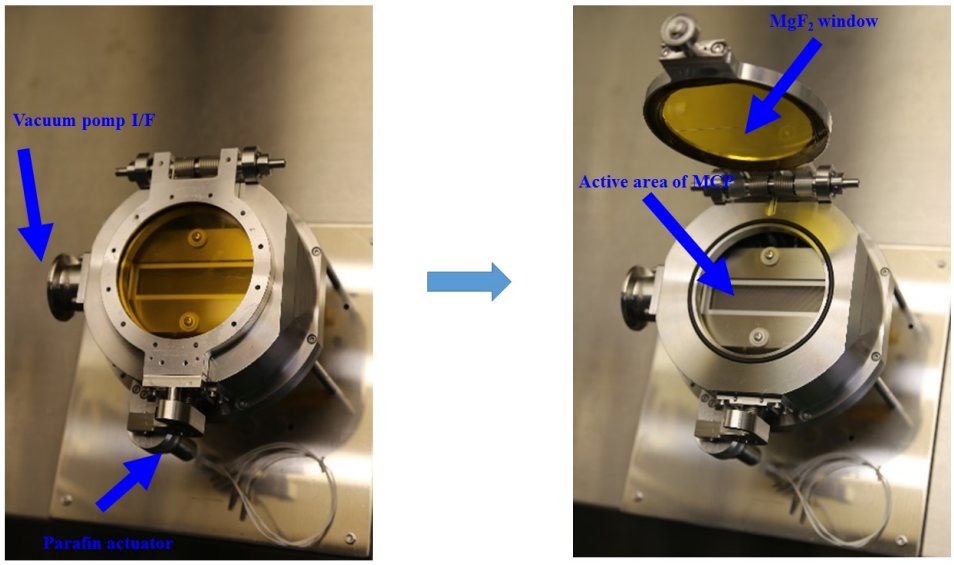

Figure C10: Photographs of the MCP assembly of the Hisaki UV imaging spectrometer. The door with the MgF2 window was opened by the paraffin actuator. Cesium Iodide (CsI) was deposited on the first face of MCP assembly as photoelectric material to increase the quantum efficiency.

(k) Energetic Neutral Atoms Imager (ENAI)

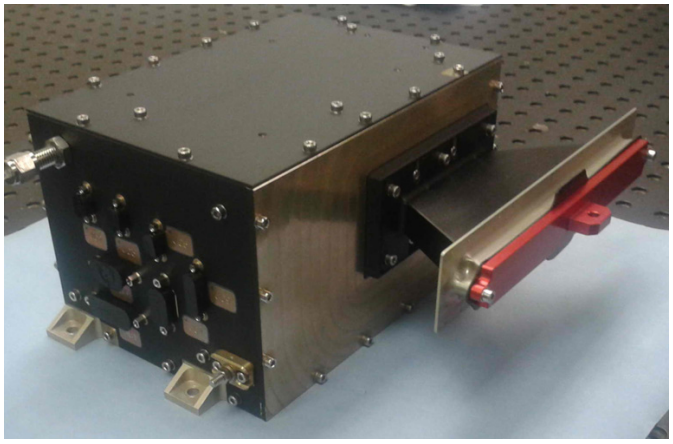

Figure C11: Bepi Colombo SERENA-ELENA instrument: ENAI heritage.

(l) Aurora Monitoring Camera (AMC)

Figure C12: ASC onboard Reimei (the same design as AMC)

(m) Active spacecraft potential control: (ASPOC)

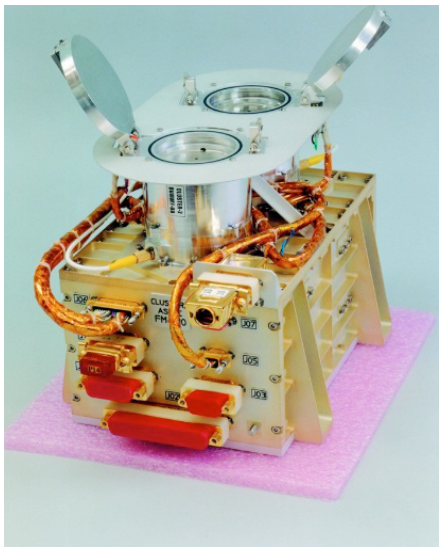

Figure C13: ASPOC

2. ESCAPE spacecraft

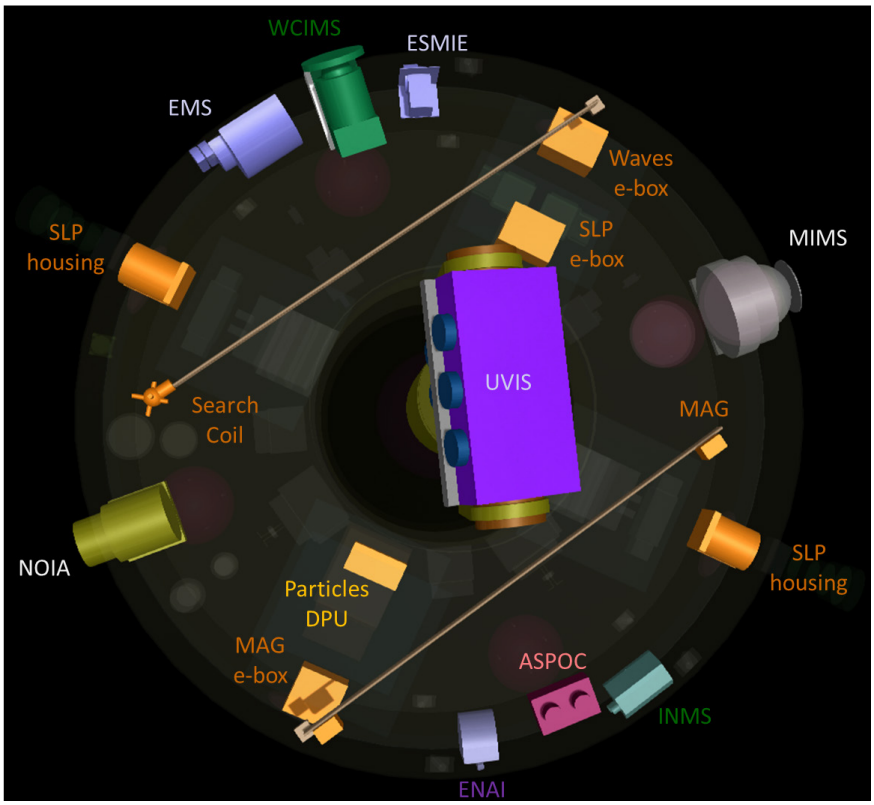

Figure C.14: Cut-view of the instrument accommodation on the ESCAPE spacecraft. Booms not deployed

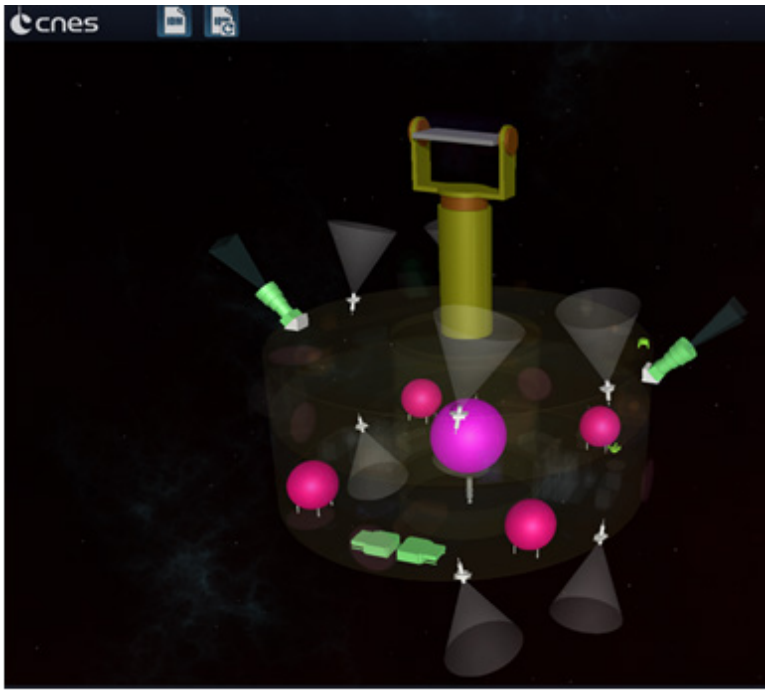

Figure C.15: ESCAPE satellite attitude and orbit control system. The thrusters (white), stellar sensors (green cones), cold gas tanks (pink) and electronics (green boxes) are represented. The magenta tank at the middle is the monopropellant tank for the end-of-mission deorbiting manoeuvre

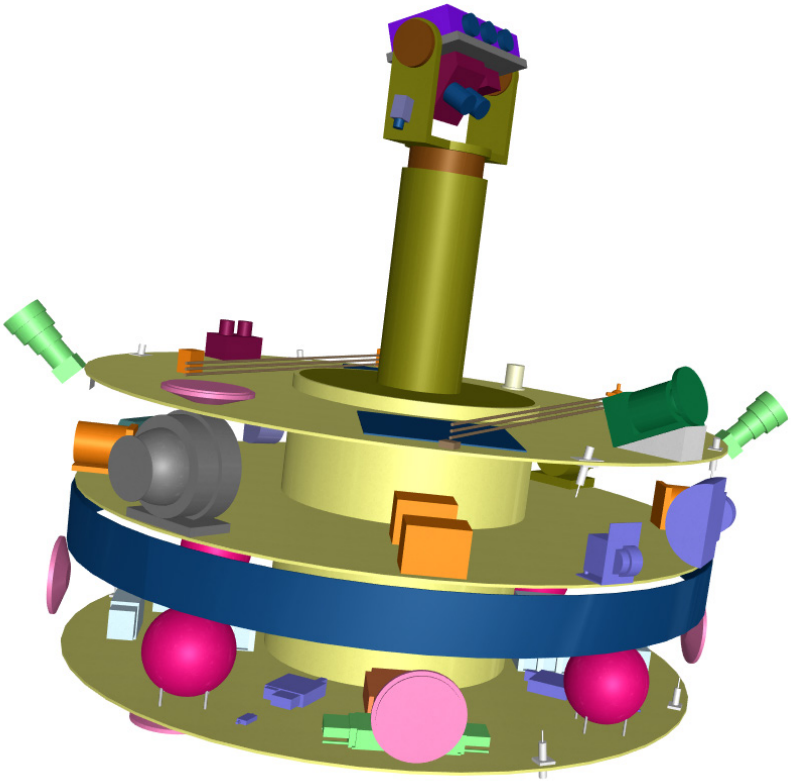

Figure C.16: ESCAPE satellite internal view.

Figure C.17: ESCAPE satellite subsystems view.

Annex-D: EISCAT_3D

The EISCAT mainland UHF and VHF systems have both been operating since the early 1980s) and will soon be replaced by a new system, EISCAT_3D. This will lead to major improvements of the capabilities compared to the present systems since EISCAT_3D will use antenna arrays instead of dish antennas, and since it will only use solid state electronics it will be fully remote-controlled and able to operate continuously. The arrays will allow transmission and reception of multiple simultaneous radio beams, measuring plasma parameters and velocities in three dimensions in a large volume of the ionosphere.

EISCAT_3D will contain a core site, with transmitters and receivers, located at Skibotn in Norway at the latitude close to that of the current mainland transmitter site. It will also contain remote, receive-only, sites in Sweden and Finland. The core site will be capable of receiving multiple simultaneous beams with a beamwidth and pointing accuracy on the order of one degree. EISCAT_3D will thus be able to observe both spatial and temporal structures in a way that the present single-antenna systems cannot. The transmitted power and the large antenna area of EISCAT_3D will also allow faster measurements than the present radars.

EISCAT_3D will be capable of continuously measuring the bulk characteristics of the plasma (including electron density and temperature and ion temperature) at fine spatial resolution (sub-100 meter) including the measurement of anisotopic temperatures. EISCAT can, to a considerable degree, also estimate the high-energy electron distribution via altitude profiles of the resulting electron densities. EISCAT_3D will be able to do this with much higher accuracy and resolve the features over narrow areas. This should be compared with in-situ data from low orbit satellites. With EISCAT_3D the results will be more directly comparable to satellite conjunction data, as the satellite footpoints will traverse a measurement volume rather than passing at some distance from the radar line of sight and the steering of the antenna beam can be accomplished on a millisecond to millisecond time frame.

EISCAT_3D is a large international infrastructure project and as such its completion will take a long time. The project started in 2005 with an EU-funded design study 2005-2009, an EU-funded preparatory phase 2010-2014, and the start of the implementation phase for the first stage in 2015, with a test sub-array already under construction in Norway. The completion of the first stage (three sites, one in Sweden, one in Norway and one in Finland) and its operation depends on the funding situation. As of Spring 2016, the European Commission (Horizon 2020, InfraDev-3) has funded 3.1 M€ for the test sub-array, Sweden has allocated 120 Msek (Swedish Research Council), Norway has allocated 228 Mnok (Research Council of Norway), Finland has allocated 12.8 M€ (Finnish Academy and the University of Oulu), Japan has included EISCAT_3D in the Roadmap 2014 and will fund it as long as the project proceeds, China's Research Institute for Radio Wave Propagation (CRIRP) is proposing EISCAT_3D for the next five-year plan and the United Kingdom has identified EISCAT_3D on the Research Councils' UK capital roadmap. If this funding is obtained, the commissioning phase should start in 2020 with full operation in 2023. Even allowing for possible delays, as is often expected for large infrastructure projects (for the EISCAT_3D case, the UK funding situation may cause small delay of 1-2 years, and technological risks such as the availability of transmitters and software development might also cause the delay of operation by 1-2 years), it would be fully operational by 2025.

Figure D1: Picture of the test array under construction.